Design and characteristics of GaAsSb Photodiodes

Yifan Liu

A thesis submitted for the degree of Doctor of Philosophy

Department of Electronic and Electrical Engineering

The University of Sheffield

Oct 2024

Contents

Acknowledgment

I am deeply grateful to Professor John P. R. David and Dr. Robert Richards for their invaluable guidance and mentorship throughout my PhD. Professor David's insightful discussions and advice have shaped my research, and Dr. Richards' dedication has continually inspired me to strive for excellence. I also thank Professor Jo Shien Ng and Professor Chee Hing Tan for their early supervision and insightful feedback on publications resulting from this work.

I am immensely thankful to Dr. Seunghyun Lee, Dr. Hyemin Jung, and their team at The Ohio State University for their efforts in MBE growth and device fabrication, and to Professor Sanjay Krishna for his guidance on paper writing.

I would like to thank my lab mates, Dr. Matthew Carr, Nada Adham, Xiaofeng Tao, and Shiyuan Gao, for their support, friendship, and enriching discussions. My appreciation extends to Dr. Harry Lewis, Dr. Xiao Jin, and Dr. Yuchen Liu, especially for their help with excess noise, avalanche multiplication measurements, and device fabrication, respectively.

A special thanks to Dr. Tarick Blain, Dr. Jonathan Petticrew, and Dr. Jonathan Tayler-Mew for their assistance in the lab, and to Dr. Jeng Shiuh Cheong and Dr. Faezah Harun for their early-stage work and theoretical contributions.

I am especially grateful to Dr. Yuting Ji, my best friend and colleague, for her unwavering support throughout my PhD and daily life. I also thank my family for their unwavering emotional and financial support.

Finally, I would like to thank Professor Gareth and Nush, my Brazilian Jiu-Jitsu instructors, for helping me maintain balance and resilience through their training and guidance.

Abstract

This thesis focuses on the design, characterization, and performance optimization of GaAsSb/AlGaAsSb Separate Absorption Charge and Multiplication (SACM) avalanche photodiodes (APDs) grown on InP substrates, targeting applications in the 1550 nm telecom wavelength range, as well as short-wave infrared (SWIR) systems for LiDAR and free-space communication.

The absorption coefficients of GaAsSb and InGaAs *p-i-n* photodiodes were measured, showing strong absorption near 1550 nm, with coefficients of approximately 8400 cm^{-1} for GaAsSb and 8100 cm^{-1} for InGaAs. Both materials demonstrated low dark current and favourable photocurrent responses, validating their suitability for photodetection in this wavelength range.

Impact ionization measurements revealed that GaAsSb has a lower electron ionization coefficient (α) than InGaAs at fields below 210 kV/cm, which results in reduced multiplication but significantly lowers noise. This makes GaAsSb ideal for low-noise applications. At higher fields, GaAsSb has smaller inter-valley separations allow competitive electron ionization rates, making it suitable for high-field applications such as long-range optical communication and LiDAR.

Electroabsorption effects in GaAsSb and InGaAs were studied, examining the Franz-Keldysh effect. A theoretical model was developed to predict the electroabsorption behaviour in both materials, providing practical insights for optimizing high-speed optical modulators and photodetectors under applied electric fields.

GaAsSb/AlGaAsSb SACM APDs demonstrated excellent performance, achieving high multiplication ($M > 1200$) and low excess noise ($F < 7$ at $M = 200$) at room temperature. Compared to commercially available InGaAs/InP devices, these APDs exhibited a 40-fold improvement in maximum achievable multiplication and 6.5 times lower excess noise at $M = 25$. Photocurrent spectral measurements were utilized to optimize the device design by providing accurate information on the electric field within the absorber region.

In conclusion, GaAsSb/AlGaAsSb SACM APDs offer a compelling alternative to InGaAs-based devices, delivering lower noise at moderate fields and strong multiplication performance at higher fields. These characteristics make GaAsSb-based APDs highly suitable for telecommunications, LiDAR, and other infrared sensing systems, where high sensitivity, low noise, and optimized field management are crucial for performance.

Publications

Journal publications

- **Liu, Yifan**, Xiao Jin, Hyemin Jung, SeungHyun Lee, Fazlul Harun, J. S. Ng, S. Krishna, and J. P. R. David. 2024. 'Electroabsorption in InGaAs and GaAsSb *p-i-n* Photodiodes'. *Applied Physics Letters* 125 (22): 221107. https://doi.org/10.1063/5.0228938.
- **Liu, Yifan**, Xiao Jin, SeungHyun Lee, Hyemin Jung, Harry Lewis, Bingtian Guo, Sri Kodati, et al. 2024. 'Very High Gain and Low Noise GaAsSb/AlGaAsSb Avalanche Photodiodes for 1550nm Detection at Room Temperature'. In *Optical Components and Materials XXI*, edited by Michel J. Digonnet and Shibin Jiang, 50. San Francisco, United States: SPIE. https://doi.org/10.1117/12.3011687.
- Jung, Hyemin, Seunghyun Lee, Xiao Jin, **Yifan Liu**, Theodore. J. Ronningen, Christopher. H. Grein, John. P. R. David, and Sanjay Krishna. 2024. 'Low Excess Noise and High Quantum Efficiency Avalanche Photodiodes for beyond 2 Mm Wavelength Detection'. *Communications Materials* 5 (1): 219. https://doi.org/10.1038/s43246-024-00627-9.
- Jung, H., S. Lee, **Y. Liu**, X. Jin, J. P. R. David, and S. Krishna. 2023. 'High Electric Field Characteristics of GaAsSb Photodiodes on InP Substrates'. Applied Physics Letters 122 (22): 221102. https://doi.org/10.1063/5.0154844.
- Lee, S., X. Jin, H. Jung, H. Lewis, **Y. Liu**, B. Guo, S. H. Kodati, et al. 2023. 'High Gain, Low Noise 1550 Nm GaAsSb/AlGaAsSb Avalanche Photodiodes'. *Optica* 10 (2): 147. https://doi.org/10.1364/OPTICA.476963.
- Jin, Xiao, Shiyu Xie, Baolai L. Liang, Xin Yi, Harry Lewis, Leh Woon Lim, **Yifan Liu**, et al. 2022. 'Comparison of the Temperature Dependence of Impact Ionization Coefficients in AlAsSb, InAlAs, and InP'. In *Optical Components and Materials XIX*, edited by Michel J. Digonnet and Shibin Jiang, 19. San Francisco, United States: SPIE. https://doi.org/10.1117/12.2609929.

- Jin, Xiao, Shiyu Xie, Baolai Liang, Xin Yi, Harry Lewis, Leh W. Lim, **Yifan Liu**, et al. 2022. 'Temperature Dependence of the Impact Ionization Coefficients in AlAsSb Lattice Matched to InP'. *IEEE Journal of Selected Topics in Quantum Electronics* 28 (2: Optical Detectors): 1–8. https://doi.org/10.1109/JSTQE.2021.3099912.

Conferences

- **Y. Liu**, X. Jin, H. Jung, S. Lee, F. Harun, J.S. Ng, S. Krishna and J. P. R. David, "The Electro-absorption Effect in InGaAs and GaAsSb p-i-n Photodiodes", 66th Electronic Materials Conference (EMC), 2024.
- **Y. Liu**, X. Jin, H. Jung, S. Lee, S. Krishna, and J. P. R. David, "Determination of Electric Field Profile in GaAsSb/Al0.85GaAsSb SACM APDs from the Electro-Absorption Effect in GaAsSb", UK Semiconductors Conference, 2024.
- **Y. Liu**, X. Jin, H. Jung, S. Lee, S. Krishna, and J. P. R. David, "Characterization of GaAsSb on InP for 1550nm Detection", Semiconductor and Integrated Optoelectronics, Cardiff, 2023

Chapter 1 Introduction

1.1 Overview

In the field of telecommunications, optical telecommunication systems stand out as transformative technologies that have dramatically enhanced how information is transmitted over distances[1]. These systems utilize light, primarily through fibre optic cables, to send signals with unparalleled efficiency and speed. Originating in the 1970s with the groundbreaking work on low-loss optical fibres by Kao and Hockham[2] and later demonstrated by Kapron et al.[3], this technology has allowed light to travel great distances with minimal signal degradation. The evolution of optical communication systems has been marked by continuous improvements in fibre manufacturing techniques, light sources, and detection methods. These advancements have collectively contributed to increasing transmission distances, data rates, and overall system reliability[4].

One of the critical aspects of optical telecommunication systems is their use of specific wavelength ranges. Typically, these systems operate within the near-infrared part of the electromagnetic spectrum, primarily between 1310 nm to 1650 nm[5]. This range is favoured because optical fibres exhibit minimal loss at these wavelengths, as shown in Fig. 1.1. The most used windows are centred around 1310 nm, and 1550 nm, each providing different balances between attenuation and performance, and chosen based on the specific requirements of the communication application.

The selection of these wavelength windows is not arbitrary but based on the fundamental properties of silica glass, the primary material used in optical fibres[6]. At 1310 nm, the fibre exhibits zero dispersion, which is beneficial for maintaining signal integrity over long distances. At the 1.31μm window, optical fibre transmission has low loss (approximately 0.6dB/km). This is further reduced to about 0.2dB/km for the 1.55μm window[7].

The development of erbium-doped fibre amplifiers (EDFAs) in the late 1980s further revolutionized optical communications by allowing direct amplification of optical signals in the 1550 nm window without the need for electronic regeneration[8]. This innovation dramatically increased the feasible transmission distances and paved the way for wavelength-division multiplexing (WDM) systems, which have greatly enhanced the capacity of optical networks.

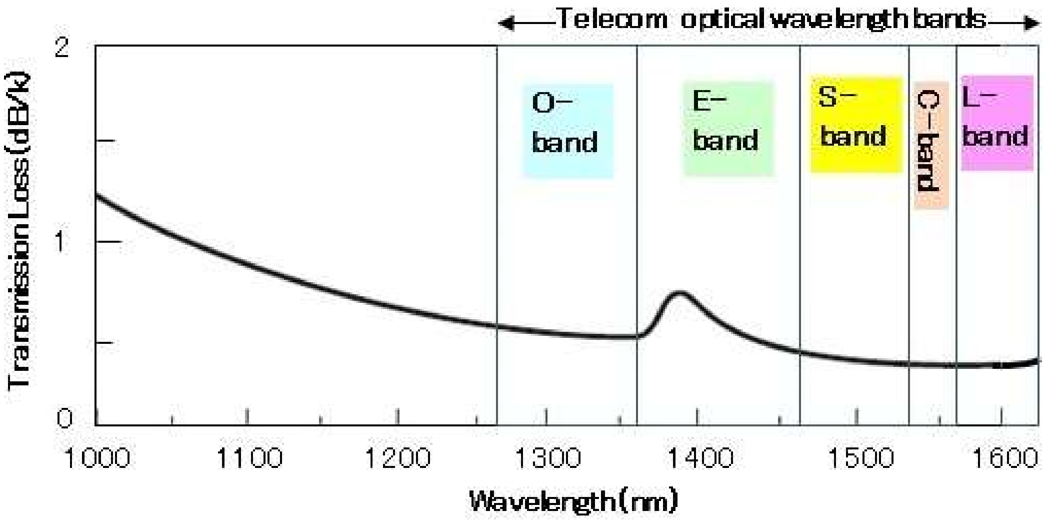

Fig. 1.1 Transmission loss in optic fibre.

In parallel with telecommunication, the choice of operating wavelengths is also crucial in LiDAR (Light Detection and Ranging) systems, which are widely used for remote sensing and ranging applications [9]. LiDAR technology has found extensive use in various fields, including autonomous vehicles, forestry, archaeology, and atmospheric studies, due to its ability to provide accurate, high-resolution 3D mapping of environments[10]. While these systems operate across various wavelengths, including 905 nm and 1064 nm, there is a growing emphasis on 1550 nm due to its unique advantages in LiDAR applications.

The 1550 nm wavelength offers a compelling combination of benefits for LiDAR systems. Perhaps most critically, it provides enhanced eye safety. At this wavelength, the cornea absorbs most of the energy before it reaches the more sensitive retina, allowing for the use of higher power levels without compromising safety. This characteristic is particularly crucial for LiDAR systems operating in public spaces, such as those used in autonomous vehicles[11]. Moreover, 1550 nm light experiences less atmospheric attenuation compared to shorter wavelengths. This property enables longer-range measurements, a significant advantage for applications like autonomous vehicles and aerial surveying where extended range is paramount[12]. The reduced atmospheric interference also contributes to improved performance in various weather conditions, enhancing the reliability of LiDAR systems.

Another advantage of the 1550 nm wavelength is its reduced susceptibility to solar interference. The solar spectrum has less intensity at this wavelength compared to shorter wavelengths, which improves the signal-to-noise ratio of LiDAR measurements in daylight conditions[13]. This feature is particularly beneficial for outdoor applications where ambient light can otherwise interfere with sensor performance. Furthermore, the 1550 nm wavelength aligns with the third telecommunication window, allowing LiDAR systems to leverage existing optical fibre technologies and components[1].

These advantages have led to increased adoption of 1550 nm LiDAR systems, which can detect objects over 200 meters distance at a typical speed of 75mph[14]. Some advanced systems are pushing this range even further, with experimental setups achieving ranges of several kilometres. However, the shift towards 1550 nm LiDAR systems presents unique challenges in photodetection. Silicon-based detectors, which are commonly used for shorter wavelengths, become ineffective at 1550 nm due to the smaller bandgap of Silicon (1.12 eV). This necessitates the use of alternative materials for efficient photodetection at this wavelength, which is where III-V semiconductor photodiodes come into play.

III-V semiconductors, composed of elements from groups III and V of the periodic table, offer several advantages for 1550 nm detection. These materials can be engineered to have a bandgap that corresponds to the energy of 1550 nm photons, enabling efficient absorption and detection[15]. Many III-V materials also exhibit strong absorption at 1550 nm, allowing for the fabrication of thin, efficient detectors[16]. The high carrier mobility often found in III-V semiconductors can lead to faster detector response times, a crucial factor in high-speed LiDAR applications[17]. Additionally, III-V materials can be grown epitaxially on various substrates, facilitating integration with other optoelectronic components.

Among III-V semiconductors, $In_{0.53}Ga_{0.47}As$ (commonly referred to as InGaAs) has emerged as a primary material for 1550 nm photodetection. InGaAs photodiodes offer high quantum efficiency, low dark current, and fast response times at this wavelength, with commercially available devices by several companies[18], [19]. However, research continues into other III-V materials and alloys, such as GaAsSb and InGaAsSb[20], for their potential to further enhance detector performance.

In the pursuit of even higher sensitivity and faster response times, Separate Absorption, Charge, and Multiplication (SACM) Avalanche Photodiodes (APDs) have gained significant attention for 1550 nm detection. SACM APDs are particularly well-suited for LiDAR applications due to their ability to provide internal gain, which can significantly improve the signal-to-noise ratio in weak signal conditions[21]. The SACM structure typically consists of a wide-bandgap absorption layer, a charge control layer, and a multiplication layer. This design allows for the optimization of each layer independently, resulting in improved performance compared to traditional APD structures. The separation of the absorption and multiplication regions helps to reduce tunnelling current and improve the excess noise characteristics of the device.

1.2 Photodetection technologies

The phenomenon of light absorption in semiconductor materials is fundamentally tied to their electronic band structure. In direct bandgap semiconductors, photons with energy equal to or exceeding the bandgap energy can excite electrons directly from the valence band to the conduction band. This direct transition mechanism facilitates efficient absorption and emission of light, making these materials particularly valuable for photodetectors and light-emitting devices[17]. III-V compound semiconductors such as InAlAs, InGaAs, and InP exemplify direct bandgap materials widely employed in high-speed and highly sensitive photodetection systems. Their bandgap energies can be engineered through composition tuning, enabling detection ranges from ultraviolet to infrared wavelengths[22]. For instance, InGaAs lattice-matched to InP is particularly suited for near-infrared detection around 1.55 μm, a crucial wavelength for optical communications[16].

While indirect bandgap semiconductors like Si and Ge can also absorb light, the process is less efficient due to the requirement of phonon assistance for momentum conservation. Despite this limitation, these materials find widespread use in photodetection, largely due to their mature production industry and integration capabilities with existing electronic technologies.

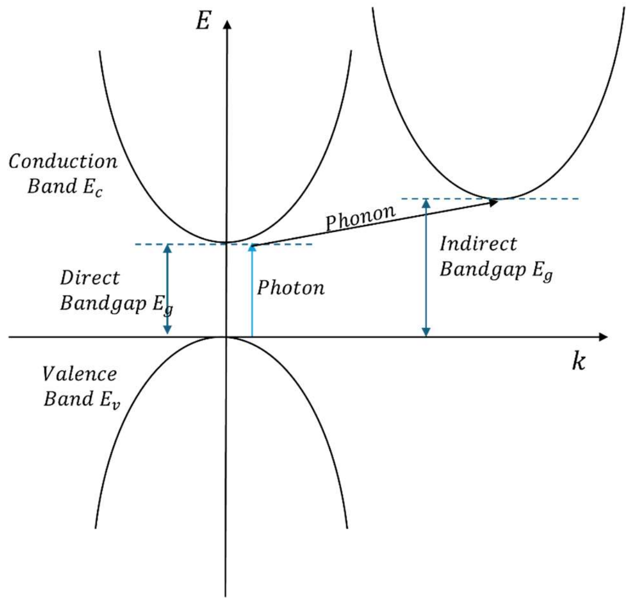

Fig. 1.2 Absorption process in direct and indirect semiconductors.

The realm of photodetectors encompasses various device architectures, each offering unique attributes suited for specific applications:

Photoconductors alter their electrical resistance in response to light. While typically slower in response time, they excel in applications requiring high sensitivity over a wide spectral range[23]. Phototransistors, essentially light-sensitive transistors, amplify photon-generated currents, offering enhanced sensitivity compared to simple photodiodes. Their utility is particularly evident in signalling and switching applications. Photomultiplier Tubes (PMTs) are renowned for their extreme sensitivity and low noise characteristics, capable of single-photon detection. This makes them invaluable in fields such as medical imaging, fluorescence microscopy, and astrophysics[24]. Photodiodes generate current when illuminated and are prized for their rapid response. Their widespread adoption spans consumer electronics, optical communication, and remote-control technologies[21].Avalanche Photodiodes (APDs) operate with internal gain via avalanche multiplication, finding use in applications demanding high sensitivity and bandwidth, such as long-range fibre optic communication[21].

The performance of these photodetectors is typically assessed based on several key metrics:

1.Responsivity: Measures the electrical output per unit light input, typically expressed in A/W. It indicates how effectively a photodetector converts light into electrical current.

2.Sensitivity: Refers to the minimum intensity of light the photodetector can effectively respond to, crucial for low-light applications.

3.Speed: Indicates how fast a photodetector can respond to changes in light intensity. Critical in applications requiring rapid detection, such as optical communication.

4.Noise: A key factor that can limit the performance of a photodetector, including thermal noise, shot noise, excess noise and dark current, affecting the device's ability to detect low levels of light.

1.2.1 Photodiodes

In the context of optical communication, not all photodetectors are equally suitable. While Photomultiplier Tubes (PMTs), pyroelectric photodetectors, and phototransistors offer unique advantages, they generally do not meet the specific needs of optical communication systems. PMTs, for example, are sensitive but too bulky and require high-voltage operation, which is impractical for compact, modern systems[24]. Pyroelectric detectors, useful in detecting temperature changes from infrared radiation, lack the speed and wavelength specificity required for transmitting optical data[25]. Phototransistors, while sensitive to light, also suffer from slower response times that can delay high-speed data processing[17].

In contrast, photodiodes (PDs) and avalanche photodiodes (APDs) have found extensive application in optical communications. Their popularity stems from a combination of compact size, high sensitivity, fast response, and cost-effectiveness. *P-i-n* photodiodes are noteworthy for their high electrical response and low noise characteristics, attributes that are crucial for maintaining signal integrity in high-speed fibre optic communication systems. The structure of a *p-i-n* photodiode typically includes a thick intrinsic layer sandwiched between $p+$ and $n+$ regions. This design is optimized for efficient conversion of light into electrical signals. When reverse-biased, the intrinsic region becomes depleted of free charge carriers, creating an environment conducive to rapid and efficient photodetection.

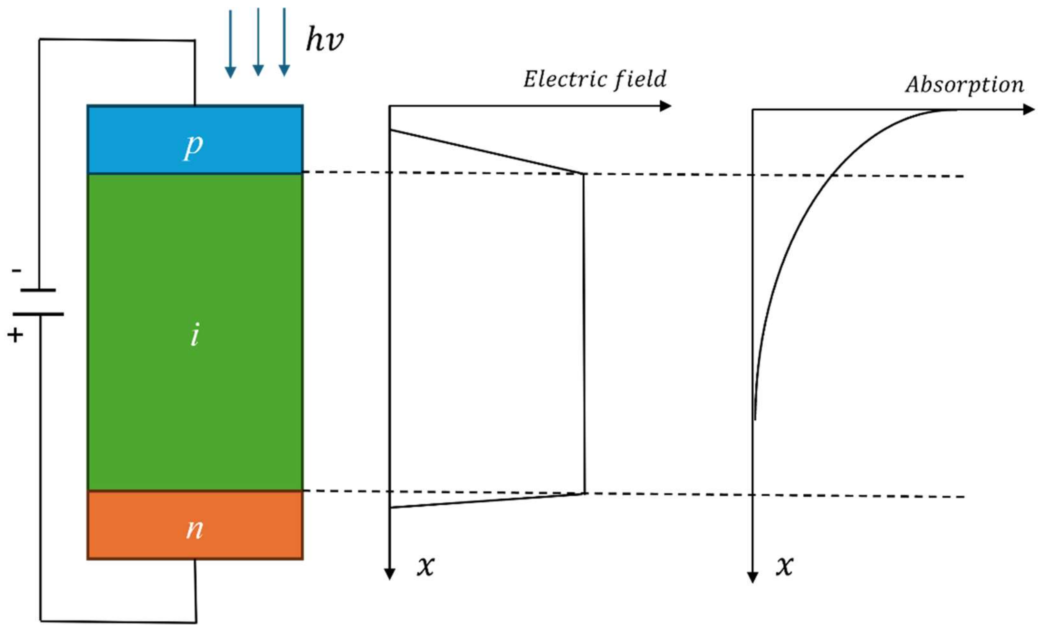

Fig. 1.3 Electric field and absorption profile in a p-i-n structure.

In the intrinsic region of a *p-i-n* photodiode, the low doping concentration results in a nearly constant electric field. This field configuration rapidly directs photogenerated electrons towards the $n+$ side and holes towards the $p+$ side. The strength of this electric field is carefully calibrated to achieve a balance between performance parameters. It must be sufficiently high to maintain saturated drift velocity for rapid response, yet below the threshold that would trigger avalanche multiplication, which could introduce excess noise and compromise signal reliability.

The quantum efficiency of a *p-i-n* photodiode is largely dependent on the thickness of its depletion region. A thicker depletion region allows for the generation of more electron-hole pairs within the electric field, thereby increasing quantum efficiency. However, this presents a design trade-off: while a thicker depletion region enhances quantum efficiency, it also increases the transit time of charge carriers, potentially limiting the speed of the device. This trade-off between quantum efficiency and speed is a critical consideration in the design of photodiodes for high-speed optical communication systems. For optimal high-speed operation, the depletion region should be as thin as possible while still maintaining sufficient quantum efficiency to meet system requirements.

1.2.2 Avalanche Photodiodes

Avalanche photodiodes (APDs) represent a significant advancement in photodetector technology, offering a unique combination of high sensitivity and internal signal amplification. These devices have found widespread application in optical communication systems, particularly at high bit rates, where their internal gain mechanism can substantially improve the signal-to-noise ratio (SNR) of optical receivers in which amplifier noise is the dominant noise source[21].

The fundamental operating principle of APDs is based on the phenomenon of impact ionization. When operated under high electric fields, carriers (electrons and holes) in APDs are accelerated as they drift across the device. These energetic carriers can generate new electron-hole pairs upon collision with the semiconductor lattice, a process known as avalanche multiplication. This mechanism provides APDs with internal gain, significantly enhancing their ability to detect weak optical signals.

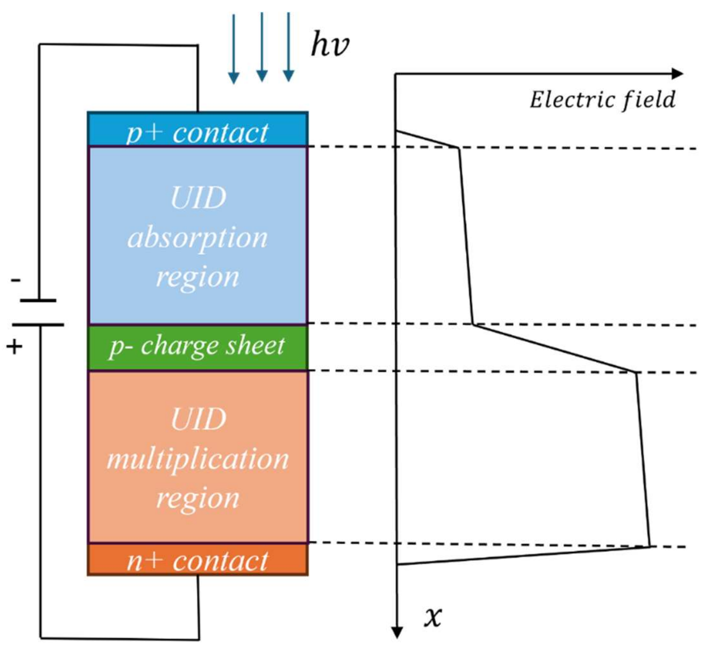

Fig. 1.4 schematics and electric field of a SACM APD.

A key design in APD technology is the Separate Absorption, Charge, and Multiplication (SACM) structure. In SACM APDs, light is absorbed in a lightly doped absorption region, similar to conventional photodiodes. The photo-generated carriers are then separated by the internal electric field and swept towards their respective contacts. A critical feature of this design is the inclusion of a charge sheet layer—a doped thin region that helps establish a high electric field in the multiplication area while maintaining a low field in the absorption area. This strategic field distribution is essential for managing the amplification process and enhancing detector efficiency. Additionally, the charge layer can be designed to grade the bandgap discontinuities between the narrow bandgap absorption layer and the wide bandgap multiplication layer, minimizing charge trapping that could otherwise degrade the APD's speed performance.

The internal gain mechanism of APDs offers several advantages. Their enhanced sensitivity allows APDs to detect very low light levels, making them ideal for long-distance communications where signals weaken over distance. The ability to operate at high speeds makes APDs suitable for high-bandwidth applications, meeting and often exceeding the requirements of advanced optical communication systems. Furthermore, in many systems, especially those limited by amplifier noise, the internal gain of APDs can significantly improve the overall signal-to-noise ratio.

These advantages have led to APDs increasingly displacing traditional optical amplification devices such as photomultiplier tubes (PMTs) in applications requiring very high sensitivity down to single-photon detection levels and high quantum efficiency (QE). Moreover, APDs are being developed into focal plane arrays for various 2-D and 3-D imaging applications where conventional detector arrays lack the required sensitivity[26]. Recent developments in semiconductor materials and structures have expanded the operational range of APDs from UV to IR wavelengths.

However, APDs are not without challenges. A significant drawback is the introduction of excess avalanche noise. This noise originates from the inherent randomness in the ionization probabilities of carriers during the avalanche process, leading to fluctuations in the multiplication value. As the gain increases, so does the avalanche noise, potentially degrading the signal quality. This makes it challenging to operate APDs at very high gains due to the resultant high noise levels[27].

To mitigate this issue, careful material selection is crucial. One strategy is to use materials where one type of carrier (either electrons or holes) predominantly contributes to the impact ionization events. This approach reduces the randomness and associated noise in the avalanche process. The ongoing research in this area focuses on developing materials and structures that can optimize the trade-off between high sensitivity and low noise.

1.3 Competing materials for telecommunication detection

The evolution of optical communication has driven the development of various photodetector materials, each with its own advantages and limitations. Initially, silicon (Si) photodiodes were prevalent due to their technological maturity, cost-effectiveness, and high quantum efficiency exceeding 80% at wavelengths around 800-900 nm[28]. These Si photodiodes were predominantly used within the first optical window of early optical communication systems. However, Si has relatively large bandgap of 1.12 eV, corresponding to an absorption cutoff wavelength of approximately 1.1μm, limits its effectiveness at longer wavelengths. Gallium Arsenide (GaAs) emerged as another cost-effective material with a detection wavelength range similar to Si and the advantage of being grown on large semi-insulating substrates. Despite these benefits, GaAs has similar absorption wavelength limit and its incompatibility with CMOS technology have led to its less extensive use in optical communication systems.

As optical communication evolved to exploit the 1300 and 1550 nm wavelengths, which offer lower dispersion loss and attenuation, focus shifted towards photodetectors capable of operating effectively at these longer wavelengths. Germanium (Ge) was one of the earliest materials used for photodiodes in the 1.0 to 1.6 μm wavelength range [29], [30]. While Ge initially aligned well with the low transmission loss and dispersion characteristics of silica optical fibres, it has limitations. Germanium has a β/α ratio of approximately 1.5 [31], resulting in higher excess noise compared to materials with a more balanced ionization coefficient. Moreover, its absorption drops significantly beyond 1.5μm, especially when cooled [32]. At room temperature, the absorption coefficient of germanium is less than 500 cm^{-1} at 1550 nm, an order of magnitude lower than that of InGaAs, reducing its effectiveness as a photodetector.

InGaAs has become a pivotal material in photodetector technology. Grown on high-quality Indium Phosphide (InP) substrates, InGaAs is a direct bandgap material that strongly absorbs light up to 1.7 μm, making it the current photodiode of choice for advanced optical communication systems. Research on InGaAs has led to commercial availability through companies like Perkin Elmer, Hamamatsu[33], and Thorlabs[34]. However, being a narrow bandgap material, InGaAs is prone to high band-to-band tunnelling currents when subjected to high electric fields, making it unsuitable for use in the multiplication region of APDs.

To address these challenges, the Separate Absorption, Charge and Multiplication (SACM) structure was developed, especially in the InP material system with InGaAs as the absorption material. InGaAs-based SACM APDs have demonstrated excellent performance with various multiplication materials lattice-matched to InP, including InP[33], InAlAs [34], and AlGaAsSb[37]. These devices exhibit high gain-bandwidth products, high speed, and low dark current. Notably, Xie et al. [37] developed an InGaAs/$Al_{0.85}Ga_{0.15}AsSb$ APD with a gain-bandwidth product of 424 GHz, the highest reported for InP-compatible APDs, combining high GBP with low dark current and minimal excess noise.

Research on GaAsSb, while not as extensive as that on InGaAs, has also provided valuable insights. Park and Jang[38] conducted initial work on GaAsSb using transmission measurements on a 1 μm MOVPE-grown GaAsSb/InP heterostructure layer, indicating promising absorption characteristics suitable for telecommunications applications.

For applications beyond traditional telecommunications, such as spectral imaging, remote sensing, and free space communications, there's growing demand for APDs operating in the 1.5 to 3μm range. This specific wavelength range is crucial due to its ability to penetrate atmospheric particles like haze or clouds, making it invaluable for several advanced applications including remote sensing, industrial inspection, surveillance and security, and scientific research.

In this domain, Mercury-Cadmium-Telluride (HgCdTe) APDs have shown exceptional performance. HgCdTe APDs with bandgap (Eg) of ~0.55eV show negligible hole-initiated ionization at room temperature, yielding a very low excess noise factor of ~1.5[39], [40]. The HgCdTe offers a tuneable bandgap by varying its Hg and Cd compositions to optimize operation at a given wavelength. However, the HgCdTe technology faces challenges in fabrication complexity and cost, which can lead to issues with uniformity across wafers and integration difficulties. Alternatively, Ge-on-Si photodiodes combine silicon's electronic properties with germanium's superior optical absorption, achieving bandwidths up to 21.5 GHz[41], making them highly promising for high-speed communications.

As optical communication technology continues to evolve, the development of new materials and structures for photodetectors remains a critical area of research, driving innovations in sensitivity, speed, and integration capabilities to meet the ever-increasing demands of modern communication systems.

1.4 Thesis description

This thesis is structured to present a comprehensive study on the design, characterization, and optimization of GaAsSb/AlGaAsSb Separate Absorption Charge and Multiplication (SACM) avalanche photodiodes (APDs) for high-performance optoelectronic applications. The chapters are organized to guide the reader through the theoretical background, experimental techniques, and results, followed by a discussion of the implications of the findings and potential areas for future research.

Chapter 1 introduces the overall research objectives and motivations. It provides an overview of the importance of SACM APDs in modern optoelectronic systems, particularly in telecommunications and infrared detection. The key challenges in developing efficient, low-noise photodetectors are outlined, and the advantages of GaAsSb/AlGaAsSb materials in these applications are discussed.

Chapter 2 presents a review of the fundamental principles underlying the operation of avalanche photodiodes, including diode theory, impact ionization, excess noise, and electroabsorption effects. It also covers competing materials like InGaAs and GaAsSb and highlights the theoretical background necessary to understand the experimental work.

Chapter 3 describes the experimental procedures and theoretical models used to characterize the GaAsSb/AlGaAsSb SACM APDs. It details the device fabrication process, measurement techniques for absorption coefficients, impact ionization coefficients, and electroabsorption effects. The methodologies for analysing device performance, including dark current, noise, and breakdown voltage, are also covered.

Chapter 4 focuses on the measurement of absorption coefficients for GaAsSb and InGaAs *p-i-n* photodiodes, with a focus on the 1550 nm telecom wavelength. Comparisons are made between the absorption characteristics of both materials, highlighting how GaAsSb offers strong absorption with lower noise, which can improve the sensitivity of SACM APDs.

Chapter 5 investigates the impact ionization properties of GaAsSb, focusing on determining the ionization coefficients for both electrons (α) and holes (β). The advantages of lower ionization coefficient at moderate fields in GaAsSb in reducing noise and enhancing APD performance are discussed.

Chapter 6 examines the electroabsorption characteristics of GaAsSb and InGaAs under varying electric fields. The effects of the elelctroabsorption effect on the absorption coefficients of these materials are analysed. A model is proposed to calculate the electroabsorption coefficients, providing a basis for optimizing the electric field in SACM structures, particularly for high-speed telecommunications applications.

Chapter 7 summarizes the key findings of this research and provides suggestions for future work.

Chapter 2 Background Theory

2.1 Diode Theory

Diodes are fundamental components in semiconductor devices, and their operation is primarily governed by the physics of charge carrier movement within a p-n junction. A diode consists of two regions of semiconductor material with opposite doping: the p-type region, which contains an abundance of holes (positive charge carriers), and the n-type region, which has an excess of electrons (negative charge carriers). When these two regions come into contact, they form a p-n junction, resulting in the diffusion of electrons and holes across the junction. This diffusion leads to the formation of a depletion region at the junction, where mobile charge carriers have recombined, leaving behind ionized donor atoms in the n-region and acceptor atoms in the p-region. These fixed charges create an electric field, known as the built-in potential, which opposes further diffusion of charge carriers.

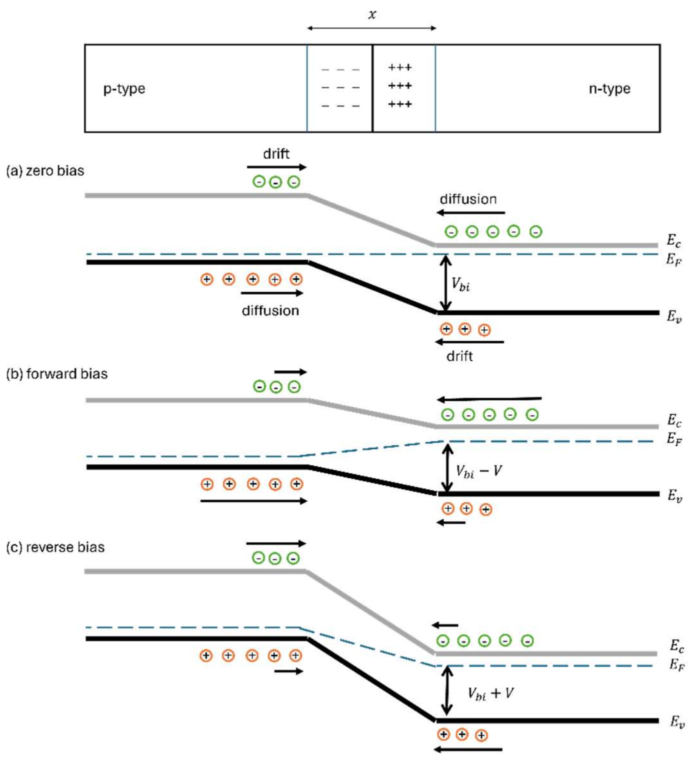

Fig. 2.1 The energy level diagram of p-n junction in (a) equilibrium, (b)forward and (c)reverse bias.

The behaviour of a diode under bias can be classified into two modes: forward bias and reverse bias. Under forward bias, an external voltage is applied in such a way that it reduces the barrier potential of the depletion region, allowing charge carriers to flow across the junction. Electrons from the n-type region are injected into the p-type region, where they recombine with holes, and similarly, holes are injected into the n-type region. This movement of charge carriers constitutes the forward current. The relationship between the applied voltage V and the resulting forward current I is described by the ideal diode equation[17]:

$$I = I_0 \left(e^{\frac{qV}{nkT}} - 1 \right) \tag{2.1}$$

where I_0 is the reverse saturation current, q is the charge of an electron, V is the applied voltage, n is the ideality factor, k is Boltzmann's constant, and T is the absolute temperature.

The ideality factor n, typically ranging from 1 to 2, reflects how closely a diode follows the ideal diode model. It provides insight into the dominant carrier transport mechanisms within the semiconductor. When $n = 1$, the current is dominated by diffusion, indicating ideal diode behaviour, whereas $n = 2$ suggests that recombination in the depletion region dominates[42]. Deviations from the ideal behaviour can also occur due to non-ideal effects such as series resistance and leakage currents, further impacting the overall diode performance[43].

In reverse bias, the external voltage increases the width of the depletion region, creating a potential barrier that prevents the majority carriers from crossing the junction. Consequently, only a small reverse saturation current I_0 flows, which is typically due to the thermal generation of minority carriers. This current remains nearly constant until the reverse bias reaches a critical point, known as the breakdown voltage. At breakdown, the electric field across the depletion region becomes strong enough to cause impact ionization, where energetic carriers create additional electron-hole pairs, leading to a sharp increase in reverse current. Two common types of breakdown mechanisms are avalanche breakdown, which occurs in lightly doped diodes with large depletion regions, and Zener breakdown, typical in heavily doped diodes with narrow depletion regions[44], [45].

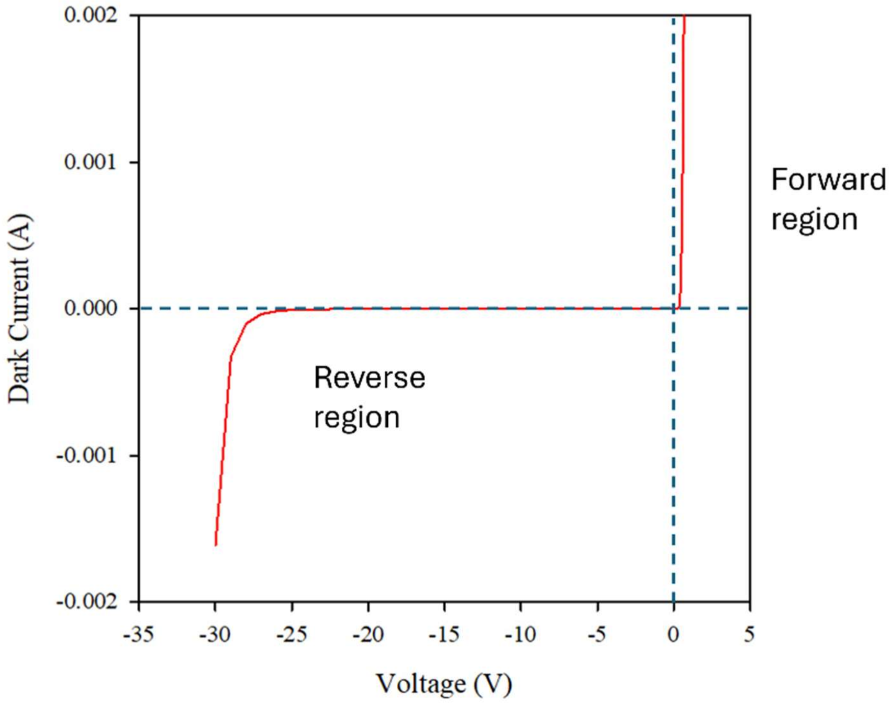

Fig. 2.2 The Current-Voltage graph of InGaAs p-i-n diodes.

However, real-world diodes often deviate from this ideal behaviour due to additional effects. For instance, series resistance R_s arises from the resistive components of the diode, such as the bulk material and contact resistance, which limit current flow at higher forward bias. Additionally, leakage currents and surface recombination further contribute to deviations from the ideal model, especially under reverse bias conditions. These non-ideal factors collectively influence the I-V characteristics, making the accurate determination of n crucial for assessing diode performance.

A *p-i-n* diode is a specialized version of the *p-n* junction diode that includes an intrinsic (undoped) region between the *p*-type and *n*-type layers. The addition of this intrinsic layer alters the behaviour of the diode in several important ways, particularly by expanding the depletion region. Under reverse bias, the intrinsic layer becomes depleted, resulting in a much wider depletion region compared to a standard *p-n* diode.

From a theoretical perspective, the wider depletion region in a p-i-n diode plays a significant role in reducing junction capacitance, which is inversely proportional to the depletion width. The reduced capacitance makes p-i-n diodes ideal for high-frequency applications, as they can operate efficiently with minimal signal distortion. The extended depletion region also enhances the electric field, allowing for better control of carrier drift and minimizing the chance of recombination before carriers reach the n or p regions.

Under forward bias, current conduction in a p-i-n diode is dominated by carrier drift rather than diffusion, as in a standard p-n diode. When forward biased, carriers are injected into the intrinsic region and drift across the depletion region under the influence of the electric field. This results in efficient current conduction, especially under high-level injection conditions where both electrons and holes are present in large quantities. The intrinsic region acts as a resistor, which reduces the on-state resistance, allowing p-i-n diodes to handle higher current loads than conventional diodes.

In reverse bias, the wider depletion region in a p-i-n diode enables higher breakdown voltages because the electric field is distributed more uniformly across the intrinsic layer. This characteristic is particularly valuable in high-voltage applications, where the ability to withstand large reverse voltages without undergoing breakdown is essential.

2.1 Absorption of light in semiconductors

The absorption of light in photodetectors is fundamentally governed by the absorption coefficient, γ, of the semiconductor material used[17], [46]. Under monochromatic wavelength illumination, the absorption of photons is directly proportional to their concentration at an infinitesimal thickness dx within the material. This relationship can be quantitatively described using an exponential decay model. The intensity of light I_T as it travels through a semiconductor, decreases exponentially according to the Lambert-Law equation[47]:

$$I_T = I_0 e^{-\gamma(\lambda)x} \tag{2.2}$$

where I_0 is the initial intensity of light at the surface of the material, and x is the distance travelled. This coefficient is a material-specific parameter that depends on factors such as the wavelength of the incident light and the electronic properties of the semiconductor. The exponential nature of this equation is shown in Fig. 2.3 shows with two different absorption coefficients, for a large absorption coefficient (10^4 cm $^{-1}$), most of the light is absorbed near the surface (with in the first few microns), conversely for a small absorption coefficient (<100 cm $^{-1}$), the light is evenly absorbed along the material.

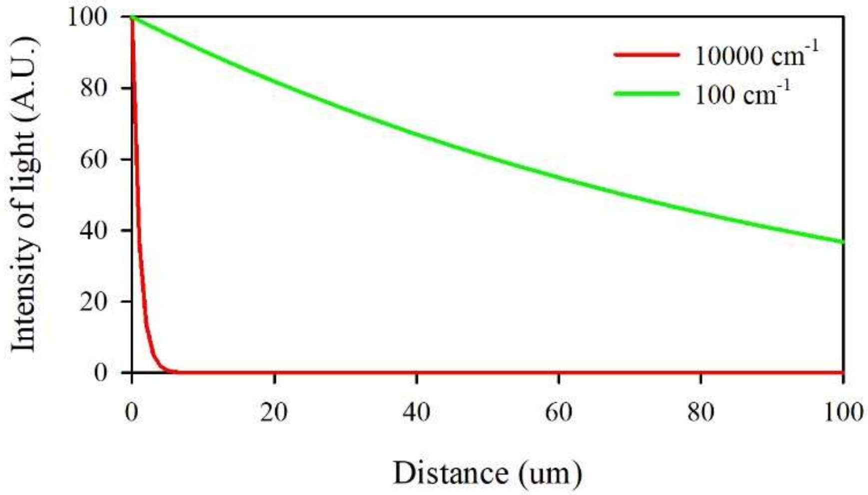

Fig. 2.3 Intensity of light as a function of distance in a semiconductor for different absorption coefficients.

Fundamental absorption in direct bandgap semiconductors occurs when a photon with energy equal to or greater than the bandgap energy (E_g) is absorbed, promoting an electron from the valence band to the conduction band. This process is characterized by a direct electronic transition that conserves crystal momentum, meaning the electron's initial and final momentum states are the same. These transitions are highly efficient due to the momentum conservation inherent in direct bandgap materials, which eliminates the need for phonon assistance, as shown in Fig 2.4. As a result, the absorption coefficient in these materials is significantly higher compared to indirect bandgap semiconductors.

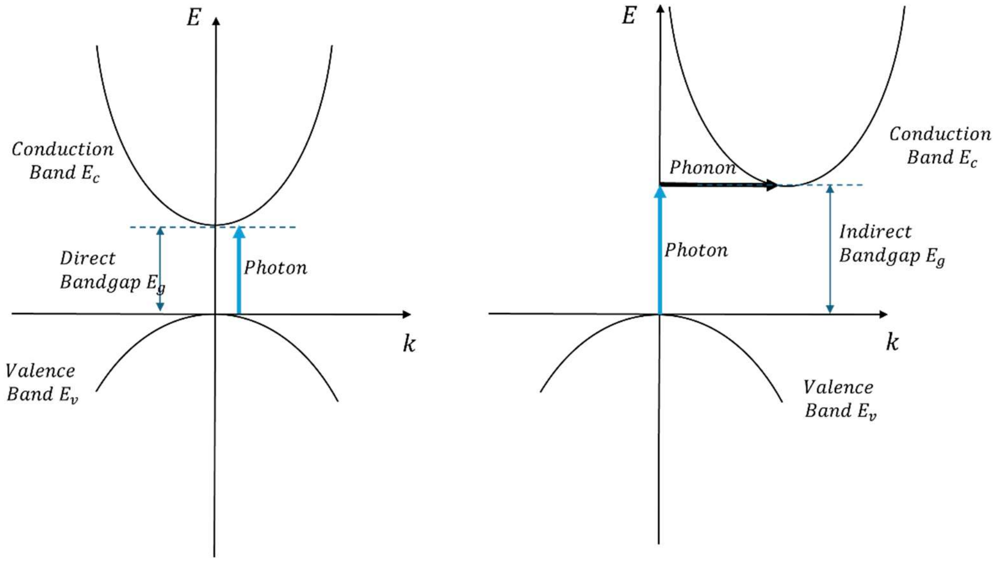

Fig. 2.4 E-k diagram of a direct (left) and indirect (right) semiconductor

Fig. 2.5 shows the absorption coefficient plotted as a function of wavelength for several well-known semiconductors at 300 K. Direct bandgap semiconductors such as GaAs and InP exhibit much sharper absorption profiles at their respective bandgap energies compared to indirect bandgap semiconductors like Ge and Si. The direct absorption at Γ valley contributes to the relatively steeper increase in the absorption coefficient of germanium for wavelengths shorter than 1.7 µm. Similarly, silicon exhibits this behaviour at wavelengths shorter than 440 nm. At even shorter wavelengths, the absorption coefficient saturates due to the limited number of available states in the conduction band. This saturation effect is observed in GaAs, Si, and Ge.

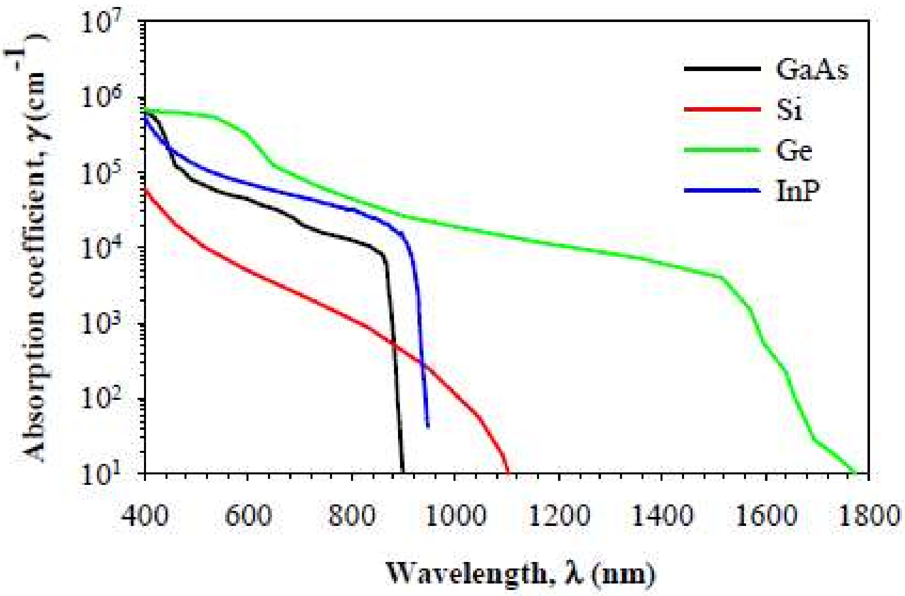

Figure 2.5 Absorption coefficients of GaAs, Si, Ge, and InP at 300 K[17], [48].

Mathematically, the absorption coefficient $\gamma(\omega)$ in a direct bandgap material can be expressed using the joint density of states and the matrix element for the optical transition[47]:

$$\gamma(\hbar\omega) = \frac{\pi e^2 \hbar}{n_r c m_0{}^2 \epsilon_0} \frac{1}{\hbar\omega} \frac{2 p_{cv}{}^2}{m_0} N_{cv}(\hbar\omega) \tag{2.3}$$

with N_{cv} being the joint density of states:

$$N_{cv}(\hbar\omega) = \frac{\sqrt{2}(m_r{}^*)^{\frac{3}{2}}(\hbar\omega - E_g)^{\frac{1}{2}}}{\pi^2 \hbar^3} \tag{2.4}$$

where e is the electron charge, $m_r{}^*$ is the reduced electron-hole mass, $\hbar$ is the reduced Planck's constant, c is the speed of light, n_r is the refractive index, E_g is the band gap, and ω is the angular frequency of the incident photon. The quantity $2p_{cv}{}^2$ is the polarization averaged matrix element, where for most semiconductors

$$\frac{2p_{cv}{}^2}{m_0} \cong 20eV \tag{2.5}$$

One can calculate the first principal absorption coefficient for a direct bandgap semiconductor for example for InGaAs, by plugging in their relative numbers in Table 2.1,

$$\gamma(\hbar\omega) = 2.38 \times 10^{4} \frac{(\hbar\omega - E_g)^{\frac{1}{2}}}{\hbar\omega} \tag{2.6}$$

Table 2.1 The parameters used for calculating absorption coefficient of InGaAs

	value	unit
$m_r{}^*$	$0.0368 \times 0.91 \times 10^{-30}$	kg
$\hbar$	1.05×10^{-34}	J*s
e	1.6×10^{-19}	C
c	3×10^{8}	m/s
n_r	3.65	No unit

This relationship from Eqn (2.6) indicates that the primary transition related absorption coefficient increases sharply as the photon energy exceeds the bandgap energy, while there is no absorption below the band gap.

In addition to these primary transitions, transitions between band tail states, which are localized states near the band edges caused by impurities or disorder, also contribute to the absorption spectrum. These states enable absorption at photon energies slightly below the bandgap. The absorption tail usually follows an exponential decay. This is known as the Urbach's rule[49]:

$$\frac{d(\ln\gamma)}{d(\hbar\omega)} = \frac{1}{kT} \tag{2.7}$$

The presence of an external electric field further modifies the fundamental absorption characteristics of semiconductors, leading to phenomena such as the electroabsorption effect, also known as the Franz-Keldysh effect. Under an electric field, the band structure of the semiconductor can be distorted, causing the conduction and valence bands to tilt. This distortion results in quantum mechanical tunnelling of electrons from the valence band to the conduction band, a process first described by Walter Franz[50] and Leonid Keldysh[51] in the late 1950s. Tharmalingam[52] and Callaway[53] introduced an effective mass approximation and used an Airy function for the numerical calculation of the oscillations and decay with photon energy of the absorption spectrum.

The equations for theoretical electro-absorption coefficient as given by [52], [53]

$$\gamma(\hbar\omega, F) = A \cdot F^{\frac{1}{3}} \left[\left| \frac{d\, Ai(\beta)}{d\, \beta} \right|^2 - \beta |Ai(\beta)|^2 \right] \tag{2.8}$$

$$\beta = B \cdot (E_g - \hbar\omega) F^{-2/3} \tag{2.9}$$

$Ai(\beta)$ is the Airy function, F is the electric field, $\hbar\omega$ is the energy of light, E_g is the bandgap energy. The approximation of factor A and B is given as [54], [55]:

$$A = \frac{C}{n\hbar\omega} \left(\frac{2\mu}{m_0} \right)^{4/3} \tag{2.10}$$

$$B = 1.1 \times 10^5 \left(\frac{2\mu}{m_0} \right)^{1/3} \tag{2.11}$$

These effects result in the shifting and broadening of the absorption edge, altering the transition probabilities and potentially increasing the material's absorption efficiency. This tunability of absorption under an electric field is crucial for the development of advanced optoelectronic devices. For instance, in photodetectors, this property can be exploited to enhance sensitivity and spectral response. In solar cells, improved absorption can lead to higher energy conversion efficiencies. Moreover, understanding the interplay between band tail states and electric field effects is essential for optimizing the performance of light-emitting diodes (LEDs) and laser diodes, where precise control over light absorption and emission is required.

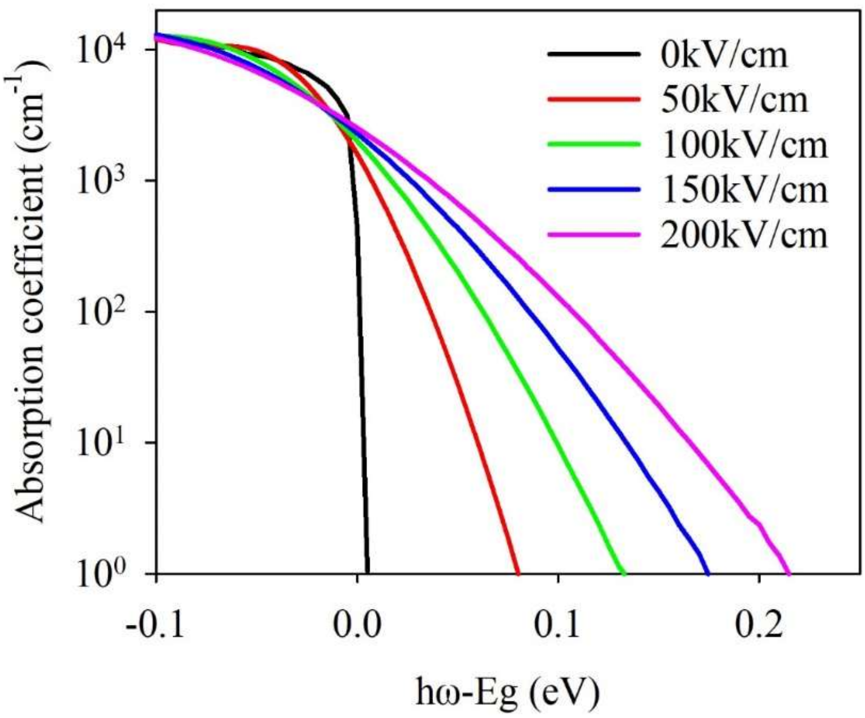

Figure 2.6 Calculated absorption coefficient in InGaAs at various electric fields using Eqn (2.7)- Eqn (2.10).

2.2 Quantum Efficiency in Photodiodes

In an ideal photodiode, the quantum efficiency (η) would be equal to one. However, reaching this level in real-world devices is difficult without internal gain[17]. Various factors, such as surface recombination, recombination of minority carriers, and reflection at the semiconductor-air boundary, can lower the quantum efficiency (η).

Surface recombination happens at the semiconductor surface due to deep-level defects caused by dangling bonds[56], disruptions in the crystal structure[57], and multiple phonon interactions[58]. These defects increase the probability of non-radiative recombination at the surface, rather than allowing carriers to diffuse into the depletion region. This issue is especially prominent at shorter wavelengths, where the absorption depth (γ^{-1}) is only a few tens of nanometres, making it less likely for carriers to contribute to the photocurrent. Consequently, photodiodes often exhibit a short wavelength cut-off, where their responsivity drops to nearly zero as the wavelength decreases. To counteract surface recombination, techniques like surface passivation can be employed to reduce surface states[59], or a "barrier" can be created at the semiconductor-air interface, such as with a heterojunction[60] or a heavily doped surface layer[61].

Additionally, minority carriers created at distances beyond the diffusion length from the depletion region are more likely to recombine before generating a photocurrent. The diffusion length is influenced by several factors, including crystal quality[62], doping concentration, temperature[63], and whether the material has a direct or indirect bandgap[64]. Light reflection at the semiconductor-air interface can also reduce quantum efficiency, but this can be minimized by using anti-reflection coatings. For optimal performance, photons should ideally be absorbed within the depletion region, where the electric field can quickly sweep the carriers away, minimizing the chances of recombination.

These considerations can be analytically modelled in the quantum efficiency equation, derived from the current-continuity equation. The model assumes that electron-hole pairs generated within the depletion region are collected with 100% efficiency due to the electric field. Therefore, the quantum efficiency η in the intrinsic region primarily depends on the absorption coefficient. For a *p-i-n* diode with monochromatic light entering from the *p*-cladding, the generation rate of electron-hole pairs at a given position can be expressed as:

$$G(x) = \begin{cases} 0 & x < 0 \\ G_0 \exp(-\gamma x) & x \geq 0 \end{cases} \tag{2.12}$$

where G_0 is the number of photons injected per unit area from the *p*-cladding. The photocurrent J_{dr} can be calculated by integrating this equation with the appropriate limits (x_1 and x_2):

$$J_{dr} = -q \int_{x_1}^{x_2} G_0 \gamma \exp(-\gamma x) = qGe^{-\gamma x_1}\left[1 - e^{-\gamma(x_2 - x_1)}\right] \tag{2.13}$$

The quantum efficiency η_i can then be expressed as:

$$\eta_i = \frac{J_{dr}}{qG_0} = e^{-\gamma x_1}\left[1 - e^{-\gamma(x_2 - x_1)}\right] \tag{2.14}$$

Carriers generated in the *p* and *n*-cladding regions outside the depletion region can also contribute to the photocurrent through diffusion. The photocurrent density due to electrons can be obtained using the one-dimensional diffusion equation, accounting for surface recombination:

$$J_n = \left[\frac{qG_0\gamma L_e}{\gamma^2 {L_e}^2-1}\right]\left[\frac{\frac{S_eL_e}{D_e}+\gamma L_e-\exp(-\gamma x_1)\left(\frac{S_eL_e}{D_e}\cosh\frac{x_1}{L_e}+\sinh\frac{x_1}{L_e}\right)}{\frac{S_eL_e}{D_e}\sin\frac{x_1}{L_e}+\cosh\frac{x_1}{L_e}} - \gamma L_e \exp(-\gamma x_1)\right] \tag{2.15}$$

where L_e is the electron diffusion length, S_e is the surface recombination velocity at the p-cladding, and D_e is the electron diffusion coefficient which is related to $L_e = \sqrt{D_e \tau_e}$ where τ_e is the minority electron lifetime.

The quantum efficiency η_n due to electrons in the *n*-cladding is then:

$$\eta_n = \frac{J_n}{qG_0} = \left[\frac{\gamma L_e}{\gamma^2 {L_e}^2-1}\right]\left[\frac{\frac{S_eL_e}{D_e}+\gamma L_e-\exp(-\gamma x_1)\left(\frac{S_eL_e}{D_e}\cosh\frac{x_1}{L_e}+\sinh\frac{x_1}{L_e}\right)}{\frac{S_eL_e}{D_e}\sin\frac{x_1}{L_e}+\cosh\frac{x_1}{L_e}} - \gamma L_e \exp(-\gamma x_1)\right] \tag{2.16}$$

Similarly, for holes generated in the *p*-cladding, the photocurrent density J_p is:

$$J_p = \left[\frac{qG_0\gamma L_h}{\gamma^2 {L_h}^2-1}\right]\exp[-\gamma(x_3 - x_2)]\left[\gamma L_h - \frac{\frac{S_hL_h}{D_h}\left[\cosh\frac{x_3}{L_h}-\exp(-\gamma x_3)\right]+\sinh\frac{x_3}{L_h}+\gamma L_h\exp(-\gamma x_3)}{\frac{S_hL_h}{D_h}\sinh\frac{x_3}{L_h}+\cosh\frac{x_3}{L_h}}\right] \tag{2.17}$$

with η_p given by:

$$\eta_p = \frac{J_p}{qG_0} = \left[\frac{\gamma L_h}{\gamma^2 {L_h}^2-1}\right]\exp[-\gamma(x_3 - x_2)]\left[\gamma L_h - \frac{\frac{S_hL_h}{D_h}\left[\cosh\frac{x_3}{L_h}-\exp(-\gamma x_3)\right]+\sinh\frac{x_3}{L_h}+\gamma L_h\exp(-\gamma x_3)}{\frac{S_hL_h}{D_h}\sin\ \frac{x_3}{L_h}+\cosh\frac{x_3}{L_h}}\right] \tag{2.18}$$

where L_h is the hole diffusion length, S_h is the surface recombination velocity at the *n*-cladding, and D_h is the hole diffusion coefficient.

The internal quantum efficiency η_{int} of a *p-i-n* diode is the sum of the efficiencies due to the intrinsic region, electrons, and holes. The external quantum efficiency η_{ext} also takes into account the reflectivity R of the semiconductor surface:

$$\eta_{ext} = (1-R)\times\eta_{int} = (1-R)\times(\eta_i + \eta_n + \eta_p) \tag{2.19}$$

2.3 Optical constant characterization methods

The performance of optoelectronic devices such as lasers, solar cells, and waveguides is highly dependent on the optical constants of the materials used, including refractive indices, dielectric constants, extinction coefficients, and absorption coefficients. These parameters change with wavelength, temperature, and electric field, making it crucial to accurately determine them for device optimization. Transmission and ellipsometry measurements are two reliable methods to extract these properties. This section outlines the principles, advantages, and disadvantages of these methods, with a brief mention of other techniques and an introduction to the phase-sensitive photocurrent method for detailed discussion later.

2.3.1 Transmission Measurements

Transmission measurements involve passing light through a sample and recording the intensity of the transmitted light to calculate the absorption coefficient (γ) using the Lambert-Law equation in Eqn. (2.2). This straightforward method works well for materials with low absorption but requires a transparent substrate and can be less accurate for highly absorbing or translucent materials due to scattering and diffusion.

Early studies on Ge and Si absorption measured the transmission by illuminating samples with monochromatic light and detecting the transmitted intensity[65], [66]. Repeating measurements for various thicknesses ensured consistent γ values. However, multiple reflections and Fabry-Perot oscillations due to interference complicate the results. To account for this, the absorption coefficient γ is calculated as[67]:

$$\frac{I_T}{I_0} = \frac{(1-R)^2 + 4Rsin^2(y)e^{-\gamma x}}{1-R^2e^{-2\gamma x}} \tag{2.20}$$

where

$$y = \tan^2\left[\frac{2K}{(n^2+K^2-1)}\right] \tag{2.21}$$

R is the reflectivity, n and K are the refractive index and extinction coefficient of the material respectively. To determine R accurately, the sample is illuminated with light of wavelengths longer than the material cut-off wavelength, ensuring $\gamma \to 0$. Then Eqn. (2.20) simplifies to

$$\frac{I_T}{I_0} = \frac{(1-R)}{(1+R)} \tag{2.22}$$

This approach ensures that the absorption characteristics of the material are accurately reflected by minimizing errors due to surface roughness and oxide layers. However, highly absorbing materials ($\gamma > 10^3 cm^{-1}$) challenge transmission measurements, as I_T approaches zero, potentially falling below the detector's sensitivity, as a results. thin film samples of a few microns thickness are usually required for reliable results.

2.3.2 Spectroscopic Ellipsometry (SE)

Ellipsometry, initially proposed by Drude[68] and later demonstrated by Ingersoll and Littleton[69], provides another method for determining γ. It measures changes in light polarization from linear to elliptical upon reflection, using the relationship:

$$\gamma = \frac{4\pi}{\lambda} \tag{2.23}$$

Electromagnetic waves consist of electric and magnetic fields. The electric field component, polarized light, decomposes into s and p vectors, perpendicular and parallel to the plane of incident light. Linearly polarized light results when s and p vectors are in phase. Upon reflection, the different phase changes of p and s components alter the polarization to elliptical. The ellipsometer measures the amplitude and phase difference and relates these to the material's complex refractive index ($n^* = n + iK$) via Fresnel's equations.

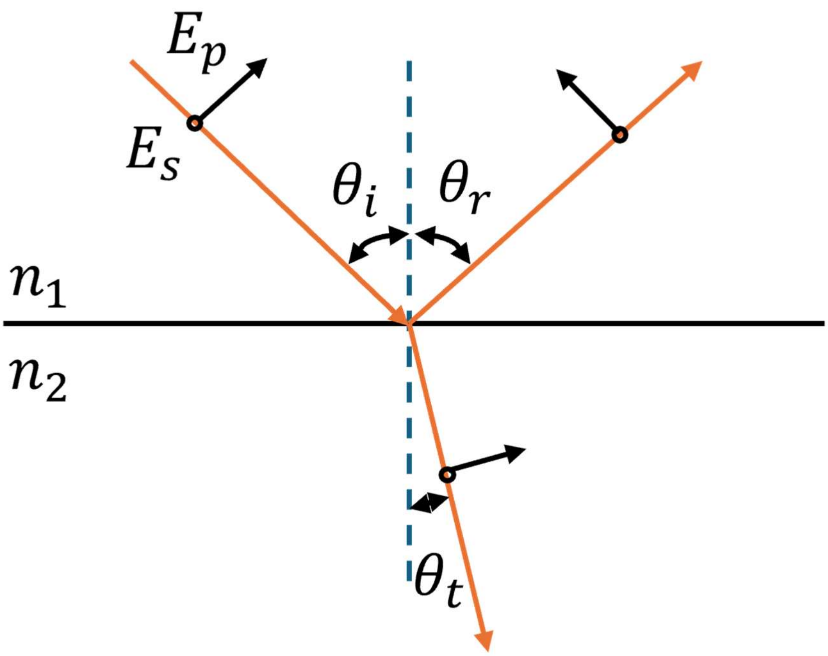

Fig. 2.7 A light travels from medium 1 to 2 with an incident angle of θ_i which its electric field component of two perpendicular s and p vector.

Ellipsometry is more accurate than transmission measurements as it involves relative measurements of reflectance ratios rather than absolute intensities. Ellipsometry can achieve sub-nanometre accuracy for film thickness, provided the sample is homogeneous and free of surface contaminants[70]. However, it requires significant time for spectral measurements and can be less reliable for $\gamma < 10^4 cm^{-1}$ due to surface roughness and oxide layers affecting precision. Moreover, the measurement's precision depends on accurately determining Δ, the phase difference, which impacts K, the imaginary part of n^*. A small deviation in Δ can significantly affect γ, making transmission measurements preferable for low absorption values.

2.3.3 Brief Mention of Other Methods

1. Swanepoel's Envelope Method:

This method utilizes the transmission spectrum displaying interference fringes to determine the absorption coefficient and film thickness[71]. It is accurate for samples with uniform thickness but becomes less effective for materials with high absorption where interference fringes are not visible. Improvements such as the Tangent Point Method (TPM) have enhanced its accuracy for materials with abnormal thickness values in strong absorption regions.

2. Transfer Matrix Method (TMM):

TMM analyses the absorption coefficient for propagation through layered materials, taking into account coherent wave superposition[72]. It is suitable for complex structures but requires detailed knowledge of each layer's properties and can be computationally intensive. This method is particularly useful for multilayer structures where interference effects are significant.

3. Interpolation Method:

This method estimates the absorption coefficient of new ternary and quaternary compounds using known data from binary compounds[73]. It provides quick theoretical estimations but heavily depends on the precision of the baseline binary material data. Recent advancements have improved its reliability by incorporating algorithms that map critical points based on material composition.

4. Phase-Sensitive Photocurrent Method

The phase-sensitive photocurrent method, involving a monochromator and lock-in amplifier, calculates the absorption coefficient from the measured photocurrent, responsivity, and external quantum efficiency (EQE). This technique uses a monochromator to select specific wavelengths of light and a lock-in amplifier to enhance the signal-to-noise ratio by synchronizing the detection with a reference signal. This method is precise for materials where all generated carriers contribute to the photocurrent, making it particularly useful for semiconductor devices. The detailed exploration of this method will be provided in Chapter 3.

2.4 Overview of impact ionization

Avalanche multiplication in an Avalanche Photodiode (APD) is primarily governed by the ionization coefficients for electrons (α) and holes (β), which define the number of electron-hole pairs generated by a single initiating carrier per unit distance in an electric field[16], [74]. These coefficients are crucial in determining the multiplication gain, $M(x)$, and the overall performance of the APD. The inverse of these coefficients represents the mean distance between successive impact ionization events, making α and β dependent on both the electric field strength and the material's band structure[17], [75].

In an APD, the multiplication process occurs as an electron moves through the depletion region, gaining energy from the electric field. As shown in Fig 2.8, once the electron reaches a critical energy threshold, it can generate a new electron-hole pair by promoting an electron from the valence band to the conduction band, leaving a hole behind. Both the primary electron and the newly created electron can undergo further ionization events, resulting in a cascading multiplication effect. This process continues as long as carriers gain sufficient energy to initiate additional ionizations. Similarly, holes moving in the opposite direction under the electric field can contribute to the multiplication process, depending on the ionization rate for holes.

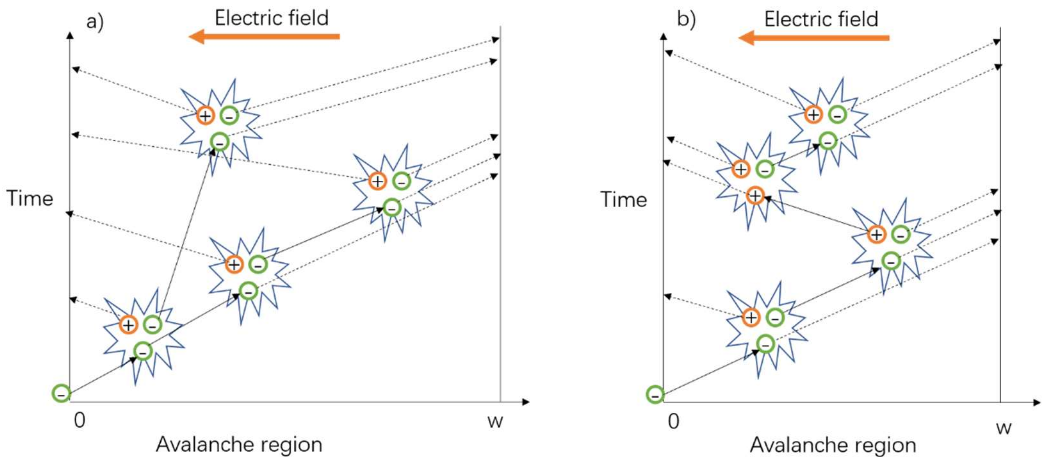

Fig. 2.8 schematic diagram of electron-initiated avalanche multiplication process where a) β=0, b) α=β.

The gain $M(x)$ in the APD is closely linked to the ionization coefficients α and β, and it depends on where the primary electron-hole pair is generated within the multiplication region. For a diode with a multiplication region of length w, if an electron travels to the right and a hole travel to the left, the electron will, on average, generate αdx ionizing collisions over a distance dx, while the hole will produce βdx electron-hole pairs over the same distance. These newly generated carriers are then swept by the electric field and can trigger further ionization events, leading to a cascading amplification of the current.

The average gain $M(x)$ resulting from an electron-hole pair injected at position x in the multiplication region can be expressed as:

$$M(x) = \frac{exp\left[-\int_0^x \left(\alpha(x') - \beta(x')\right) dx'\right]}{1 - \int_0^w \alpha(x') \exp\left[-\int_0^{x'} (\alpha(x'') - \beta(x'')) dx''\right] dx} \tag{2.23}$$

where $\alpha(x)$ and $\beta(x)$ are the ionization coefficients that vary with position. In this model, electrons move in the positive x direction, while holes move in the negative x direction.

For an ideal *p-i-n* diode, where the electric field is uniform throughout the multiplication region, α and β are constant, simplifying the gain equation to:

$$M(x) = \frac{\exp[-(\alpha - \beta)x]}{1 - \int_0^w \alpha \exp\,[-(\alpha - \beta)x'] dx'} \tag{2.24}$$

This equation yields the familiar formulas for electron-initiated and hole-initiated multiplication factors, Me and Mh, when carriers are injected at the endpoints x=0 and x=w, respectively:

$$M_e = \frac{1}{1 - \frac{\alpha}{\alpha - \beta}\{exp[(\beta - \alpha)w] - 1\}} \tag{2.25}$$

$$M_h = \frac{1}{1 - \frac{\beta}{\alpha - \beta}\{exp[(\alpha - \beta)w] - 1\}} \tag{2.26}$$

The ratio of the ionization coefficients, $k = \beta/\alpha$, plays a pivotal role in determining both the multiplication gain and the response speed of the APD. When $k = 0$, the multiplication process is dominated entirely by electrons, as holes do not undergo further ionizations. In this single carrier multiplication scenario, the gain is given by:

$$M = e^{\alpha w} \tag{2.27}$$

In this case, the avalanche multiplication process ends once the electron transit time is completed, leading to a fast response time and minimal gain-bandwidth limitations. The gain can be controlled through the applied bias voltage, making it suitable for high-speed applications where rapid signal detection is required. Since the holes do not contribute to further ionization events, the excess noise is minimized, resulting in a lower noise level in the device.

On the other hand, when $k = 1$, both electrons and holes have equal probabilities of initiating ionization events, leading to double carrier multiplication. The gain in this case is given by:

$$M = \frac{1}{1-\alpha w} \tag{2.28}$$

This condition results in significantly higher gain compared to the single carrier case, as both electrons and holes contribute to the avalanche process. However, the extended duration of the avalanche multiplication process due to both carrier types participating results in a slower response time and a reduced gain-bandwidth product. Additionally, since both electrons and holes contribute to ionization, any fluctuations in the random path lengths of these carriers are amplified, leading to increased excess noise.

In practical APDs, the ionization rates for electrons and holes are rarely equal, and the actual multiplication lies between these two extremes[76], [77]. The relative values of α and β determine the feedback from the ionization process and directly influence the noise performance of the APD. A higher k ratio (where β approaches α) results in greater feedback from hole-initiated ionization, amplifying noise levels. Conversely, when k is small, the noise is reduced because fewer holes are involved in the multiplication process.

A critical factor in the multiplication process is the threshold energy E_{th}, which is the minimum energy a carrier must gain to initiate an impact ionization event. This energy is typically greater than the material's bandgap, as carriers must retain some of their energy and momentum after ionization. Anderson and Crowell[78] estimated that E_{th} is approximately 1.5 times the bandgap energy, E_g, assuming a simple parabolic band structure. However, due to the complexity of real semiconductor band structures, E_{th} is often treated as an adjustable parameter.

Another key aspect is the dead space effect, which refers to the minimum distance a carrier must travel before gaining enough energy to trigger impact ionization[79], [80]. In small devices, the dead space can occupy a significant portion of the multiplication region, reducing the effective gain. Carriers must first traverse this dead space before initiating further ionization events, which delays the onset of avalanche multiplication. This non-local effect is especially important in modern APDs with thin depletion regions, where the dead space reduces both the effective gain and the response speed.

2.5 Excess noise in APD

The performance of APDs is significantly impacted by excess noise, which originates from the intrinsic randomness of the avalanche multiplication process[74]. This noise plays a crucial role in determining the ultimate sensitivity and signal-to-noise ratio of APD-based detection systems.

The avalanche multiplication process is inherently stochastic, meaning that the number of carriers generated during each ionization event can vary greatly. This variability introduces fluctuations in the multiplication gain around the mean value, commonly referred to as the mean multiplication factor $\overline{M}$. These fluctuations generate excess noise, which ultimately limits the maximum effective gain of the APD and impacts the overall performance of the device.

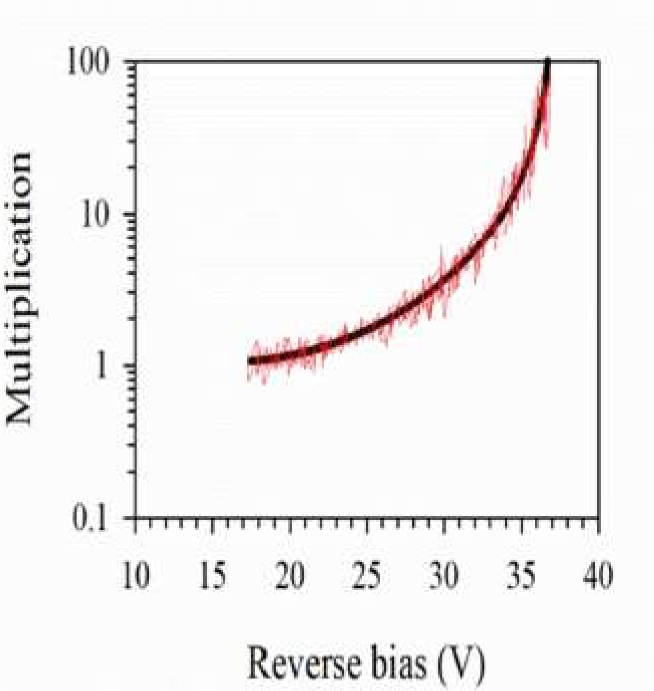

Fig. 2.9 diagram showing the fluctuation in the multiplication process.

Due to the random nature of the impact ionization process, the number of ionizing collisions within the multiplication region is also random. Consequently, the total number of carriers produced by a single injected carrier under a specific bias condition can exhibit a significant spread of values. This statistical fluctuation, stemming from the randomness in both the location of ionization events and the number of secondary carriers generated by the initiating carrier, results in a distribution of gain around a mean value. The gain M discussed in previous sections now represents the average or mean gain $\overline{M}$.

The fluctuations in gain can be characterized by the excess noise factor $F(M)$, which is related to the variance of gain $\sigma^2(M)$ by the following relationship:

$$F(M) = 1 + \frac{\sigma^2(M)}{\overline{M}^2} \tag{2.29}$$

This expression highlights how $F(M)$ is used to evaluate the additional noise introduced by the fluctuating gain in APDs. Alternatively, F(M) can also be expressed as:

$$F(M) = \frac{\overline{M^2}}{\overline{M}^2} \tag{2.30}$$

where $\sigma^2(M) = \overline{M^2} - \overline{M}^2$. In addition to excess noise, APDs also exhibit shot noise, which arises from the random fluctuations in the motion of carriers within the device.

2.5.1 McIntyre's Avalanche Noise Theory

McIntyre's theory of avalanche noise provides a fundamental framework for understanding the stochastic nature of the avalanche multiplication process in avalanche photodiodes (APDs)[74]. This theory offers a local model that describes how the probabilistic behaviour of carrier ionization events contributes to the overall noise within the device.

The core of McIntyre's theory is based on the assumption that the ionization coefficients for electrons (α) and holes (β) are constants, independent of the electric field. These ionization coefficients represent the likelihood of an electron or hole generating a secondary carrier via impact ionization as they traverse through the high-field region of the APD. The theory introduces the concept of the excess noise factor F, which quantifies the deviation from an ideal noiseless multiplication process.

According to McIntyre's model, the excess noise factor F is expressed as[74]:

$$F = kM + \frac{(1-k)(1-\frac{1}{M})}{M} + \frac{k^2(M-1)}{M^2} \tag{2.31}$$

where $k = \frac{\beta}{\alpha}$ is the ionization coefficient ratio, and M is the multiplication gain. This equation accounts for the fluctuations in the multiplication gain that arise due to the random nature of the ionization events. The excess noise factor F increases as the multiplication gain M increases, reflecting the fact that higher gains are associated with greater noise levels due to more frequent ionization events.

McIntyre's model provides two critical guidelines for minimizing excess noise in APDs:

1. The carrier species with the higher ionization coefficient should be preferentially injected into the multiplication region.
2. Operational parameters should be optimized to yield the smallest possible ionization coefficient ratio, $k = \beta/\alpha$.

These guidelines are derived from the analysis of the excess noise factor $F(M)$ as a function of k and the mean multiplication factor M. The relationship can also be expressed as:

$$F(M) = kM + (1 - k)(2 - \frac{1}{M}) \tag{2.32}$$

where k ranges from 0 to 1.

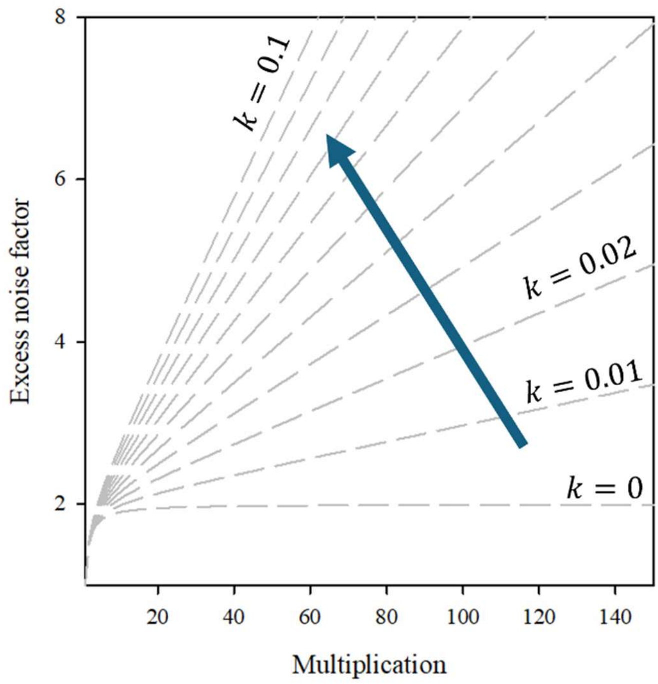

Fig. 2.10 McIntyre local model excess noise factor as a function of multiplication with different k values from 0 to 0.1 with a step of 0.01.

To illustrate the implications of this model, two boundary cases are considered:

Case 1: $\beta = 0$ $(k = 0)$

This represents the ideal scenario where only electrons contribute to the ionization process. The excess noise factor reaches its minimum value:

$$F(M) = 2 - \frac{1}{M} \tag{2.33}$$

High gain in this case requires a large αw, where w is the width of the multiplication region. This involves numerous electrons in the multiplication process, resulting in a statistically more stable gain.

Case 2: $\beta = \alpha \ (k = 1)$

This represents the scenario where electrons and holes contribute equally to the ionization process. The excess noise factor reaches its maximum:

$$F(M) = M \tag{2.34}$$

High gain is achieved with αw approaching unity, involving fewer carriers in the impact ionization process. This leads to larger variations in gain and higher excess noise.

The contrast between these cases highlights the importance of k in determining APD noise performance. Engineering devices to operate with a minimal k value can significantly reduce excess noise and enhance overall APD performance[21], [81].

McIntyre's theory also highlights the trade-off between gain and noise in the design and operation of APDs. While a higher multiplication gain M can enhance the sensitivity of the photodiode by amplifying the photocurrent, it simultaneously increases the noise, as quantified by the excess noise factor F. Therefore, optimizing APD performance involves balancing the desired gain with the acceptable noise levels to achieve the best possible signal-to-noise ratio (SNR) in practical applications.

Chapter 3 Methodology

3.1 Introduction

This chapter outlines the experimental techniques used to characterize the performance of avalanche photodiodes (APDs). The study involves several key measurements:

- Current-voltage (I-V) measurements were conducted to evaluate the electrical properties, such as breakdown voltage and leakage current, under both forward and reverse bias conditions.
- Capacitance-voltage (C-V) measurements provided insights into the doping profiles and depletion regions, crucial for understanding the charge distribution and built-in voltage of the devices.
- Photoresponce measurements were performed to determine the spectral response of the APDs, identifying their peak wavelength sensitivity and overall optical efficiency.
- Photomultiplication measurements were used to assess the voltage-dependent amplification of photocurrent, focusing on characterising the impact ionization process within the APDs.
- Excess noise measurements were carried out to quantify the additional noise generated during photomultiplication, providing a clear understanding of the noise performance and signal-to-noise ratio of the devices.

3.2 I-V Measurements

The current-voltage (I-V) measurements in this study were conducted using two primary instruments: the HP 4140 picoammeter and the Keithley 237 Source-Measure Unit (SMU). The HP 4140 provides a voltage source of up to 100 V, suitable for most samples. However, the Keithley 237, with its higher voltage capability of up to 1100V, was employed for specific layers, such as the InGaAs layers, which exhibited avalanche breakdown voltages greater than 100 V. All measurements were performed under dark conditions to prevent optical generation of carriers, ensuring that the results accurately reflected the intrinsic electrical properties of the devices.

Forward and reverse I-V characteristics were measured across different-sized mesa devices fabricated from each layer. The mesa devices were produced with nominal diameter determined by photolithography during the device fabrication process, ranging from 500µm to 50µm. These nominal values of diameter were used to calculate the device junction area (A), which is essential for determining current densities and capacitance characteristics, as detailed later in Section 3.3. The I-V measurements provided valuable insights into several key parameters, including breakdown voltage (V_{bd}), leakage current (I_s), bulk dark current (I_b), series resistance (R_s), and ideality factor (n). These parameters are crucial for assessing the quality of the materials and the effectiveness of the fabrication techniques.

The ideality factor (n) of a diode reflects how closely it follows the ideal diode model and provides insight into the dominant carrier transport mechanisms. Traditionally, it's extracted from the slope of the forward bias I-V characteristics in the exponential region. However, an alternative approach involves calculating the differential ideality factor, which can vary with applied voltage:

$$n(V) = \frac{q}{kT}\left(\frac{dV}{d[ln(I)]}\right) \tag{3.1}$$

Where $n(V)$ is the voltage-dependent differential ideality factor, q is the elementary charge, k is Boltzmann's constant, T is the absolute temperature, V is the applied voltage, and I is the measured current.

The ideality factor typically ranges from 1 to 2. A value close to 1 indicates that the current is dominated by diffusion, representing ideal diode behaviour. As n approaches 2, it suggests significant recombination in the space-charge region. Deviations from ideal behaviour can also occur due to non-ideal effects such as series resistance and leakage currents.

3.3 CV Measurements

Capacitance-voltage (C-V) measurements were performed to characterize the capacitance, built-in voltage (V_{bi}), and doping profile of APD devices. These measurements are essential for understanding the electronic properties of semiconductor junctions, particularly in devices with complex doping structures. By analyzing how capacitance varies with applied voltage, key parameters such as the depletion width and doping concentration can be extracted, providing insights into the material quality and device performance.

In devices with complex junctions, such as multi-region structures (e.g. *p-i-n* diodes or SACM structures), standard analytical models for simple junctions may not be sufficient. Therefore, advanced modelling techniques, such as solving Poisson's equation for multi-layered structures, are required. These methods allow for the accurate calculation of the electric field profile and capacitance in devices with varying doping levels and material properties across different regions.

The C-V measurements were carried out using an HP 4275A LCR meter in conjunction with a reverse biasing circuit provided by the HP picoammeter. This circuit was configured to apply a precise DC reverse bias voltage to the device under test (DUT), superimposed with a small sinusoidal AC test signal. The test signal had an amplitude of 50 mV and was applied at frequencies of 10 kHz, 100 kHz, and 1 MHz. These frequencies were selected to study the frequency dependence of the capacitance and to ensure accurate measurements under various conditions. The reverse bias voltage was supplied through the HP picoammeter, which was integrated into the measurement setup to provide stable and controllable biasing conditions, essential for accurately measuring the capacitance of the APD devices under varying reverse bias.

The capacitance of an APD device changes with the applied reverse bias voltage due to the variation in the depletion width within the device. The basic principle of capacitance involves two conductors separated by a dielectric material, where the capacitance C is given by:

$$C = \frac{\epsilon_0 \epsilon_r A}{W} \tag{3.2}$$

where ϵ_r is the relative dielectric constant of the material, ϵ_0 is the permittivity of vacuum, A is the area of the conductor, W is the depletion width.

As the reverse bias increases, the depletion region in the device widens, leading to a decrease in capacitance. This relationship allows the extraction of important parameters such as the built-in voltage (V_{bi}) and the doping profile of the semiconductor material.

The built-in voltage V_{bi} can be estimated by plotting $\frac{1}{C^2}$ versus the applied voltage V and extrapolating the linear portion of the plot to find the intercept on the voltage axis. This method assumes an abrupt, single-sided junction with constant doping density. However, in more complex junctions, such as those found in *p-i-n* diodes, this method serves as an approximation.

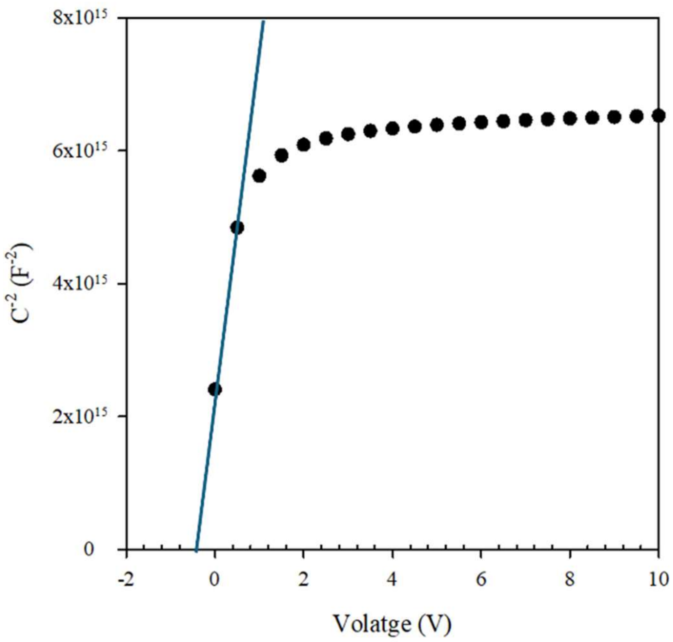

Fig. 3.1 $\frac{1}{C^2}$ vs. bias voltage obtained from the C-V measurement in a GaAsSb device.

The doping density $N(w)$ at a given position within the depletion region can be calculated from the slope of the $\frac{1}{C^2}$ versus V plot using the following relation:

$$N(w) = \frac{2}{q\epsilon_r\epsilon_0 A}\left(\frac{d\left(\frac{1}{C^2}\right)}{dV}\right) \tag{3.3}$$

where q is the elementary charge, ϵ_r and ϵ_0 are the relative and vacuum permittivity, respectively, A is the area of the diode. However, this method assumes a uniform permittivity across the entire device, which works well for simple junctions but becomes limited when applied to more complex structures, such as Separate Absorption Charge Multiplication (SACM) APDs. In SACM structures, different regions have distinct permittivities, making this assumption less accurate.

A more sophisticated approach involves modelling the C-V characteristics based on the known device structure. The input parameters include the widths of different regions, their respective permittivities, and doping densities. This method employs Poisson's equation to calculate the electric field and depletion profiles throughout the device. Poisson's equation for a semiconductor junction is:

$$\frac{dE(x)}{dx} = \frac{qN(x)}{\epsilon} \tag{3.4}$$

where E(x) is the electric field, N(x) is the doping concentration, and ϵ is the material's permittivity. In multi-region devices like SACM APDs, each region may have a distinct doping concentration and permittivity, necessitating a region-by-region calculation of the electric field.

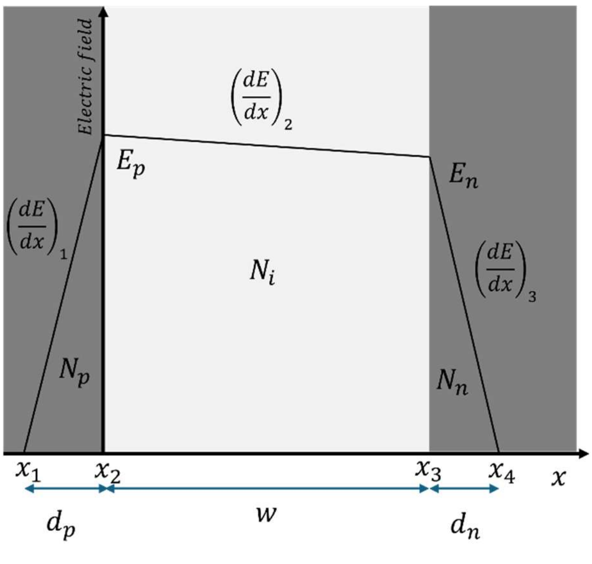

Fig. 3.2 The 3-region doping profile assumed in the C-V fitting.

For example, in a three-region structure, the electric field in each region is calculated as:

$$\left(\frac{dE}{dx}\right)_1 = \frac{qN_p}{\epsilon_p} \tag{3.5}$$

$$\left(\frac{dE}{dx}\right)_2 = \frac{qN_i}{\epsilon_i} \tag{3.6}$$

$$\left(\frac{dE}{dx}\right)_3 = \frac{-qN_n}{\epsilon_n} \tag{3.7}$$

The total reverse bias voltage V_t applied across the device is the sum of the voltage drops across each region, given by the area under the electric field profile:

$$V_t = \int_{x_1}^{x_2} E(x)dx + \int_{x_2}^{x_3} E(x)dx + \int_{x_3}^{x_4} E(x)dx \tag{3.8}$$

This method extends to more complex devices with multiple regions. For example, in SACM APDs, which may have four or five distinct regions, the solver generalizes the field calculations. The thickness and doping density of each region are taken into account, and Poisson's equation is solved for the entire structure. In a five-region SACM APD, the electric field equations are extended:

$$\left(\frac{dE}{dx}\right)_4 = \frac{qN_4}{\epsilon_4} \tag{3.9}$$

$$\left(\frac{dE}{dx}\right)_5 = \frac{qN_5}{\epsilon_5} \tag{3.10}$$

By solving these equations, the depletion width and electric field profile across the device are calculated. This model then generates a theoretical capacitance curve, which can be compared to the experimentally measured C-V data. By iteratively adjusting the input parameters (doping concentrations, layer thicknesses, etc.), the model fits the theoretical data to the experimental results.

This Poisson-based approach is particularly well-suited for SACM APDs, where different regions have varying permittivities and doping profiles. By accurately solving the electric field distribution, this method provides a precise representation of the capacitance, accounting for complex material properties and structure. This results in a more reliable extraction of device parameters, such as doping concentrations and region thicknesses, compared to simpler models that assume uniform material properties.

3.4 Photocurrent Measurements

Photocurrent measurements are essential for evaluating the photoresponse of photodiodes by determining how effectively the device converts incident light into an electrical signal. This section outlines the methodology used to measure the photo-response of photodiodes, focusing on the setup and operation of the instrumentation, including the monochromator and lock-in amplifier (LIA), which are critical for achieving accurate and reliable measurements.

The measurement setup consisted of several key components: a Horiba Scientific iHR320 Czerny-Turner monochromator, a Keithley 236/237 Source-Measure Unit (SMU), a Stanford Research SR830 lock-in amplifier (LIA), a mechanical chopper, and a desktop computer with a data acquisition module (DAM). The iHR320 monochromator was used to generate monochromatic light by splitting polychromatic light into individual wavelengths with a reflective diffraction grating, which operates based on the interference principle. The monochromatic light was then directed onto the device under test (DUT) to assess its spectral response.

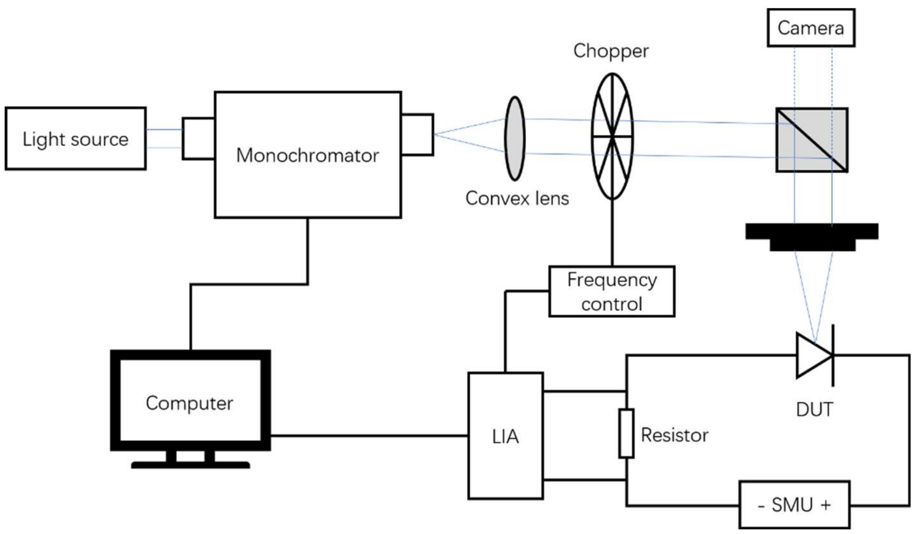

Fig. 3.3 The schematics of the photocurrent setup.

As shown in Figure 3.3, the iHR320 monochromator focuses polychromatic light onto the entrance slit using a concave mirror. The light is collimated, passed through a diffraction grating to separate it into its constituent wavelengths, and then refocused by a second concave mirror onto the exit slit. The desired wavelength is selected by adjusting the grating angle via computer control, ensuring that the focused monochromatic light exits the slit and illuminates the device under test (DUT). To maximize light throughput, the F-number of the tungsten lamp housing and the collimating lens was matched to that of the monochromator.

The tungsten bulb, used as the light source, provides a relatively smooth spectrum in the visible range, although its intensity varies with wavelength due to the blackbody radiation response and the grating's efficiency. Once generated, the monochromatic light is mechanically chopped at a frequency optimized to avoid interference with the line frequency and to match the response characteristics of the DUT. The modulated light beam is then focused on the DUT's optical window using a microscope objective, and the resulting photocurrent is measured through the voltage drop across a series resistor, using a lock-in amplifier (LIA) synchronized with the chopper's reference frequency.

The LIA output voltage, V_{LIA}, is given by:

$$V_{LIA} = LIA\ Reading \times \frac{10}{Sensitivity\ of\ LIA} \tag{3.11}$$

This output was digitized by the DAM and read by the desktop computer for further analysis.

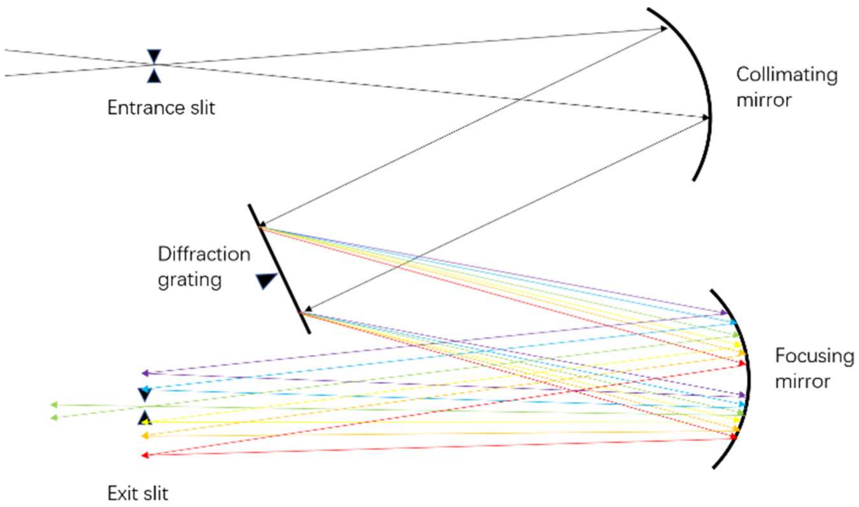

Fig. 3.4 Schematic of the diffraction process in the monochromator.

The iHR320 monochromator uses a blazed holographic diffraction grating optimized for a blaze wavelength of 1000 nm, aligning well with the peak response of the DUTs at approximately 1500 nm. The grating equation governing the diffraction process is:

$$\sin(\theta_i) + \sin(\theta_r) = m\frac{\lambda}{d} \tag{3.12}$$

where θ_i and θ_r are the incident and reflective angles, respectively, m is the diffraction order, λ is the wavelength, d is the groove spacing of the grating. To avoid detecting undesired wavelengths corresponding to higher-order diffractions ($m > 1$), a 1150 nm long-pass colour filter was used.

During the measurement process, the monochromatic light was directed onto the DUT while varying the wavelength to map the photo-response across different spectral regions. The DUT was reverse biased using the Keithley 236/237 SMU, and the photocurrent generated was measured by the LIA, which amplified the AC signal corresponding to the chopped light and separated it from the DC background. Due to the non-point source nature of the tungsten bulb, the focused spot size was approximately 1 mm × 2 mm, meaning only a fraction of the incident light illuminated the DUT's optical window.

Calibration of the incident power was performed using a commercial photodiode (Thorlabs FD05D) with a photosensitive area similar to the largest DUTs. The measured power was then scaled according to the area ratio to estimate the power incident on the DUT, ensuring accurate responsivity measurements.

The LIA was crucial for enhancing the signal-to-noise ratio (SNR) by selectively amplifying the AC component of the photocurrent at the chopper frequency while suppressing noise. The reference frequency for the LIA was provided by the chopper controller, and the input signal V_t, after synchronizing the phase of the input and reference signals, is given by:

$$V_t = \frac{2V_a}{\pi} \tag{3.13}$$

where V_a is the amplitude of the input signal. This output was then processed to extract the photocurrent signal, isolating it from the dark current and noise contributions.

The LIA low-pass filter (LPF) further refined the signal by removing higher-frequency noise, with the time constant τ adjusted to ensure a stable reading without excessively prolonging the measurement time. The integration time on the PC was set to 3τ to allow the LIA output to reach 95% of its final value, ensuring accurate and reliable photocurrent measurements.

3.5 Photomultiplication Measurements

Photomultiplication is a key process in avalanche photodiodes (APDs) and other high-sensitivity photodetectors, where the photocurrent is amplified due to impact ionization under a reverse bias. Understanding this process is critical for optimizing the performance of such devices. This section describes the methodology used to measure photomultiplication in the device under test (DUT), detailing the experimental setup, the principles of measurement, and the method for extracting ionization coefficients α and β.

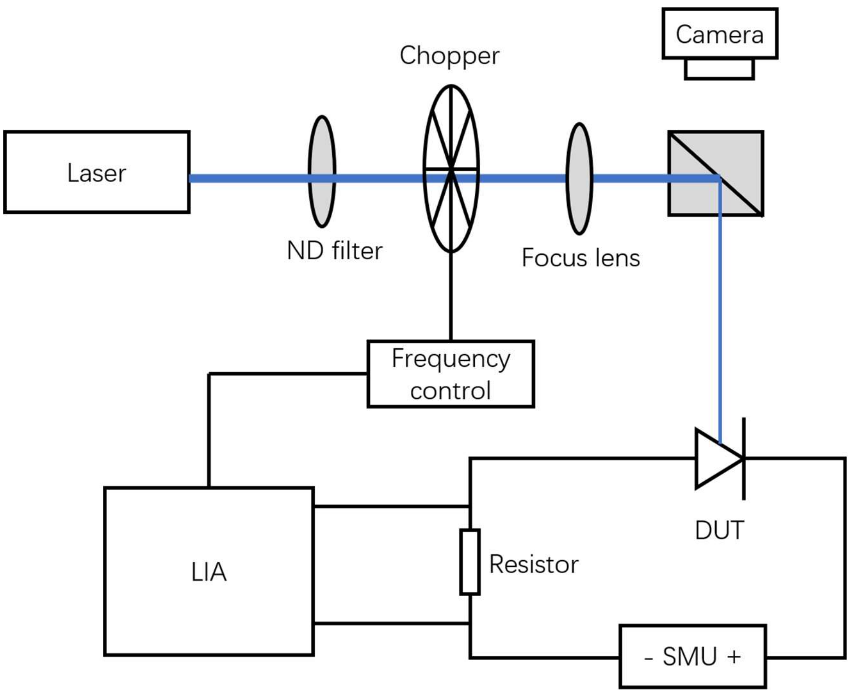

Fig. 3.5 The schematics of the photocurrent measurement setup.

The photomultiplication measurement setup, depicted in Figure 3.5, consists of a laser or LED light source modulated at 180 Hz to enable phase-sensitive detection (PSD). The DUT is reverse-biased using a Keithley 236/237 Source-Measure Unit (SMU), which controls the applied voltage and measures the resulting current. The modulated optical signal is synchronized with a reference AC signal of the same frequency. The photovoltage signal, corresponding to the modulated photocurrent, is then measured using a lock-in amplifier (LIA), which filters out noise and unwanted signals for precise photocurrent measurement.

In a reverse-biased *p-i-n* diode, photomultiplication occurs when charge carriers generated by illumination (electrons and holes) are accelerated in a high reverse electric field, leading to impact ionization. When the diode is illuminated, light is absorbed in the p^+ cladding layer, generating electron-hole pairs. The photo-generated holes are quickly collected, while the minority carriers (electrons) diffuse toward the intrinsic i-region. Electrons that avoid recombination are injected into the i-region, where the high reverse electric field may cause them to undergo impact ionization, amplifying the primary current I_{pri} by a multiplication factor M_e. This amplified current, I_{ph}, is the reverse photocurrent measured by the LIA.

The avalanche multiplication factor $M(V)$ at a given reverse bias voltage V is calculated as:

$$M(V) = \frac{I_{ph}(V)}{I_{pri}} \tag{3.8}$$

where $M(V)$ is the multiplication factor at the specific reverse bias voltage V, I_{pri} is the primary photocurrent, measured at $V = 0$ V, $I_{ph}(V)$ is the photocurrent at the given reverse bias V.

The measurement procedure involves varying the reverse bias applied to the DUT while illuminating it with modulated light. I_{pri} is measured at V=0 V, and the corresponding I_{ph} is measured at different biases. The photocurrent I_{ph} is determined using the equation:

$$I_{ph} = \frac{V_{ph}}{R} \tag{3.9}$$

where V_{ph} is the photovoltage across a series resistor R. The choice of R is crucial; it must be small enough (typically 100 Ω) to minimize voltage drop but large enough to ensure a detectable signal.

Beyond standard photomultiplication measurements, ionization coefficients α and β can be extracted by analysing how $M(V)$ varies with different wavelengths of illumination. Shorter wavelengths are absorbed near the surface, generating electron-hole pairs closer to the high electric field region, while longer wavelengths penetrate deeper into the structure, generating carriers further from the field. For example, 99% of 455 nm light is absorbed within the InAlAs p^+ cladding layer, whereas longer wavelengths create carriers deeper in the device. This depth-dependent carrier generation allows for the estimation of α and β by observing the differences in $M(V)$ with varying wavelengths.

In materials where $\alpha > \beta$, avalanche multiplication increases more rapidly with shorter wavelength illumination because more electrons, which have a higher ionization probability, are generated closer to the high field region. Conversely, longer wavelengths generate more holes, which have a smaller ionization coefficient, leading to lower overall multiplication. This wavelength-dependent behavior provides a powerful method for estimating α and β, offering valuable insights into the material properties and design of APDs.

3.6 Excess Noise Measurement

To experimentally determine the excess noise factor F, a precise measurement of the noise power in the DUT is required. The experimental setup is designed to isolate and measure this noise by focusing on key variables, such as the photocurrent and its variance, under controlled conditions.

The excess noise measurement setup, depicted in Figure 3.6, is adapted from the design by Lau et al.[82], specifically tailored to assess the noise characteristics of APDs. In this setup, a laser source, mechanically chopped at a frequency of 180 Hz, illuminates the DUT. The laser light is focused onto the DUT, which has a diameter greater than 200 µm, producing a spot size of approximately 100 µm. The photocurrent generated by the DUT is amplified by a low noise transimpedance amplifier (TIA) with a gain of 2.2 kV/A, converting the photocurrent into a proportional square wave voltage signal at the reference frequency. To avoid saturation of the TIA, the input photocurrent is carefully limited to 1.7 mA.

The chopping frequency of 180 Hz was selected to ensure that the modulated light signal falls well within the detection bandwidth of the lock-in amplifier, minimizing interference from environmental noise sources such as power line frequency (50 Hz). The gain of the transimpedance amplifier was set to 2.2 kV/A to achieve a balance between sensitivity and dynamic range, ensuring accurate measurement of the photocurrent without saturating the amplifier.

Following amplification, the voltage signal from the TIA is passed through a low-pass band filter with a centre frequency of 10 MHz and a bandwidth of 4.2 MHz. This filtering process effectively removes the high-frequency noise associated with the chopped signal, allowing the filtered signal to be further amplified for analysis.

The amplified signal is then fed into a noise power meter, which converts it into a mean square value representing the combined noise from impact ionization, dark current shot noise, and system noise. A lock-in amplifier is used to measure the noise power from the noise power meter, providing precise isolation of the relevant noise contributions. To prevent signal clipping during high noise measurements, an attenuator is placed between the amplifier output and the noise power meter, ensuring accurate noise power readings.

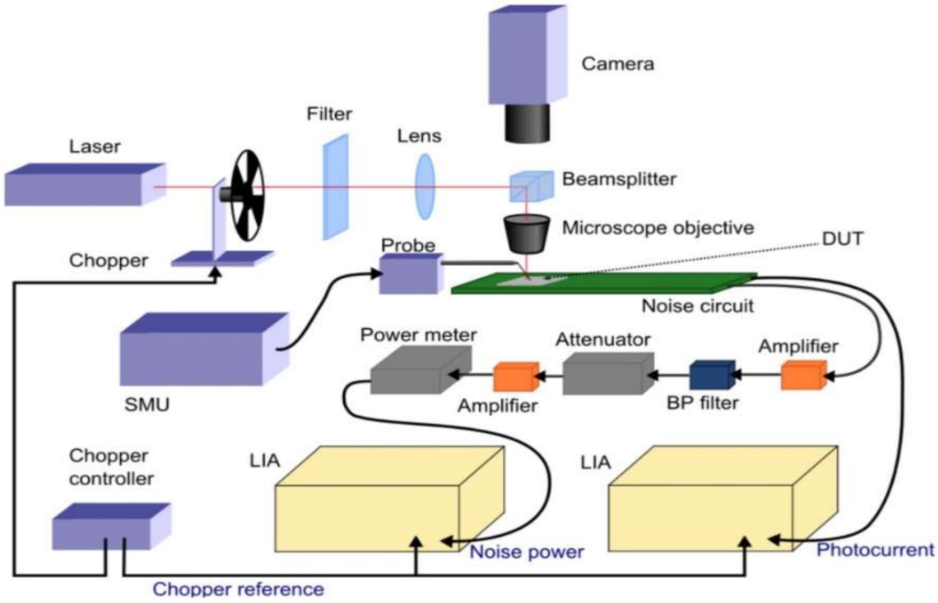

Fig. 3.6 The schematics of the excess noise setup.

The excess noise factor F is a key parameter that quantifies the deviation of the noise power from that expected in an ideal APD. F is defined as the ratio of the noise power from the device under test N_{dut} to the noise power expected from an ideal APD N_{ideal}:

$$F = \frac{N_{dut}}{N_{ideal}} \tag{3.13}$$

where N_{dut} is the measured noise power of the device under test, N_{ideal} is the noise power expected from an ideal APD.

Although N_{ideal} cannot be directly measured, it can be predicted using a non-avalanching silicon *p-i-n* diode. Unlike APDs, which exhibit noise due to stochastic impact ionization, the noise from a silicon *p-i-n* diode primarily originates from shot noise, making it an ideal baseline for comparison. The ideal shot noise power N_{ideal} for a primary current i_{pr} and multiplication factor M is given by:

$$N_{ideal} = 2ei_{pr}BM^2G \tag{3.14}$$

where B is the effective noise bandwidth, G is the system gain, and e is the electronic charge.

This establishes the physical basis for ideal shot noise using a silicon *p-i-n* diode as a reference. In practice, shot noise is measured and the relationship between shot noise power and primary photocurrent is calibrated using a linear fit. The slope of this fit gives k_{ref}, the shot noise per unit photocurrent. Variations in temperature or system gain can cause slight changes in k_{ref}, so calibration is typically done immediately before or after key measurements. The shot noise is linearly proportional to the primary photocurrent and is described by:

$$N_{shot} = k_{ref} I_{primary} + c \tag{3.15}$$

where c accounts for baseline or offset noise in the system.

In avalanche photodiodes (APDs), noise contributions come from both shot noise and excess noise. The excess noise factor F quantifies how much additional noise is introduced beyond the intrinsic shot noise due to stochastic variations in the avalanche gain process. The total measured noise power output for an APD is given by:

$$N_{APD} = 2qI_{pr}FM^2B \tag{3.16}$$

where I_{pr} is the primary photocurrent, M is the avalanche gain, q is the electronic charge, and B is the system's measurement bandwidth. This expression highlights how noise scales with both the photocurrent and the multiplication factor. Rearranging this equation allows us to isolate the excess noise factor as:

$$F = \frac{N_{APD}}{2qI_{pr}M^2B} \tag{3.17}$$

making it possible to compare the noise generated by the APD with that of an ideal noise source.

Since direct measurement of shot noise requires calibration, k_{ref} becomes crucial in relating the measured noise power to the photocurrent. In this context, the term $2qI_{pr}B$ is replaced with $I_{pr}k_{ref}$, leading to a simplified expression for the excess noise factor:

$$F = \frac{N_{APD}}{I_{pr}k_{ref}M^2} \tag{3.18}$$

This relationship shows that k_{ref}, obtained through the calibration process, normalizes the noise measurements against the reference shot noise, allowing for accurate comparison between different APDs or devices.

Additionally, variations in the system's effective noise bandwidth (ENBW), which change with device capacitance, must be accounted for. As the capacitance of the APD changes with bias, the system's response—and thus the noise bandwidth—also changes. This variation can significantly affect noise measurements. The noise bandwidth correction is applied to the excess noise factor equation, resulting in:

$$F = \frac{N_{APD} B(C_{APD})}{I_{pr} k_{ref} M^2 B(C_{ref})} \tag{3.19}$$

where $B(C_{APD})$ represents the bandwidth as a function of the APD's capacitance, and C_{ref} is the capacitance of the reference device used for calibration. This final adjustment ensures that the noise measurements remain accurate, even as device characteristics such as capacitance vary during testing.

By incorporating these factors—shot noise calibration through k_{ref}, the influence of the excess noise factor, and corrections for bandwidth changes due to capacitance—the noise measurements from APDs can be precisely characterized. This method provides a robust framework for evaluating APD performance across different conditions and ensures that the results are reliable and comparable.

3.7 Device fabrication methods

The fabrication of semiconductor devices involves a series of precise steps, each crucial for the device's final performance. This section outlines the process used to fabricate the devices studied in this research, detailing specific solvents and equipment employed.

The process begins with cleaving the semiconductor wafers into appropriately sized pieces. These pieces undergo a thorough three-stage solvent cleaning process using: n-Butyl Acetate ($C_6H_{12}O_2$), Acetone (C_3H_6O) and Isopropyl Alcohol (C_3H_8O). Each solvent serves to remove different types of contaminants from the wafer surface, ensuring a clean substrate for subsequent processing steps.

Following the cleaning process, metal contacts are deposited on the wafer using a high-vacuum evaporation system. For this research, the metal contact typically comprised of 20 nm of Titanium (Ti) and 200 nm of Gold (Au). This combination often forms a Schottky contact with n-doped semiconductor substrates, though the specific electrical characteristics depend on the substrate material and doping.

Photolithography is performed using a standard UV exposure system. The process begins with spin-coating photoresist onto the wafer surface, typically using a bilayer of PMGI and SPR350 in this research. The photoresist is then exposed to UV light through a patterned metal mask. Following exposure, the photoresist is developed using MF26A developer diluted in distilled water (ratio 1:0.7; MF26A: DIW). This photolithography process is repeated multiple times during fabrication to create different patterns for various device layers or features, allowing for precise control over the device geometry and structure.

Following photolithography, additional Ti/Au metal layers are deposited using the high-vacuum evaporation system. A lift-off procedure is then performed in a beaker of acetone, sometimes aided by gentle agitation or the use of a pipette to introduce air bubbles, ensuring the removal of excess metal and undeveloped photoresist.

The mesa etching process is crucial for isolating individual devices on the wafer. The wet etching recipe used in this study consists of either [1 ml HCl]: [8 ml H_2O_2]: [80 ml H_2O] or [1 ml H_2SO_4]: [8 ml H_2O_2]: [80 ml H_2O], depending on the materials to be etched. For more complex structures like SACM APDs, multiple etching stages are sometimes necessary due to the different layers involved. The etch depth is monitored using a Dektak Stylus Profiler, and the process is repeated as needed to achieve the desired thickness. This approach allows for precise control over the device structure while accommodating the varying etch rates of different semiconductor materials.

To protect the devices and prevent oxidation, a passivation layer is applied using SU-8 negative photoresist. The process begins by coating the sample with SU-8, followed by the application of a mesa mask pattern. The sample is then exposed to UV light, which hardens the exposed photoresist. Subsequently, an SU-8 developer is used to dissolve the unexposed areas, leaving hardened photoresist around the optical windows. This passivation technique effectively protects the device structure while maintaining access to the crucial optical interfaces.

Throughout the fabrication process, various characterization techniques, including profilometry and microscopy, are employed to monitor and control the quality of each fabrication step. While these specific materials and techniques were used in this research, it's worth noting that the exact chemicals, exposure times, or metal thicknesses may be optimized based on particular device requirements and materials involved in other studies.

Chapter 4: The Absorption Coefficient in GaAsSb and InGaAs

4.1 Introduction

Understanding the optical absorption coefficient is crucial for the design and optimization of optoelectronic devices such as photodetectors (PDs), avalanche photodiodes (APDs), and modulators. The absorption coefficient determines how efficiently a material absorbs light, which directly impacts the performance of devices that operate in the infrared spectrum, particularly around 1550 nm—a key wavelength used in telecommunications.

$GaAs_{0.5}Sb_{0.5}$ and $In_{0.53}Ga_{0.47}As$ (hereafter referred as GaAsSb and InGaAs) are two semiconductor materials with direct bandgaps of approximately 0.75 eV, making them ideal for absorption in the infrared range. Both materials can be grown lattice-matched to Indium Phosphide (InP), which is critical for achieving high-quality epitaxial layers with minimal defects, further enhancing their performance in photonic devices. GaAsSb and InGaAs have become promising candidates for telecommunications applications, particularly in systems that operate over the C-band (1530 nm ~ 1565 nm) and L-band (1565 nm ~ 1625 nm) due to their efficient light absorption near these wavelengths.

The absorption properties of InGaAs have been extensively studied. Transmission measurements on epitaxially grown InGaAs samples have shown absorption coefficients ranging from 30,000 cm^{-1} to 20 cm^{-1} across wavelengths from 1000 nm to 1700 nm[83]. Studies by researchers such as Humphreys et al.[84] and Zielinski et al.[85] have demonstrated that doping concentrations, layer thickness, and band structure significantly influence the material's absorption characteristics. Further investigations by Hahn et al.[86] highlighted how electron doping affects intrinsic absorption in InGaAs, shifting the absorption edge due to phenomena like band-filling and band-gap shrinkage.

In contrast, research on the absorption properties of GaAsSb has been more limited. Initial work by Park and Jang[38] used transmission measurements on a 1 µm GaAsSb/InP heterostructure layer grown by metalorganic vapor-phase epitaxy (MOVPE). However, comprehensive data on GaAsSb's absorption coefficient across various conditions and device structures is still lacking. Given the material's potential for telecom applications, there is a pressing need to explore its absorption behaviour more thoroughly, especially when compared to the well-studied InGaAs.

As the demand for increased network bandwidth and capacity grows, the ability to expand operational wavelengths in optical fibres beyond the traditional C-band into the L-band has become a priority[87]. This expansion places greater emphasis on materials like GaAsSb and InGaAs, whose absorption coefficients at these wavelengths are critical for the performance of key devices, including photodiodes and APDs.

In this chapter, we investigate and compare the absorption characteristics of GaAsSb and InGaAs, two semiconductor materials critical for optoelectronic applications. By analyzing wavelength-dependent photocurrents from p+-i-n+ structures, we obtained absorption coefficients over a wavelength range of 1200 nm to 1830 nm. The results demonstrate that both materials exhibit comparable absorption coefficients, particularly at the telecom-relevant wavelength of 1550 nm, with GaAsSb and InGaAs showing values of 8400 cm^{-1} and 8100 cm^{-1}, respectively. Additionally, the Urbach energies of the two materials were examined, revealing a slight difference. GaAsSb demonstrated a higher Urbach energy compared to InGaAs, indicating a broader absorption tail.

4.2 Device structures

Table 4.1 The layer details of the two GaAsSb p-i-n photodiodes.

Layer	Material	Description	Doping density (cm^{-3})	Thickness (nm)	
				GaAsSb-A	GaAsSb-B
6	InGaAs	p^{++} contact	1×10^{19}	20	20

5	InAlAs	p^+ cladding	2×10^{18}	150	300
4	GaAsSb	p^+ cladding	2×10^{18}	20	20
3	GaAsSb	UID	1×10^{15}	1000	1800
2	GaAsSb	n^+ cladding	2×10^{18}	100	100
1	InAlAs	n^+ cladding	1×10^{19}	500	500
0	InP	Substrate	SI	-	-

Table 4.2 The layer details of the two InGaAs p-i-n photodiodes.

Layer	Material	Description	Doping density (cm^{-3})	Thickness (nm)	
				InGaAs-A	InGaAs-B
6	InGaAs	p^{++} contact	1×10^{19}	20	20
5	InP	p^+ cladding	2×10^{18}	500	500
3	InGaAs	UID	1×10^{15}	1800	4800
2	InP	n^+ cladding	2×10^{18}	100	100
1	InAlAs	n^+ cladding	1×10^{19}	500	500
0	InP	Substrate	SI	-	-

In this study, two *p-i-n* structure photodiodes of InGaAs and two of GaAsSb were grown using Metalorganic Vapour-Phase Epitaxy (MOVPE) and Molecular Beam Epitaxy (MBE), respectively.

The GaAsSb devices are labelled GaAsSb-A and GaAsSb-B, with intrinsic layer thicknesses of 1.0 µm and 1.8 µm, respectively. Their structures are detailed in Table 4.1. For the InGaAs devices, labelled InGaAs-A and InGaAs-B, the intrinsic layer thicknesses are 1.8 µm and 4.8 µm, respectively, with their layer details provided in Table 4.2. These variations in thickness allow for comparative analysis of electric field distribution and absorption properties in both GaAsSb and InGaAs materials.

Each structure consists of highly doped (>10^{18} cm^{-3}) p^+ and n^+ cladding layers at the top and bottom to facilitate efficient carrier injection and collection. The InGaAs devices use InP for the cladding layers, while the GaAsSb devices use InAlAs cladding layers. Both materials ensure that no light absorption occurs in the cladding regions over the wavelength range of interest, particularly around 1550 nm. A 20 nm highly p^+ doped InGaAs contacting layer was used for all devices to provide low-resistance electrical contacts.

The fabrication process began with wafer cleaving and cleaning, followed by the deposition of a back metal contact using a high-vacuum evaporation system. This contact, made from 20 nm Titanium (Ti) and 200 nm Gold (Au), formed a Schottky contact with the *n*-doped InP substrate, ensuring low resistance and efficient charge transfer.

After preparing the wafer surface, a standard photolithography process was employed to define the contact areas and mesa structures. A layer of photoresist was spin-coated, exposed to UV light, and developed using a diluted MF26A developer. A Ti/Au metal layer was then evaporated onto the top surface of the wafer to form the contacts. Excess metal and undeveloped photoresist were removed using a lift-off process in acetone.

The mesa structures were defined through additional photolithography steps, followed by wet etching using a citric acid-based solution. The mesa diameters were varied from 500 µm to 60 µm to study the effect of geometry on the device performance. The thickness of the etched layers was measured using a stylus profiler to ensure precise control over the fabrication process.

To protect the devices from environmental degradation and minimize surface recombination, the sidewalls were passivated with SU-8 negative photoresist, which was patterned and exposed to UV light. This coating formed a protective layer around the optical windows, ensuring stable long-term device performance.

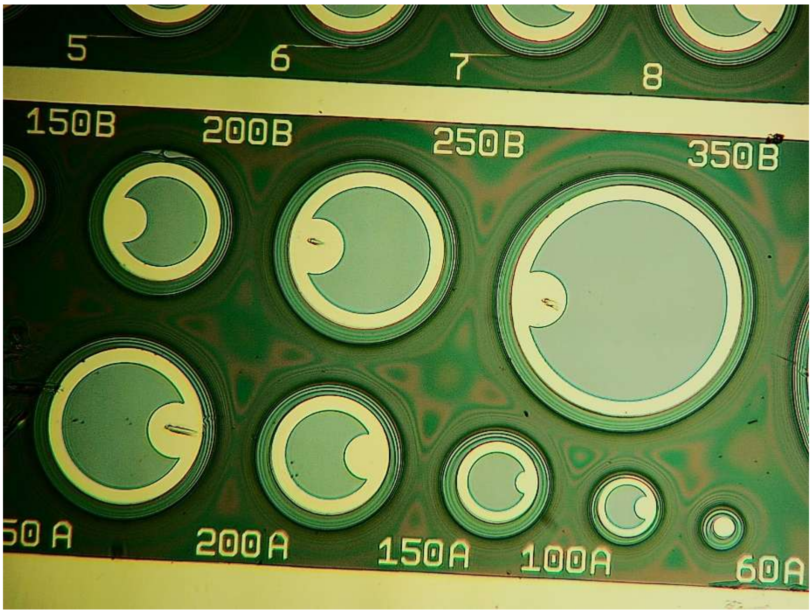

Fig. 4.1 Image of the fabricated GaAsSb photodiodes, with circular shape mesa, metal contact and optical window.

X-ray Diffraction (XRD) was employed to verify the crystal quality and lattice matching of the GaAsSb layers with the InP substrates. The results, shown in Figure 4.2, indicate high-quality epitaxial growth with well-defined peaks corresponding to GaAsSb, InAlAs, and the InP substrate. Both GaAsSb-A and GaAsSb-B samples show good lattice matching, with minimal strain evident from the peak positions. However, slight variations in the intensity and sharpness of the GaAsSb peaks suggest minor differences in crystal quality between the two samples. These results confirm that the precise control over the growth conditions provided by the MBE system ensures uniformity in layer composition and thickness, which is critical for achieving consistent device performance and extracting reliable characteristics.

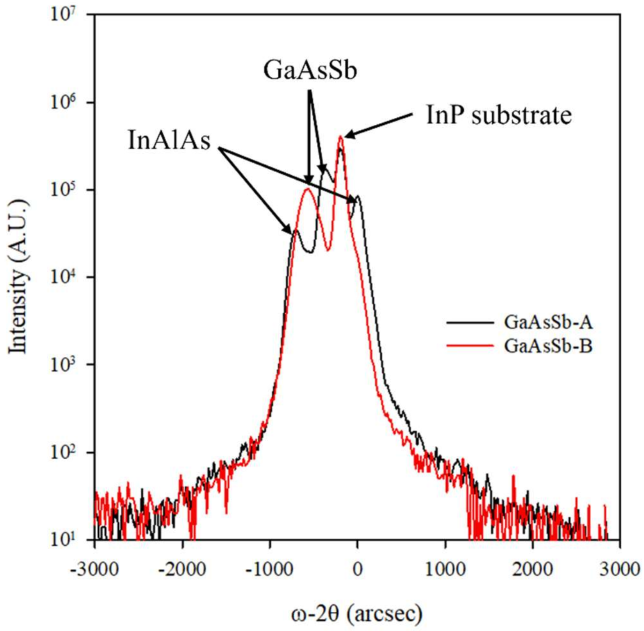

Figure 4.2 High-resolution X-ray diffraction (HRXRD) of GaAsSb layers grown on InP substrates, comparing samples GaAsSb-A (black) and GaAsSb-B (red).

4.3.1 Capacitance voltage characteristics

To confirm the background doping and intrinsic layer widths, capacitance-voltage measurements were undertaken as shown in Fig. 4.3. For all the layers, the capacitance scales with area and reduces rapidly within 1 V indicating that the background doping level in the intrinsic region is low. The low background doping in all these structures means that the electric field (and therefore the absorption coefficient) can be assumed to be constant across the depletion region, simplifying the later experimental analysis.

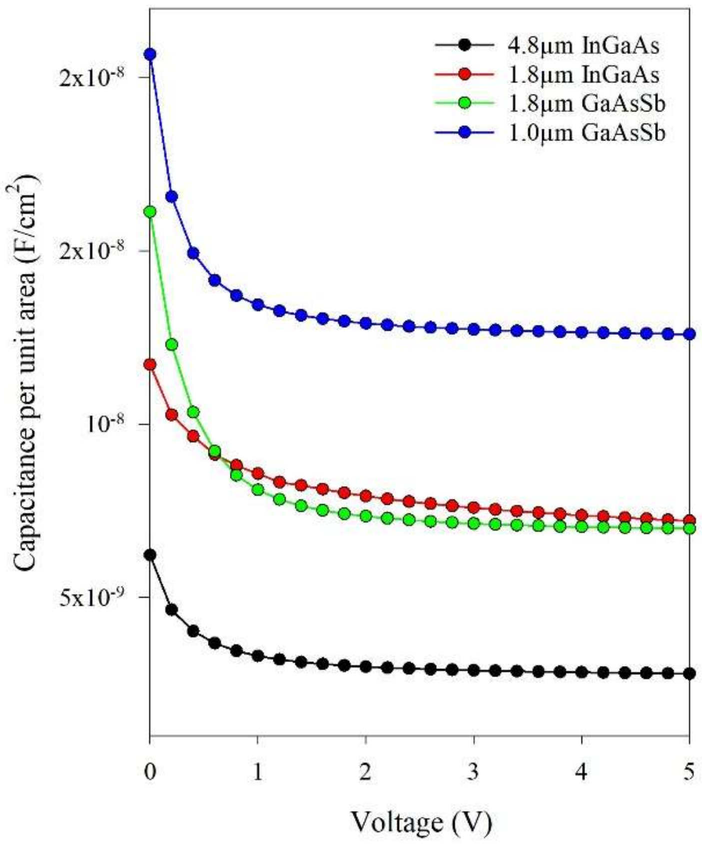

Figure 4.3 The capacitance-voltage measurements of InGaAs and GaAsSb heterojunction photodiodes.

Fig.4.4 shows the doping density as a function of depletion width calculated using Eqn. (3.3) in the two InGaAs and two GaAsSb diodes, using their respective permittivity[88]. For 4.8 µm InGaAs, the doping density starts around 1×10^{14} cm^{-3} at a depletion width close to 2.6 µm and increases gradually, reaching approximately 1×10^{16} cm^{-3} at around 4.8 µm. For 1.8 µm InGaAs, the doping density begins near 1×10^{15} cm^{-3} at a depletion width of around 1.1 µm, increasing to about 2×10^{16} cm^{-3} as the depletion width approaches 1.8 µm. For 1.8 µm GaAsSb, the doping density starts at approximately 9×10^{14} cm^{-3} at a depletion width near 1.0 µm, increasing steadily to slightly below 1×10^{18} cm^{-3} as the depletion width nears 1.8 µm. For 1.0 µm GaAsSb, the doping density is around 2×10^{15} cm^{-3} at a depletion width of about 0.8 µm, showing a steep rise and exceeding 1×10^{18} cm^{-3} at around 1.0 µm.

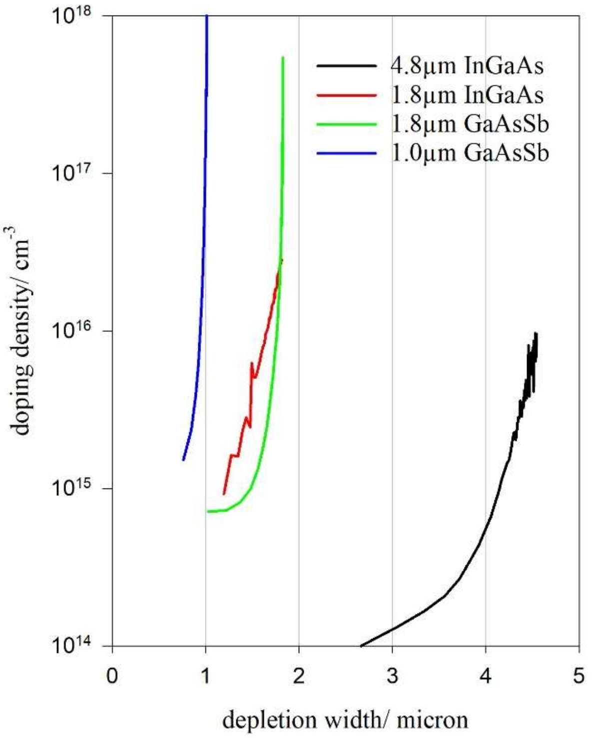

Figure 4.4 the doping density profile calculated from capacitance measurements.

While Fig. 4.4 suggests that the 4.8 μm InGaAs diode has a much lower intrinsic doping than the other samples, this may not accurately reflect the actual doping profiles. The differences observed can be attributed to several factors related to the growth process and measurement techniques. Epitaxy is known for its precise control over material composition and doping levels, and under stringent growth conditions, significant variations in UID levels between samples are unlikely. Minor differences due to variations in substrate quality or chamber conditions can occur, but substantial doping differences are improbable.

Additionally, the built-in voltage in *p-i-n* diodes creates an initial depletion region, especially in thinner devices like the 1.0 μm GaAsSb. This can result in higher apparent doping densities at small depletion widths due to the strong initial depletion, which may explain the lower apparent doping in the thicker 4.8 μm InGaAs. Furthermore, the "Debye blurring" effect[46], which refers to the diffusion of charge carriers over the Debye length, can reduce the spatial resolution of capacitance-voltage measurements, particularly in thinner devices like GaAsSb.

Given the controlled MBE growth conditions, the actual UID levels should remain uniformly low across all devices. This is supported by the raw capacitance data, which drops rapidly within 1 V, indicating low background doping in the intrinsic region. Therefore, the observed variations in doping are likely due to measurement artifacts or built-in voltage effects, particularly in the thinner devices.

The low intrinsic doping enables relative uniform electric field inside the intrinsic region, as shown in Fig. 4.5, the electric field calculated for the intrinsic region in the 4.8µm InGaAs at 100V is fairly uniform, varying only from 195 kV/cm to 208 kV/cm.

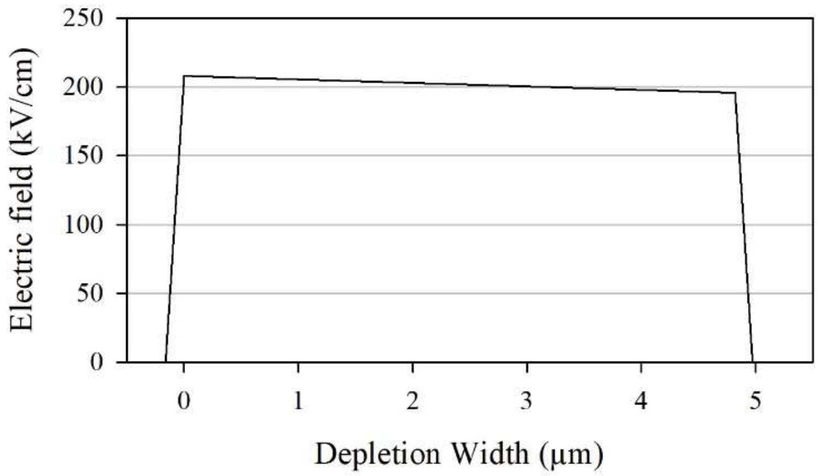

Fig.4.5 The electric field profile of the 4.8µm InGaAs at 100V

4.3.2 Current voltage characteristics

The forward and reverse dark current measurements were performed on the 1 µm GaAsSb and 4.8 µm InGaAs diodes using the techniques described in the previous chapter. The results are displayed in Fig. 4.6 and Fig. 4.7. These measurements are crucial for understanding the quality of the p-i-n junctions and the dominant recombination mechanisms within the devices.

The forward dark current is a critical parameter that provides insights into the junction quality and recombination mechanisms. For the InGaAs diode, the forward dark current increases exponentially with the applied voltage and reaches compliance at around 0.6 V. This behaviour is typical of a well-formed diode where the current is primarily governed by thermally generated carriers recombining across the junction.

In contrast, the forward dark current in the GaAsSb diode deviates from the exponential trend after 0.4 V. This deviation suggests the presence of series resistance in the GaAsSb photodiodes. Series resistance can limit the current flow, causing the observed deviation from the ideal exponential increase.

The ideality factors were measured at 1.1 for the 1 μm GaAsSb and 1.4 for the 4.8 μm InGaAs, indicating that recombination in both devices is influenced by diffusion and recombination within the depletion region. While these values suggest that the diodes are close to ideal performance, some non-ideal behaviour is likely caused by recombination-generation processes in the depletion region and at the interface. The difference in ideality factors between the diodes may also point to variations in material quality and interface conditions.

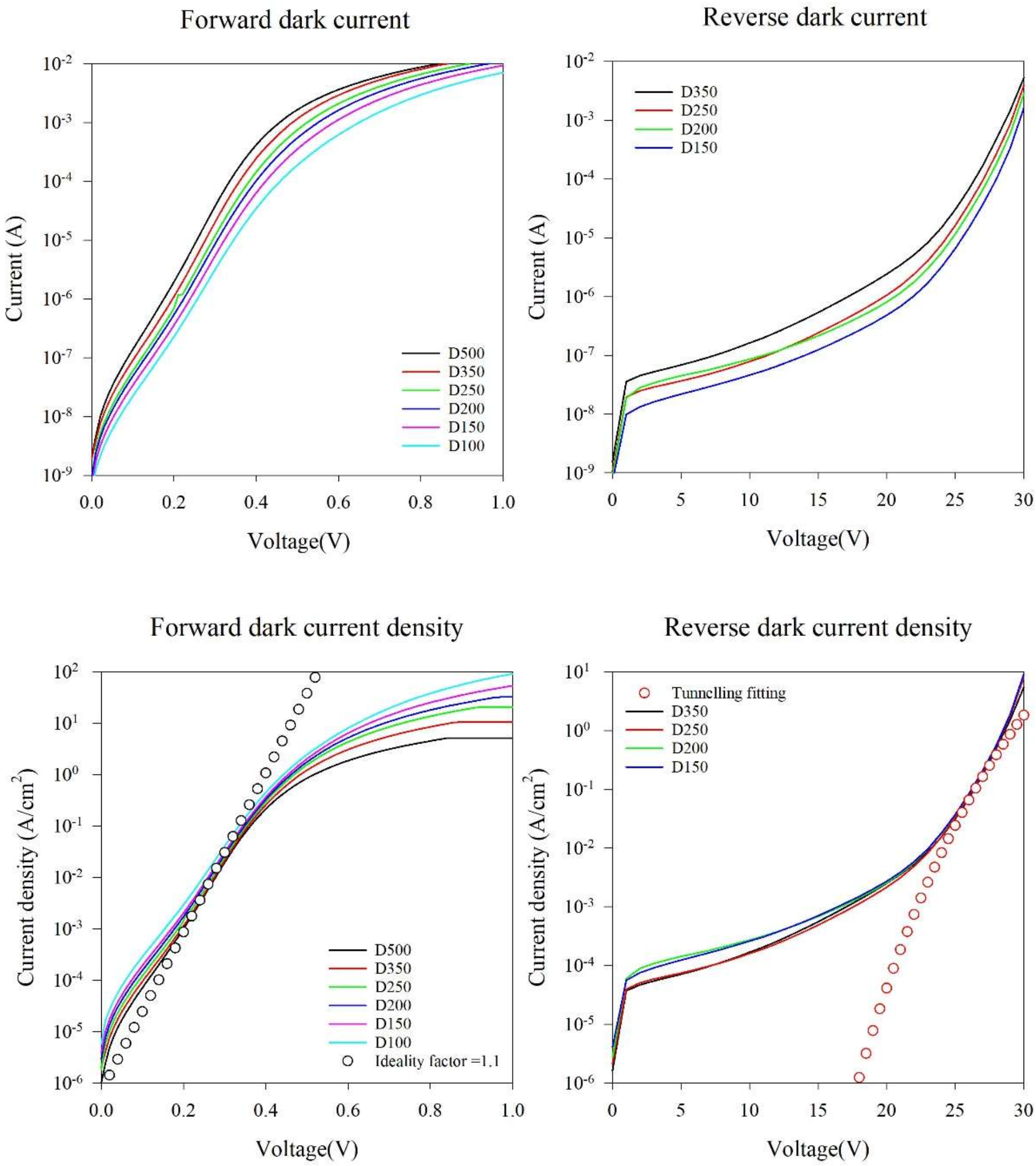

Fig. 4.6 The forward dark current (top left), forward dark current density with ideality factor (bottom left), reverse dark current (top right), and reverse dark current density with tunnelling fitting (bottom right) for 1um GaAsSb photodiodes, the diameters are 500um, 350um, 250um, 200um, and 150um.

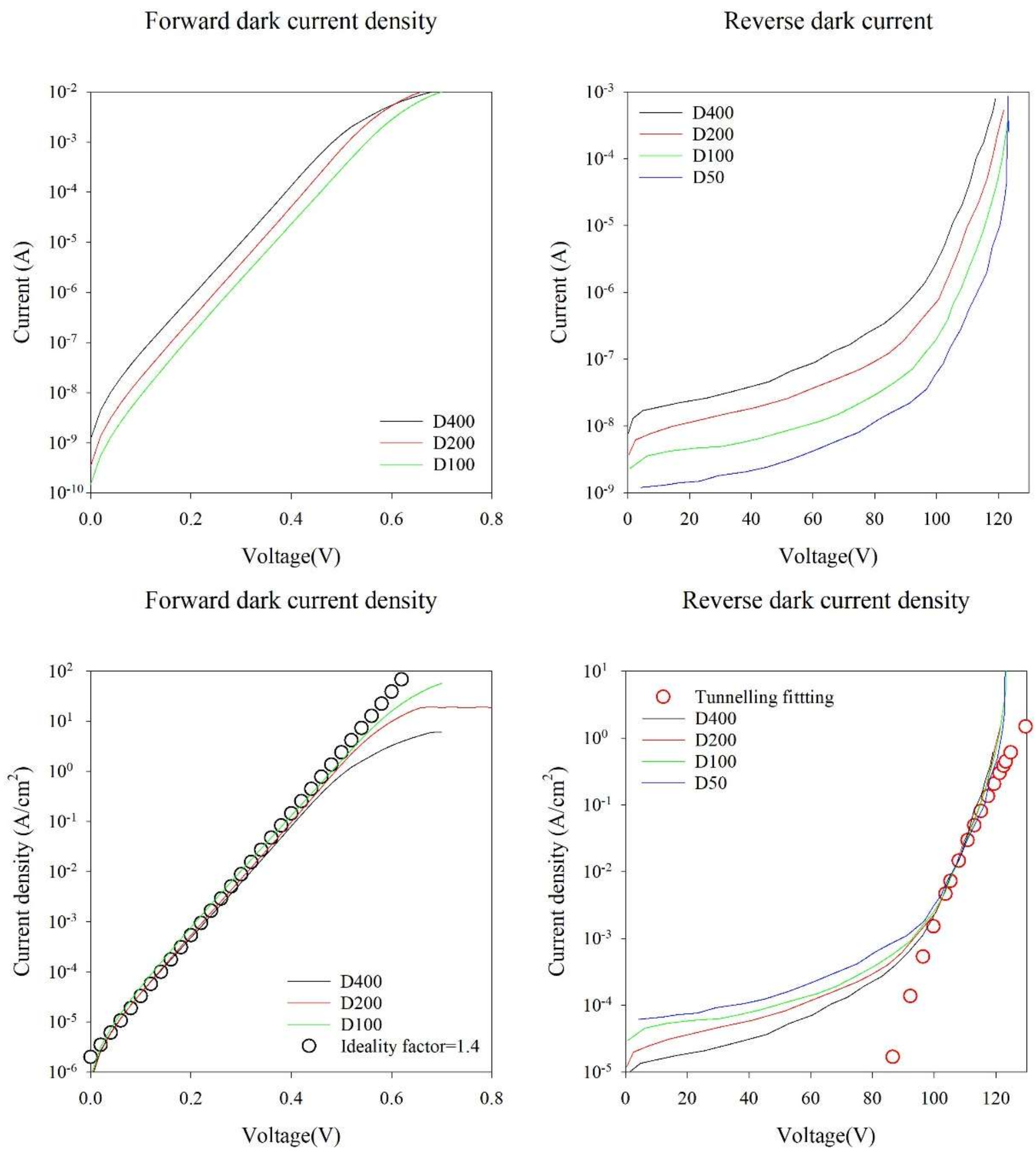

Figure 4.7 The forward dark current (top left), forward dark current density with ideality factor (bottom left), reverse dark current (top right), and reverse dark current density with tunnelling fitting (bottom right) for 4.8um InGaAs photodiodes, the diameters are 500um, 350um, 250um, 200um, and 150um.

The reverse dark currents are measured and shown in Fig. 4.6 and Fig. 4.7, the reverse dark currents increase steadily with the applied reverse voltage after a threshold voltage, this is due to the band-to-band tunnelling in the narrow bandgap semiconductors. Band-to-band tunnelling (BTBT) is a quantum mechanical process where particles tunnels from the conduction band minimum (CBM) to the valence band maximum (VBM) or vice versa through a barrier, which is formed because of the bending of the band edges in the *p-i-n* junction region. The band-to-band tunnelling current becomes pronounced at high electric field, especially for narrow bandgap materials like InGaAs and GaAsSb.

The electric field (E) was deduced from the applied voltage across the width of the intrinsic (i) region, based on the assumption of a uniform electric field distribution in the undoped intrinsic layer (UID). This assumption is supported by the relatively low background doping in the UID layer as discussed above. The band-to-band tunnelling current in a reverse-biased direct bandgap semiconductor is given theoretically by[89]:

$$I_{tun}(V) = \left(\frac{(2m_e)^{\frac{1}{2}} q^3 EVA}{h^2 E_g^{\frac{1}{2}}}\right) \exp\left(-\frac{2\pi\sigma_{tun} m_e^{\frac{1}{2}} E_g^{\frac{3}{2}}}{qhE}\right) \tag{4.7}$$

where E is the electric field, V is the applied voltage across the junction, A is the junction area, q is the electron charge, h is the Planck's constant, E_g is the bandgap, m_e is the carrier effective mass, and σ_{tun} is a constant on the order of unity depending on the shape of the tunnelling barrier.

The parameters of the fitted tunnelling current are shown in Table. 4.3, the calculated curve of the tunnelling current fitting is shown in Fig. 4.8. The band-to-band tunnelling currents observed in InGaAs and GaAsSb materials display remarkable similarities, as the two materials have very similar bandgap and electron mass. The onset of the tunnelling current is around 170kV/cm for both materials. At electric fields exceeding 220 kV/cm for InGaAs and 250 kV/cm for GaAsSb, band-to-band tunnelling becomes the predominant mechanism influencing the measured dark currents. The elevated dark current observed in GaAsSb prior to tunnelling is attributed to side leakage, indicating a fabrication issue rather than an intrinsic material property. This is supported by the fact that dark current in GaAsSb scales with the perimeter before engaging in band-to-band tunnelling, suggesting its association with edge-related leakage currents, as opposed to area-dependent mechanisms seen in InGaAs.

According to Forrest et al. [89], the tunnelling parameter σ_{tun} varies for different barrier shapes, being 1.11 for triangular barriers and 1.88 for parabolic barriers. This suggests that the nature of the barrier significantly impacts the tunnelling process. The possibility of tunnelling through mid-bandgap traps can also affect the prefactor and the height of the tunnelling current, indicating that defect states within the bandgap play a role in the tunnelling mechanism.

The spread in σ_{tun} is expected due to different bandgap lineups, influenced by the choice of cladding materials. These variations affect the junction properties and the effective tunneling barrier at the interfaces of different layers.

Table 4.3 Summary of values of parameters used in the tunnelling current fitting.

Parameters	InGaAs	GaAaSb
Bandgap (eV)	0.745	0.745
Relative carrier effective mass	0.041 [90], [91]	0.0447 [91]
Tunnelling parameter (σ_{tun})	1.36	1.15

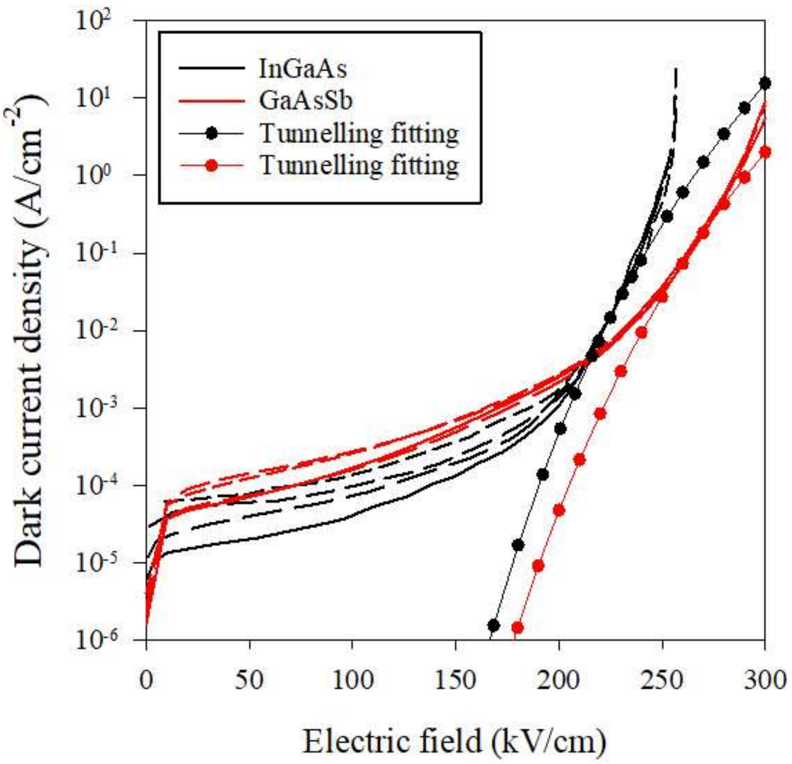

Figure 4.8 Reverse dark current versus electric field, where the black solid line represents the 4.8 µm InGaAs and the red solid line denotes the 1µm GaAsSb. Dashed lines are the fits to the band-to-band tunnelling equation with a bandgap of 0.745 eV and tunnelling.

4.3.3 Photocurrent spectrum characteristics

For an accurate determination of the absorption coefficient, the wavelength dependence of the photocurrent in the devices was measured using photocurrent measurement setup described in Chapter 3. The external quantum efficiencies at 0 V for wavelength from 1400nm in the two InGaAs and two GaAsSb were shown in Fig. 4.10. The shape of the spectral response is confirmed by comparing the measured photocurrent spectrum with the commercially available InGaAs photodiodes with the spectral response provided by Thorlab[92]. The exact external quantum efficiencies confirm using a 1450nm LED focused to a ~50um spot size on the device optical window.

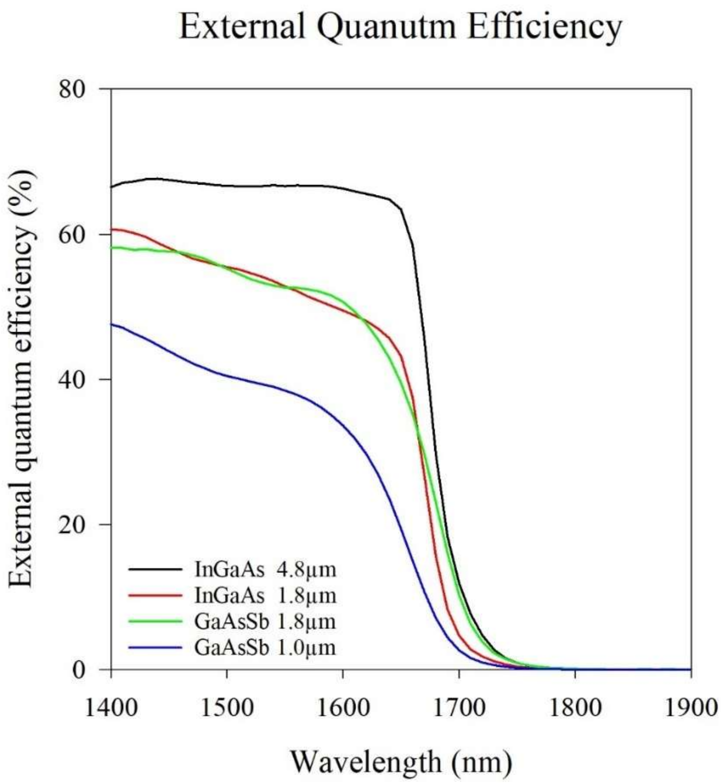

Fig. 4.10 The zero field absorption spectrum of the two InGaAs diodes and GaAsSb didoes.

For all the structures, the cladding layers materials have a much larger bandgap (InAlAs and InP), so they can be considered transparent for wavelengths beyond 1μm. Any light absorbed in the very thin (20 nm) doped contact layers is assumed to only slightly reduce the calculated quantum efficiency by ~1% and is ignored. Therefore, the external quantum efficiency (EQE) generated from the intrinsic region is given by

$$EQE\ (\lambda) = (1 - R)e^{-\gamma(\lambda)t_p}[1 - e^{-\gamma(\lambda)t_i}] \tag{4.8}$$

where R is the reflection loss of the top surface, $\gamma(\lambda)$ is the wavelength dependent absorption coefficient, t_p is the width of the top contact layer (~20 nm), t_i is the width of intrinsic layer. The reflection at the air-semiconductor interface is calculated using the reflectivity data obtained by F. R. Bacher [83] while the reflectivity between the i-region and the cladding layers is neglected due to their similar refractive indices, the refractive indices of the related materials on shown in Fig. 4.11. The calculated reflectivity between InP/InGaAs and InAlAs/GaAsSb interface is < 0.4%.

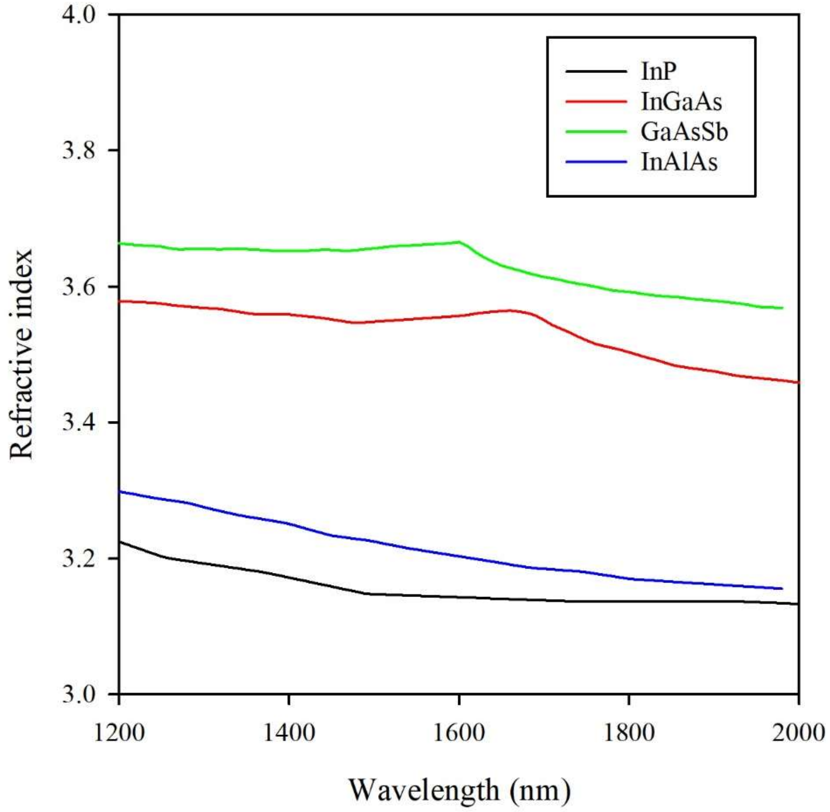

Fig. 4.11 Refractive indices of InGaAs[83]*, GaAsSb*[93]*, InP*[83]*, InAlAs*[94].

4.4 Absorption coefficient in GaAsSb

The extracted 0 V absorption coefficients for InGaAs and GaAsSb from 1400nm are shown in Fig. 4.12. These coefficients are almost identical (within experimental errors) for diodes with different intrinsic (*i*-region) widths. Uncertainties in our measurements are small due to the phase sensitive techniques enabling small values of photocurrent to be measured accurately. Systematic errors arising from small uncertainties in absorption layer thickness (±0.05 μm from CV measurements) lead to an error of ±1% in extracted absorption coefficients. The results also agree well with the published absorption coefficients for InGaAs [83], [84], [86], and GaAsSb [38], but are shown here with absorption determined down to 1 cm^{-1} and extend to longer wavelength range. The absorption coefficients for GaAsSb and InGaAs are 8400 cm^{-1} and 8100 cm^{-1} at 1550 nm respectively. Fig 4.12 shows that at zero bias, the absorption coefficient decreases almost exponentially with increasing wavelengths beyond the bandgap, and the rate of decrease is similar in both materials and for different thicknesses.

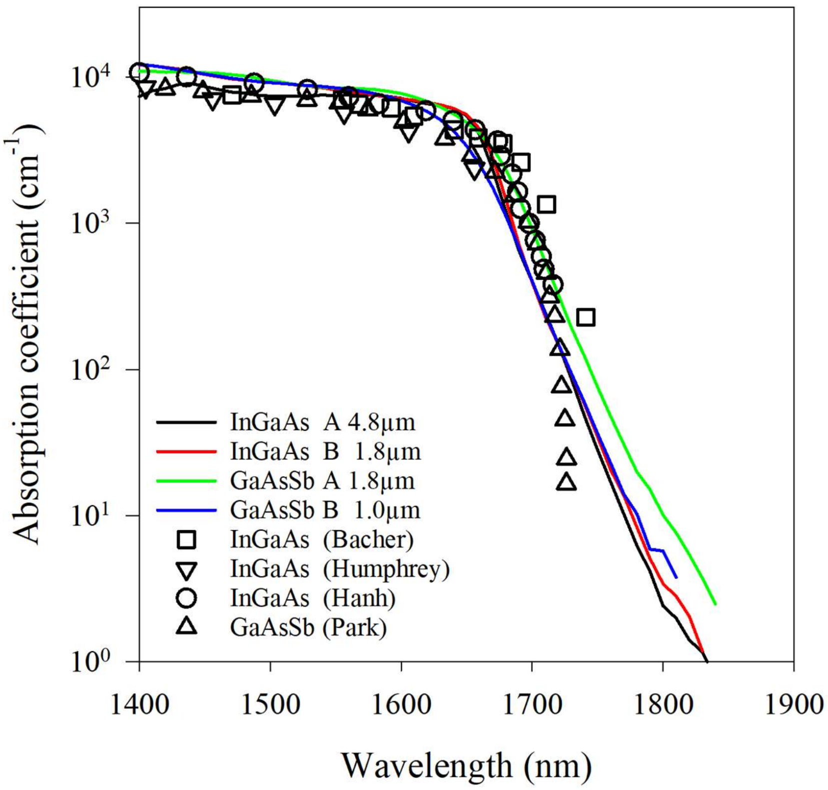

Figure 4.12 The extracted absorption coefficient of the two InGaAs photodiodes and two GaAsSb photodiodes, also shown is the data from previous literatures[38], [83], [84], [86].

4.5 Discussion

The broadening of the absorption edge in both GaAsSb and InGaAs can be quantitatively described by Urbach's rule, which relates the absorption tail below the bandgap to the Urbach energy E_u. The Urbach energy can be calculated using the formula[95]:

$$E_u = \left[\frac{d[\ln(\alpha)]}{d(\hbar\omega)}\right]^{-1} \tag{4.9}$$

Where E_u is the Urbach energy, α is the absorption tail below the bandgap, $\hbar\omega$ is the energy of photon.

For the materials investigated, the Urbach energy E_u was found to be 7.68 meV for the 4.8 μm InGaAs sample and 7.92 meV for the 1.8 μm InGaAs sample. These values are consistent with typical Urbach energies observed in similar III-V semiconductor materials, though the values differ slightly based on the intrinsic properties of the samples. The Urbach energies for the GaAsSb devices were slightly higher: 8.53 meV for the 1.8 μm GaAsSb sample and 8.69 meV for the 1.0 μm GaAsSb sample. The larger E_u in GaAsSb may reflect a higher degree of disorder or the presence of more impurities in the material, which results in a broader absorption tail compared to InGaAs.

It's important to note that these Urbach energy values were measured at room temperature (approximately 300 K). The Urbach energy is temperature-dependent, typically increasing with temperature due to enhanced phonon interactions and thermal broadening of energy states[96], [97]. At lower temperatures, the Urbach energy would be expected to decrease, reflecting reduced phonon interactions and a sharper absorption edge[98]. Conversely, at higher temperatures, the Urbach energy would likely increase, indicating a broader absorption tail due to enhanced thermal effects.

This absorption tail is observed at energies just below the bandgap, where the absorption coefficient does not sharply drop to zero but rather exhibits an exponential decay. This phenomenon reflects the influence of several intrinsic and extrinsic factors in the material. In both GaAsSb and InGaAs, this long-wavelength broadening is believed to originate from optically induced electronic transitions, which are assisted by multiple phonon absorptions in crystalline materials[99]. The absorption of multiple phonons enables transitions in the presence of defects and impurities, which contribute to this tailing behaviour. Additionally, internal electric fields caused by impurities or intrinsic defects, such as vacancies, dislocations, and alloy disorder[100], are also responsible for the broadening of the absorption edge. The presence of these defects distorts the periodicity of the crystal lattice, altering the band structure and increasing the probability of sub-bandgap absorption.

For comparison, a study by Hahn et al.[86] reported a larger Urbach energy of 13 meV for *n*-doped InGaAs layers, which highlights the significant impact of doping on the absorption characteristics.

Doping introduces additional charge carriers and creates local electric fields within the material, further enhancing the absorption below the bandgap and leading to a broader absorption tail.

The observed difference in Urbach energies between GaAsSb and InGaAs suggests that alloy composition and material quality influence the optical behaviour of these materials. Although both GaAsSb and InGaAs are ternary alloys, GaAsSb exhibits a greater degree of alloy disorder. This is due to the larger atomic size difference between Ga, As, and Sb atoms compared to the size difference between In, Ga, and As in InGaAs. The increased lattice strain in GaAsSb leads to more pronounced scattering of carriers and phonons, contributing to the broadening of the absorption edge.

4.6 Conclusion

In this chapter, the absorption coefficients of GaAsSb and InGaAs *p-i-n* photodiodes were investigated, with both materials demonstrating strong absorption around the critical 1550 nm telecom wavelength. The results show that GaAsSb and InGaAs have comparable absorption properties, with coefficients of approximately 8400 cm^{-1} and 8100 cm^{-1}, respectively, making them suitable for applications in photodetectors and avalanche photodiodes (APDs). The devices exhibited low background doping and consistent performance across different intrinsic layer thicknesses, ensuring reliable optical behaviour. Overall, this chapter highlights the potential of both GaAsSb and InGaAs for high-performance optoelectronic devices, particularly in telecommunications, and provides a foundation for further optimization of these materials in future applications.

Chapter 5 Impact Ionization in GaAsSb

5.1 Introduction

Avalanche photodiodes (APDs) are widely used in the short-wave infrared (SWIR) range for optical communication and LiDAR[101] applications because of their ability to amplify weak input signals through internal gain, thereby improving the signal-to-noise ratio (SNR). However, the effective utilization of APDs requires careful management of inherent noise components, including dark current and excess noise. Excess noise, which arises from the stochastic nature of the impact ionization process, inevitably increases with gain. However, the rate of increase is slower when there is a significant difference between the hole (β) and electron (α) impact ionization coefficients. Therefore, finding a multiplier material with a favourable k factor ($k = \beta/\alpha$ for electron-initiated multiplication or α/β for hole-initiated multiplication) is crucial for enhancing the performance of an APD[27].

For 1550 nm applications, a common APD design is the Separate Absorption and Multiplication (SACM) structure[102]. This allows for high multiplication in a wide-bandgap material while reducing the electric field in the narrow-bandgap absorber. Commercially available SACM APDs are made with In GaAs absorbers and InP multipliers[103]. However, the relatively high k-factor of InP (0.4–0.5)[104] leads to significant excess noise due to the similar impact ionization coefficients of electrons and holes, which ultimately limits the overall performance of the device.

Recent advancements have introduced alternative low-noise multipliers, such as AlAsSb ($k = 0.005$)[105], $Al_{0.85}Ga_{0.15}AsSb$ ($k = 0.01$)[106], and AlInAsSb ($k = 0.018$)[107], which are lattice-matched to InP substrates and show potential for 1550 nm APDs due to their low excess noise. However, these materials present specific challenges: AlInAsSb exhibits phase separation during growth, and AlAsSb is highly susceptible to oxidation[105], resulting in elevated surface dark currents. AlGaAsSb, with 85% Al content, mitigates oxidation-related issues while maintaining low noise, making it a promising candidate for next-generation APDs[108].

A critical challenge in APD design is minimizing the conduction band offset (Δ_{EC}) between the absorber and multiplier. AlGaAsSb, despite being a low-noise multiplier, has a substantial Δ_{EC} (~0.5 eV) when paired with InGaAs absorbers, which hinders carrier transport and reduces quantum efficiency (QE)[88]. This necessitates a higher operating bias to achieve efficient performance. In contrast, GaAsSb offers significant advantages as an absorber.

As illustrated in Fig. 5.1, GaAsSb paired with $Al_{0.85}Ga_{0.15}AsSb$ results in a much smaller Δ_{EC}, facilitating smoother carrier transport, improved QE, and a reduced operating bias. With strong absorption in the 1400–1660 nm range and a lower conduction band offset, GaAsSb is well-suited for APDs used in optical communication and LiDAR applications.

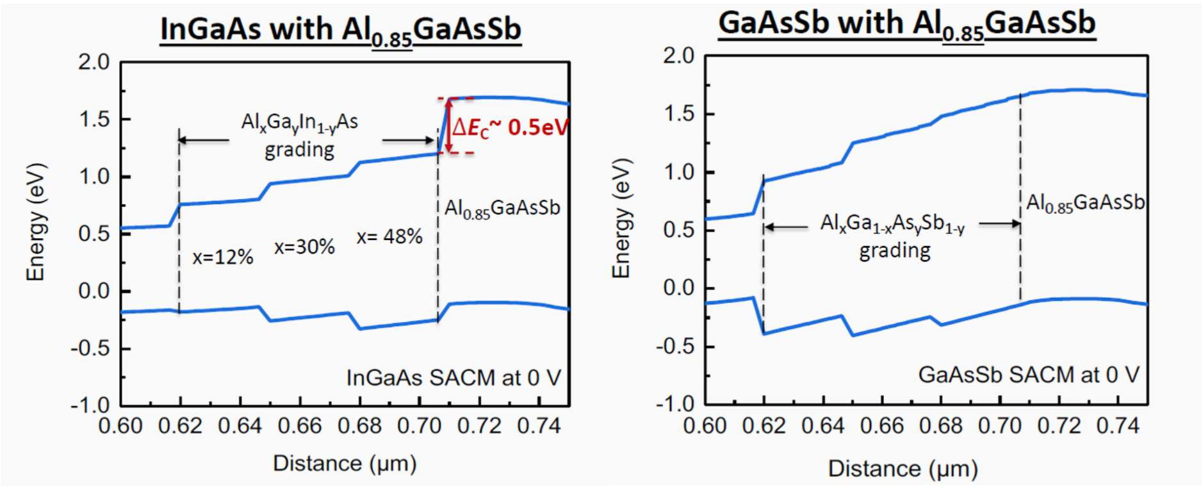

Figure 5.1 The band alignment offset for $Al_{0.85}Ga_{0.15}AsSb$ with InGaAs, and $Al_{0.85}Ga_{0.15}AsSb$ with GaAsSb.

Controlling the electric field in the GaAsSb absorber is critical to prevent unwanted impact ionization and tunnelling, both of which can degrade the performance of SACM APDs[109]. While multiplication is primarily handled by the low-noise $Al_{0.85}Ga_{0.15}AsSb$ layer, any multiplication occurring within the GaAsSb absorber increases noise and reduces the frequency response. To optimize the performance of

GaAsSb/AlGaAsSb SACM structures, it is essential to carefully manage the electric field in the absorber region.

In this chapter, the high-field characteristics of GaAsSb photodiodes are systematically explored. Specifically, multiplication measurements of *p-i-n* GaAsSb photodiodes are used to assess impact ionization. By determining impact ionization characteristics, this study provides key insights that will guide the optimization of GaAsSb-based SACM APDs for improved performance in 1550 nm optical communication and LiDAR applications.

5.2 Experiment Details

The avalanche photodiode (APD) devices used in this study are structured as *p-i-n* APDs with a GaAsSb unintentionally doped (UID) intrinsic region, as detailed in Table 4.1. Two devices, referred to as GaAsSb-A and GaAsSb-B, were grown with variations in the thickness of the GaAsSb UID region and the cladding layers. The *p-i-n* structure consists of highly doped p^{++} and n^{++} contact layers, with the GaAsSb UID intrinsic region serving as the multiplication region where avalanche breakdown and impact ionization processes occur.

To achieve the necessary level of accuracy in device characterization, Capacitance-Voltage (C-V) measurements were employed. This technique is particularly well-suited for determining doping concentrations and intrinsic region thicknesses in semiconductor devices. The C-V measurement technique involves applying a range of reverse bias voltages to the device and measuring the resulting capacitance. As the reverse bias increases, the depletion region widens, causing a decrease in capacitance.

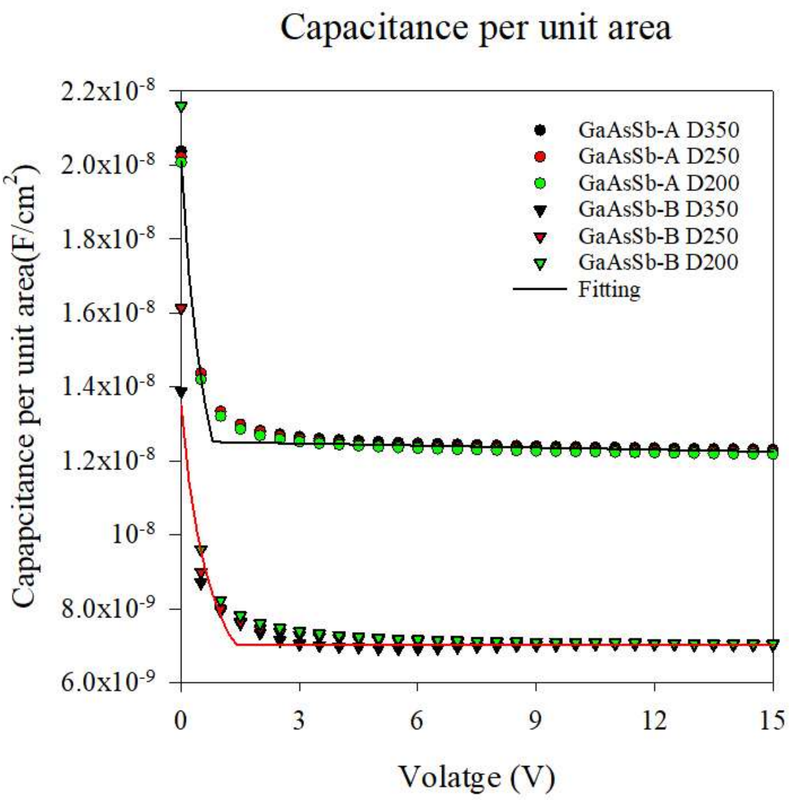

Fig. 5.1 The measured capacitance per unit area for GaAsSb-A and B, with fitted curves.

The C-V measurements revealed several important characteristics of the fabricated devices. By incorporating sample structures and permittivity ($\epsilon_r = 14.3[88]$) into the calculation model (detailed in Chapter 3), the calculated C-V curves were fitted to the measured data, with the closest fit shown as lines in Fig. 5.1. For GaAsSb-A, the measured intrinsic region thickness was 1010 nm, slightly higher than the nominal value of 1000 nm. GaAsSb-B showed a match between the measured and nominal thickness of 1800 nm. This level of accuracy is crucial for understanding device behaviour and validating the fabrication process. The doping density was found to be as low as 1×10^{15} cm^{-3} for GaAsSb-A and 9×10^{14} cm^{-3} for GaAsSb-B. These low doping densities in the UID region are essential for maintaining a relatively uniform electric field across the depletion region, which is crucial for optimal APD performance. Both devices exhibited high doping levels of 1×10^{18} cm^{-3} in the n^+ and p^+ regions, ensuring good ohmic contacts and efficient carrier injection.

Table 5.1 Sample Structure of GaAsSb APD Devices (Nominal vs. Measured Values)

UID region	GaAsSb-A		GaAsSb-B	
	nominal	measured	nominal	measured
UID region doping density (cm^{-3})	-	2×10^{15}	-	9×10^{14}
UID region thickness (nm)	1000	1010	1800	1800
n^+ and p^+ region doping (cm^{-3})	-	1×10^{18}	-	1×10^{18}

5.3 Avalanche Multiplication Measurements

The avalanche multiplication measurements for Devices A and B were conducted to extract the electron (α) and hole (β) impact ionization coefficients. These coefficients are essential for understanding how internal gain and noise evolve in GaAsSb-based APDs under different bias conditions. The multiplication factor M, defined as the ratio of the total photocurrent to the primary photocurrent, quantifies the internal gain within the device, which is driven by the impact ionization process in the high-field regions.

The photomultiplication measurements for the GaAsSb APD devices were conducted using methods as described in Chapter 3. To comprehensively characterize the devices, multiple wavelengths of light (532, 980, and 1300 nm) were employed to illuminate all layers of the structure. A lock-in amplifier was utilized to measure the relative change in photocurrent across various devices with different diameters, ensuring the repeatability of results and confirming that the multiplication measurements were independent of incident power. The multiplication factor M was calculated as:

$$M = \frac{I_{ph}}{I_{pr}} \tag{5.1}$$

$$I_{pr} = kV + b \tag{5.2}$$

where I_{ph} is the total photocurrent measured and I_{pr} is the primary photocurrent corrected for any baseline shifts due to depletion edge movement or responsivity changes. To ensure accuracy, baseline correction was applied to the multiplication measurements, especially at low bias voltages where tunnelling and non-multiplicative effects are significant. A simplified linear correction Eqn. (5.2), which closely aligns with the Woods correction[110], was used for all data to ensure consistent and accurate analysis.

This method corrects for changes in the primary photocurrent as the depletion edge moves further into the cladding layers with increasing reverse bias. The corrected multiplication values account for any non-multiplicative current increase due to the extension of the depletion region.

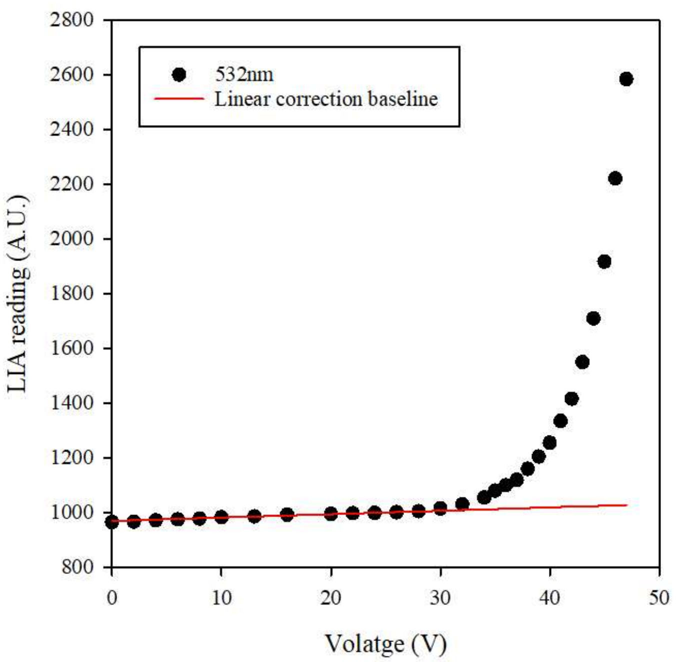

Fig. 5.2 Example of baseline correction for avalanche multiplication.

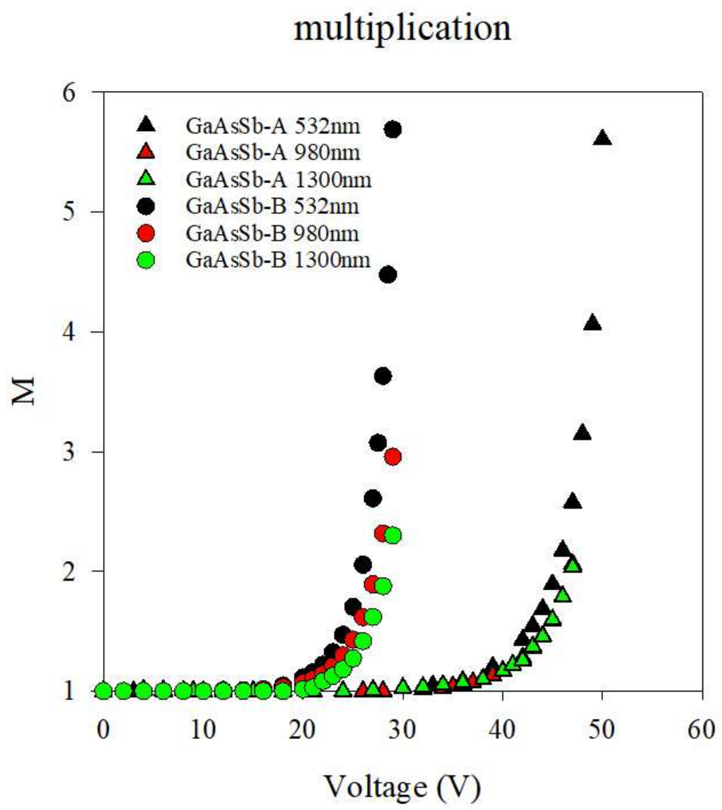

Fig. 5.3 Measured multiplication in GaAsSb-A and B under three different wavelengths, 532, 980, and 1300 nm.

Fig. 5.3 presents the multiplication (M) as a function of reverse bias for Devices A and B under illumination at three distinct wavelengths: 532 nm, 980 nm, and 1300 nm. This comprehensive set of measurements provides crucial insights into the avalanche multiplication process in these GaAsSb photodiodes.

The results clearly demonstrate that shorter wavelengths, particularly 532 nm, lead to higher multiplication values. This phenomenon can be attributed to the injection of carriers in the cladding layers. Due to the large band-offset, any carriers generated in the top InGaAs contact layer do not contribute to the overall photocurrent, effectively isolating the multiplication process to the layers beneath this contact. For the 532 nm illumination, a significant portion of the light is absorbed in the top p+ InAlAs cladding layer. The absorption characteristics of these InAlAs layers are estimated in the as 6×10^4 cm^{-1} (similar to InP). For Device A, with its 150 nm p+-InAlAs cladding layer, the total absorption (including the 20 nm p++ InGaAs layer) is approximately 92.1% of the incident light. For device B, with its thicker 300 nm p+-InAlAs cladding layer, absorbs a total of 96.9% of the incident light. Given the high absorption in both devices, they each exhibit nearly pure electron injection profiles, as the photogenerated electrons drift into the multiplication region while the holes are collected at the p+ contact.

The longer wavelengths of 980 nm and 1300 nm penetrate deeper into the device structure, particularly the GaAsSb layers where the primary absorption and multiplication processes occur. These wavelengths experience minimal absorption in the top InGaAs and InAlAs layers, with the primary absorption occurring within the UID GaAsSb and n--GaAsSb layers. This absorption profile generates electron-hole pairs predominantly in the intrinsic region and the n-type layer of the device, resulting in a mixed carrier injection profile for both Device A and Device B, with photogenerated electrons and holes both contributing to the multiplication process.

The characterization results of GaAsSb-A and B consistently show higher gain values with shorter wavelength illumination. This trend strongly indicates that the electron ionization coefficient (α) is greater than the hole ionization coefficient (β) in GaAsSb.

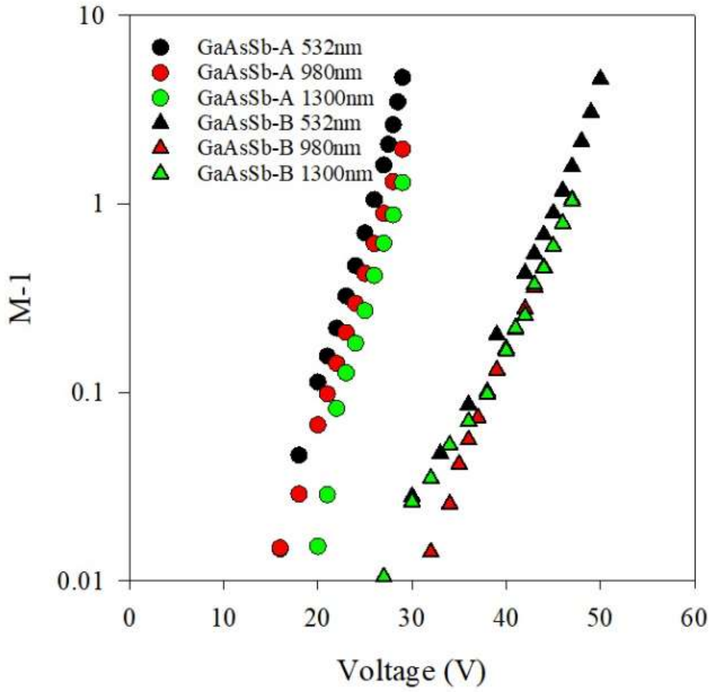

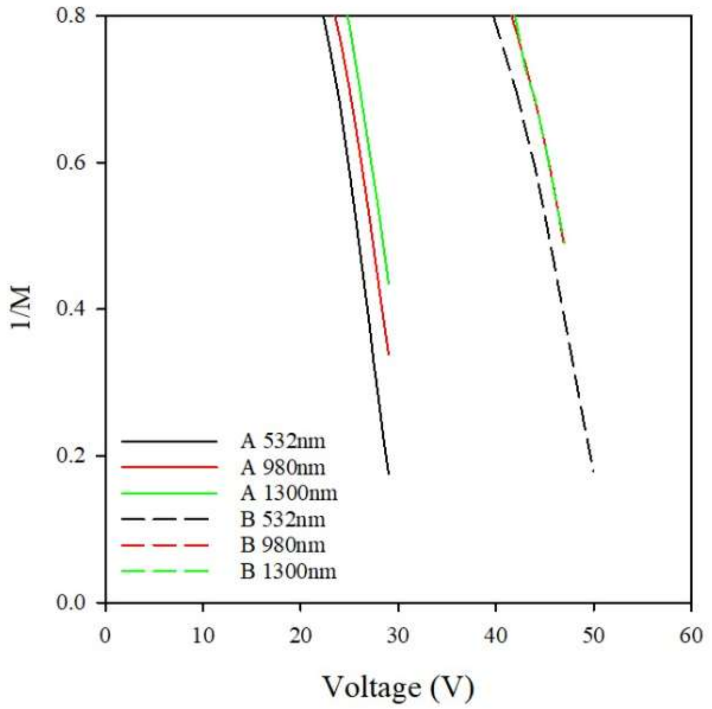

Fig. 5.4 (left)M-1 vs reverse bias and (right) 1/M vs reverse bias for GaAsSb-A and B under three different wavelengths, 532, 980, and 1300 nm.

To identify the onset of impact ionization in GaAsSb, $M-1$ was plotted for Device A and B on a logarithmic scale as a function of reverse bias, as shown in Fig. 5.4 (a). This approach provides a sensitive method for detecting the initial stages of multiplication, as even small increases in M result in noticeable changes on the logarithmic scale.

The avalanche threshold voltage (Vi) is defined arbitrarily as the point where $M - 1 = 0.01$, corresponding to a multiplication factor M = 1.01. For Device A, Vi occurs at 15 V, while for Device B, it occurs at 30 V. Despite the difference in applied voltages, both of these threshold points correspond to a similar electric field (E_{ava}) of approximately 150 kV/cm in the GaAsSb layer.

The $1/M$ plot, in Fig. 5.4 (b), is useful for examining behaviour near avalanche breakdown. As the reverse bias voltage increases and M grows rapidly, $1/M$ approaches zero, signalling breakdown. For the GaAsSb devices, breakdown occurred at 30 V for GaAsSb-A, increasing to 52 V for GaAsSb-B.

5.4 Impact Ionization Coefficient

The impact ionization coefficients of GaAsSb were determined by iteratively fitting multiplication curves measured on Devices A and B using two different lasers (532 nm and 980 nm). This fitting process employed the Random Path Length (RPL) model[111], which uses the known doping concentrations and thicknesses of the device layers, as detailed in Table 5.1. The RPL model effectively simulates the multiplication process across the electric field profile, accurately predicting carrier multiplication for a range of multiplication factors from M=1.01 to M=50. However, this model does not account for carrier history or dead-space effects, assuming that the impact ionization rates depend solely on the local electric field strength within the device[112].

For the mixed injection case (in GaAsSb-A), where both electron and hole ionizations contribute, the absorption coefficients of InAlAs and GaAsSb at 532 nm and 980 nm were included as additional fitting parameters. These coefficients are essential because they determine the carrier generation profiles under different optical injection conditions. By incorporating these parameters, the model can accurately represent the varying absorption characteristics of the materials, ensuring precise fitting of the multiplication data to real device behaviour.

The best fit to the experimental multiplication curves for Devices A and B, shown in Figure 5.5 (a) and (b). The parameterized α and β of GaAsSb for field range from 150 kV/cm $\leq E \leq$ 300 kV/cm are shown in Fig. 5.5 and parameterized by:

$$\alpha(E) = 10 \times 10^7 \exp\left(-\left(\frac{4.76\times10^6}{E}\right)^{0.8}\right) cm^{-1} \tag{5.1}$$

$$\beta(E) = 2 \times 10^7 \exp\left(-\left(\frac{4.76\times10^6}{E}\right)^{0.8}\right) cm^{-1} \tag{5.2}$$

The k of GaAsSb is found to vary between 0.03 – 0.05 over the electric field range studied, where k represents the ratio of hole to electron ionization rates (β/α). This value is consistent with the behaviour observed in InGaAs, where hole and electron ionizations are relatively balanced. However, this k is an order of magnitude higher than that observed in AlGaAsSb[113] (where $k \approx 0.01$), indicating that GaAsSb has a much stronger hole ionization process compared to materials like AlGaAsSb.

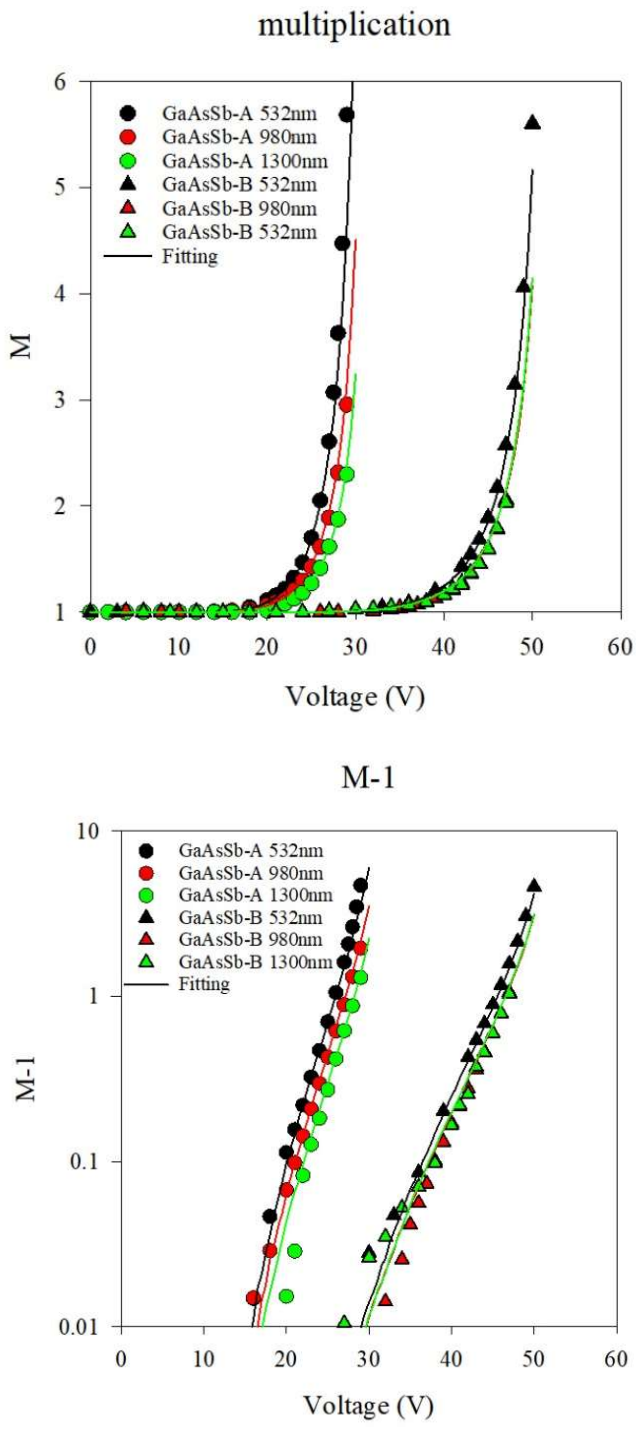

Fig. 5.5 Measured and fitted multiplication (M) and inverse multiplication (M−1) curves for GaAsSb-A and GaAsSb-B at three different wavelengths (532 nm, 980 nm, and 1300 nm). The solid lines represent the fitting to the experimental data.

5.5 Discussion

When comparing the impact ionization coefficients α (electron ionization) and β (hole ionization) between GaAsSb and InGaAs[114], notable differences arise in both their values and behavior under varying electric fields. Figure 5.6 illustrates the impact ionization coefficients (α and β) of GaAsSb and InGaAs as a function of the inverse electric field. It shows the differences in the ionization behaviours between the two materials, with GaAsSb demonstrating lower β and a varying α at different fields.

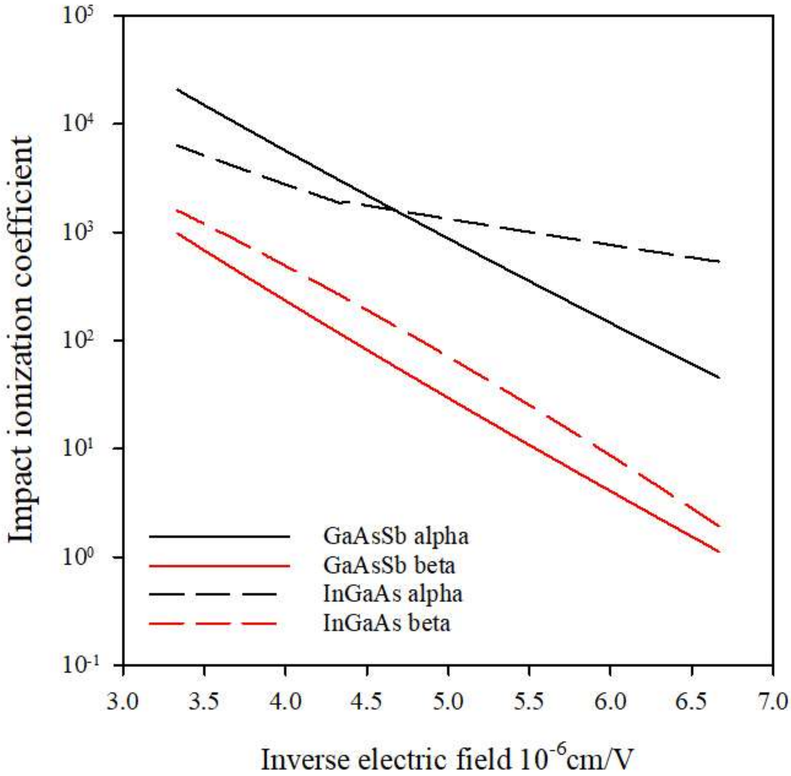

Figure 5.6 Impact ionization coefficients (α and β) of GaAsSb and InGaAs[114] *as a function of the inverse electric field.*

In the 165–210 kV/cm (for inverse electric field $> 4.7 \times 10^{-6}$ cm/V) electric field range, InGaAs exhibits a higher electron ionization coefficient α than GaAsSb, and its α decreases only slowly with decreasing electric field. This behaviour is attributed to the large Γ-L and Γ-X inter-valley separations in InGaAs (~0.785 eV and 1.082 eV, respectively)[115]. These large energy separations prevent electrons from readily accessing higher-energy satellite valleys at lower fields, thus slowing down the decrease in α. As a result, InGaAs maintains higher electron ionization rates at moderate electric fields, contributing to its higher multiplication at lower fields. However, at electric fields above 220 kV/cm, InGaAs shows a much stronger field dependence for α, as a larger number of final states in the satellite valleys become available for ionization. This transition is characterized by a steeper increase in α, as the higher energy states in these satellite valleys become accessible to electrons.

In contrast, GaAsSb has much smaller Γ-L (0.121 eV) and Γ-X (0.232 eV) inter-valley separations[116], meaning that electrons can more easily transition into satellite valleys even at relatively low electric fields. This results in a more pronounced electron ionization behaviour in GaAsSb at fields above 210 kV/cm, where it can exhibit a larger α than InGaAs. However, this is more than the typical electric field that the absorption region operates on.

The hole ionization coefficient β, however, remains lower in GaAsSb than in InGaAs across the entire field range. This difference can be attributed to the larger ΔS_o (split-off energy) in GaAsSb (~0.391 eV), compared to 0.345 eV in InGaAs[116]. This larger split-off energy makes it harder for holes in GaAsSb to gain the necessary energy to ionize, resulting in a significantly smaller β value. The reduced hole ionization, not only leading to lower multiplication gain in GaAsSb, also reduces noise from hole-initiated ionization processes, which can be advantageous in low-noise applications.

Table. 5.2 The spin splitting energy, energy differences between the bottom of the conduction band valley and the bottom of satellite valleys.[116]

	InGaAs	GaAsSb
Γ-L (eV)	0.785	0.121
Γ-X (eV)	1.082	0.232
ΔS_o (eV)	0.34	0.391

Fig. 5.7 shows the product of $\alpha \times w$, where w is the thickness of a 1 μm absorber, for both InGaAs and GaAsSb as a function of the electric field. This figure highlights how electron multiplication arises from an electron traveling through a 1 μm thick absorber in each material, alongside the tunnelling dark current density. The electron multiplication in GaAsSb is lower at electric fields below 210 kV/cm, with a multiplication factor of 1.038 at 175 kV/cm compared to 1.138 for InGaAs. The results indicate that GaAsSb has significantly lower multiplication compared to InGaAs at electric fields below 210 kV/cm, which correlates with its lower electron ionization coefficient α in this region. This behaviour is particularly advantageous for reducing noise and limiting tunnelling currents, making GaAsSb more suitable for applications requiring low noise and high signal clarity at moderate fields.

At low electric fields, tunnelling current rather than impact ionization tends to dominate APD performance. The calculated tunnelling current is shown as lines in Fig. 5.7, for both GaAsSb and InGaAs, maintaining the electric field below 175 kV/cm in the absorber region is necessary to keep tunnelling dark currents below 1×10^{-6} A/cm2. However, GaAsSb has lower α compared to InGaAs at these fields means that it generates less impact ionization, which translates into reduced gain but also lower noise. This makes GaAsSb more suitable for applications requiring low noise and high signal clarity at moderate fields.

At higher fields, both GaAsSb and InGaAs experience increasing tunnelling currents, but GaAsSb is capable of withstanding higher electric fields before impact ionization becomes problematic. This robustness against early ionization, and reduced band offset when grown with AlGaAsSb, makes GaAsSb a strong candidate for SACM APDs designed to operate in high-field environments, such as long-range LiDAR or high-bandwidth optical communication systems.

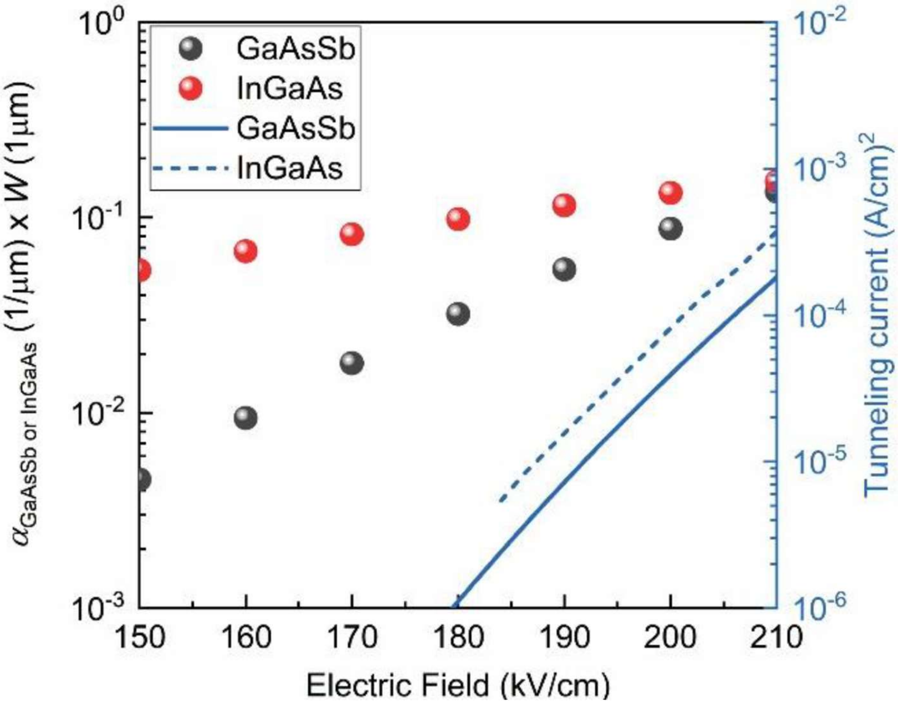

Fig. 5.7 A comparison of the multiplication arising in a 1μm thick absorber of GaAsSb and InGaAs as a function of the electric field. Also shown is the tunnelling dark current density for these two materials as a function of the electric field.

5.6 Conclusion

This chapter has explored the impact ionization properties of GaAsSb in comparison to InGaAs, highlighting their respective strengths and weaknesses for SACM APD applications. Key findings include:

GaAsSb exhibits a lower electron ionization coefficient (α) than InGaAs at electric fields below 210 kV/cm. While this results in reduced multiplication, it also significantly reduces noise, making GaAsSb ideal for low-noise applications where maintaining signal clarity is critical.

At electric fields above 210 kV/cm, GaAsSb has smaller inter-valley separations enable higher electron ionization rates, allowing it to achieve competitive multiplication without the need for excessively high fields. This makes GaAsSb well-suited for applications requiring high-field operation and moderate to high gain, such as long-range optical communication and LiDAR.

The consistently lower hole ionization coefficient (β) in GaAsSb, due to its larger split-off energy, helps reduce noise from hole-initiated ionization. This behaviour is beneficial for designing APDs that require low-noise operation in environments with high signal sensitivity.

In both GaAsSb and InGaAs-based devices, managing tunnelling currents is crucial to maintaining low dark current levels. By keeping the electric field in the absorber region below 175 kV/cm, both materials can limit tunnelling dark currents to acceptable levels, although GaAsSb showed lower multiplication at these fields, translates to lower noise overall.

In conclusion, GaAsSb presents a compelling alternative to InGaAs for SACM APD designs, offering lower noise at moderate fields and strong multiplication performance at higher fields. These characteristics provide a clear pathway for optimizing GaAsSb-based APDs in telecommunication and LiDAR applications, where balancing noise, gain, and field management is critical for device performance.

Chapter 6 The Electroabsorption in GaAsSb and InGaAs

6.1 Introduction

The manipulation of absorption properties in a semiconductor through the application of electric fields, known as electroabsorption, is a critical phenomenon in the realm of optoelectronics. The electroabsorption effect, described independently by Franz[50] and Keldysh[51], introduces an electric-field-dependent absorption tail in bulk semiconductors. This phenomenon occurs through photon-assisted tunnelling of electrons from the valence to conduction bands. One of the primary applications of the electroabsorption effect is in electroabsorption modulators (EAMs). By applying an electric field to modulate the absorption of light in semiconductors, EAMs can achieve high-speed optical intensity modulation[117]. Researchers have investigated various III-V semiconductor materials as potential candidates for EAMs, such as GaAs[118], InGaAsP[54], and GeSn[119], studying their potential to provide efficient modulation at different wavelengths relevant for optical communications.

Beyond modulation, the electroabsorption effect enables photodetectors to operate at wavelengths slightly longer than the semiconductor's bandgap, expanding the spectral range for photodetection [120]. The effect has also proven useful for extracting information about semiconductor properties, including band structure, built-in electric fields, strain, and temperature dependence of the bandgap. Time-resolved electroabsorption measurements can even reveal ultrafast electric field dynamics in semiconductors with sub-picosecond resolution[121].

In the context of telecommunications, two materials have garnered significant attention: $GaAs_{0.5}Sb_{0.5}$ (InGaAs) and $In_{0.53}Ga_{0.47}As$ (GaAsSb). Both possess direct bandgaps of approximately 0.75 eV and can be grown lattice-matched to InP, making them ideal candidates for absorber materials in 1550 nm applications. The growing demand for increased network bandwidth and capacity has driven the expansion of operational wavelengths in optical fibres from the C-band (1530 nm ~ 1565 nm) to the L-band (1565 nm ~ 1625 nm). These wavelengths lie close to the band edges of InGaAs and GaAsSb, where absorption coefficients can be significantly influenced by external electric fields.

Despite extensive research on the zero-field absorption properties of InGaAs and GaAsSb, there has been a notable lack of investigation into their electroabsorption effects. This gap in knowledge is critical, as the sensitivity to electric fields is a crucial consideration when employing these materials in various optoelectronic devices, including photodiodes, avalanche photodiodes (APDs), optical modulators, and switches.

This chapter aims to address this critical knowledge gap by providing a comprehensive study of the electroabsorption effects in InGaAs and GaAsSb. By utilizing thick epitaxially grown absorption layers of these materials in a *p+-i-n+* configuration, we investigate the changes in absorption just above and below the band edge for electric fields up to 200 kV/cm. Through the measurement of wavelength-dependent photocurrents, we experimentally determine the electroabsorption coefficient for wavelengths extending up to 2200 nm. This research will not only advance our understanding of these specific materials but also contribute to the broader field of optoelectronics and semiconductor physics.

6.2 Experiment details

For the electroabsorption coefficient measurements in this chapter, only the GaAsSb-A (1.0 μm) and InGaAs-B (4.8 μm) *p-i-n* photodiodes were studied. These devices were chosen because they can withstand higher reverse bias voltages, enabling the application of electric fields exceeding 200 kV/cm. Detailed structural information for these photodiodes is provided in Chapter 4, where their zero-field absorption coefficients were also analysed. Both devices were grown using Metalorganic Vapour-Phase Epitaxy (MOVPE) for InGaAs and Molecular Beam Epitaxy (MBE) for GaAsSb, with highly doped *p+* and *n+* cladding layers to facilitate efficient carrier collection. InP was used as the cladding material for the InGaAs device, and InAlAs was used for GaAsSb, ensuring that no absorption occurs in the cladding regions within the wavelength range of interest.

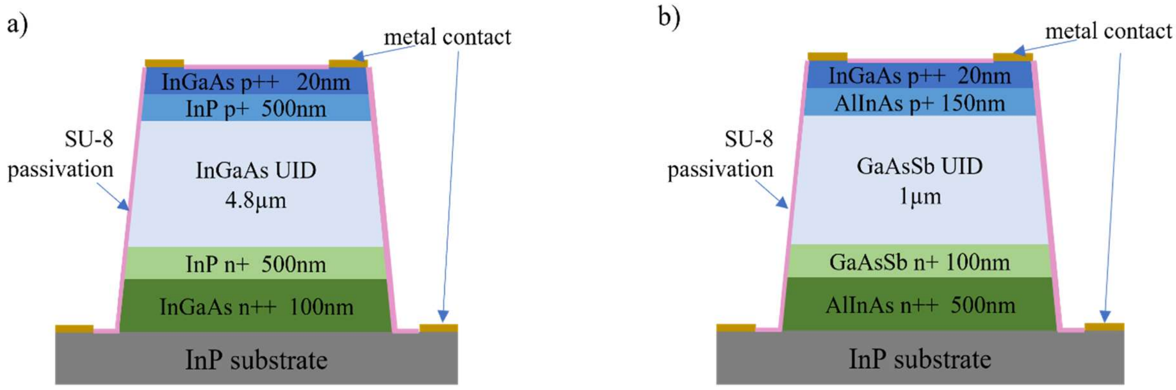

Fig. 6.1 Cross-sectional schematics of (a) InGaAs and (b) GaAsSb heterojunction photodiodes.

To investigate the electric-field-dependent absorption behaviour, voltage-dependent photocurrent measurements were conducted. The photodiodes were subjected to varying reverse bias voltages to generate a uniform electric field across the intrinsic region. Reverse bias voltages up to 120 V were applied to the InGaAs-B device and up to 24 V to the GaAsSb-A device, allowing the electric fields to exceed 200 kV/cm in both cases.

A broadband light source was used, and the light was directed through a monochromator to select wavelengths ranging from 1200 nm to 2200 nm. The photocurrent response was recorded using a lock-in amplifier to ensure high sensitivity across all voltages and wavelengths. The external quantum efficiency (EQE) spectra were first measured at zero bias to establish a baseline for the inherent absorption properties. The measurements were then repeated at incrementally higher bias voltages, observing the Franz-Keldysh effect, which results in a redshift and broadening of the absorption edge under increasing electric fields.

The EQE spectra for InGaAs-B (4.8 μm) and GaAsSb-A (1 μm), presented in the fig. 6.2, show this behaviour clearly. In the InGaAs-B device, the EQE at zero bias (black curve) reveals the inherent absorption characteristics, with an absorption edge around 1600 nm. As the reverse bias voltage increases, the absorption edge shifts toward longer wavelengths, consistent with the electroabsorption effect. Beyond 40 V, the entire EQE curve starts to increase significantly, particularly at longer wavelengths, reaching up to 120 V. The increasing electric field causes a pronounced enhancement in EQE, indicating stronger photon-assisted tunnelling and a widening of the absorption edge.

In the GaAsSb-A device, similar behaviour is observed, though at lower voltages. The EQE measured at 0 V (black curve) shows an absorption edge near 1550 nm. As the reverse bias voltage increases from 3 V to 24 V, the EQE shows a gradual broadening of the absorption edge, but the increase in EQE is more modest compared to InGaAs. Nonetheless, the electroabsorption effect is evident, particularly beyond 12 V, where the redshift becomes more pronounced, and the EQE at longer wavelengths increases slightly.

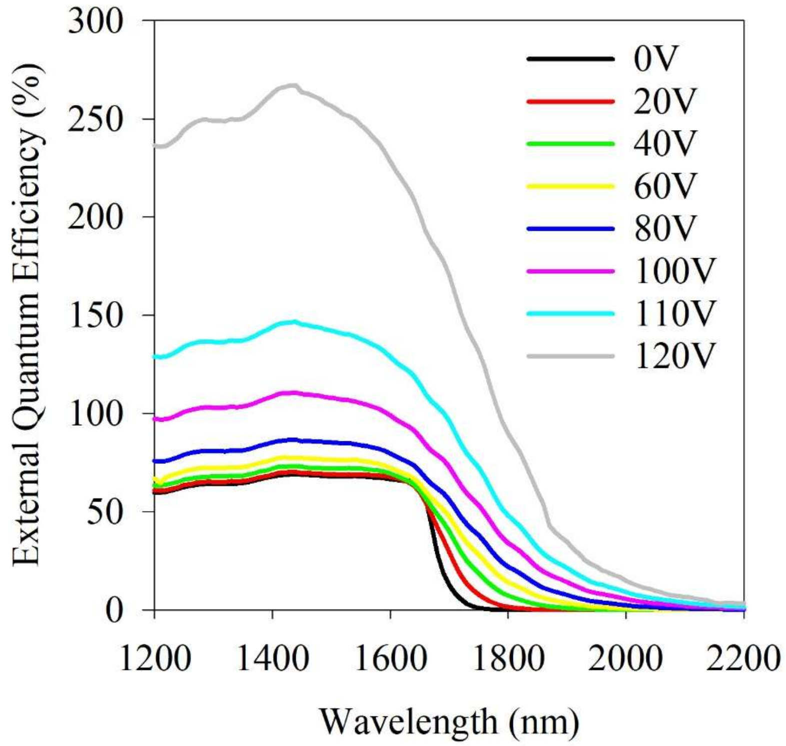

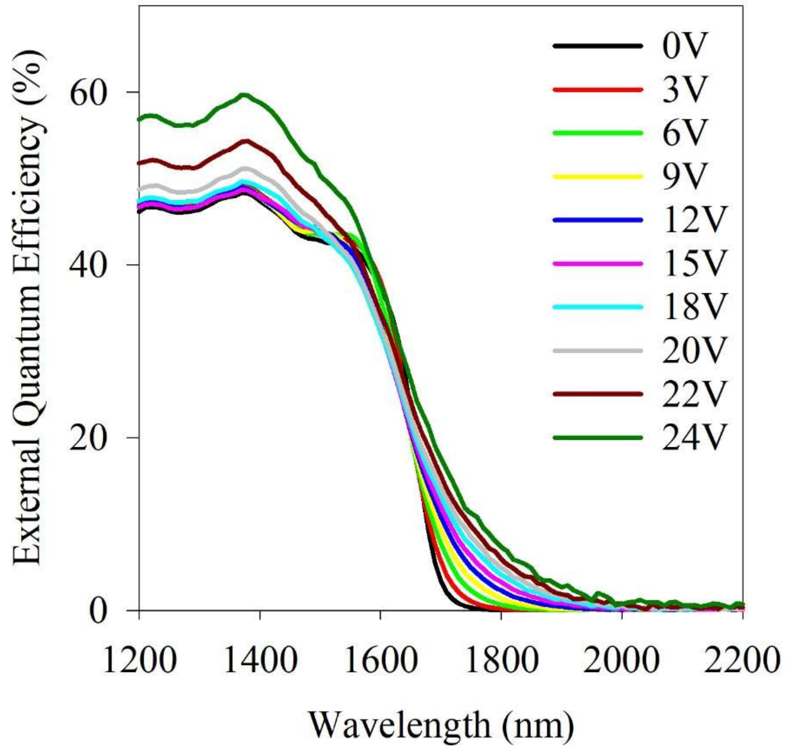

Fig. 6.2 The external quantum efficiency of the (top) 4.8um InGaAs and (down) 1um GaAsSb at various reverse bias.

6.3.1 Field dependent absorption coefficient

An important factor in interpreting the EQE data is the influence of avalanche multiplication, particularly in the InGaAs-B device. While GaAsSb-A exhibits lower multiplication due to its shorter intrinsic region, InGaAs-B is more prone to avalanche effects under moderate electric fields. This is not only because InGaAs has a slightly higher low-field impact ionization coefficient compared to GaAsSb (as discussed in Chapter 5), but also because the longer intrinsic region in the InGaAs-B device allows carriers to travel a greater distance before being collected. The increased travel distance gives carriers more opportunities to undergo impact ionization, resulting in a higher multiplication gain. This effect amplifies the photocurrent and distorts the measured EQE beyond the changes caused solely by electroabsorption. To account for this, a correction factor, M_{mix}, was applied to remove the effects of avalanche multiplication and isolate the electroabsorption-induced changes in the photocurrent.

The EQE spectra presented in Fig. 6.3(a)(c) show the corrected data after removing multiplication effects using M_{mix}. In the logarithmic plot, the absorption tail becomes clearly visible, and a softening of the slope with increasing reverse bias can be observed. As the reverse bias voltage increases, the absorption edge shifts toward longer wavelengths, with a noticeable increase in absorption beyond 1660 nm and a slight decrease in absorption below 1660 nm.

The electric field dependent absorption coefficients which are deduced from the unmultiplied EQE spectra are shown by the symbols in Fig. 6.3 (b)(d). For both InGaAs and GaAsSb the absorption coefficients increase with electric field at wavelengths beyond 1660 nm in InGaAs and 1650 nm in GaAsSb, leading to a softening of the roll-off slopes, and a red-shift of the cut-off edge. The energy where these electroabsorption curves intersect each other (i.e. are almost independent of electric field) is sometimes referred to as the "neutral point" [122] and this gives values for InGaAs (0.747 eV) and GaAsSb (0.751 eV) that are in close agreement with literature values for E_g. At the highest electric fields investigated of 200 kV/cm, the absorption coefficients at 2000 nm have increased from effectively zero to 96 cm^{-1} for InGaAs and 66 cm^{-1} for GaAsSb, indicating their potential for high contrast waveguide modulation at this wavelength.

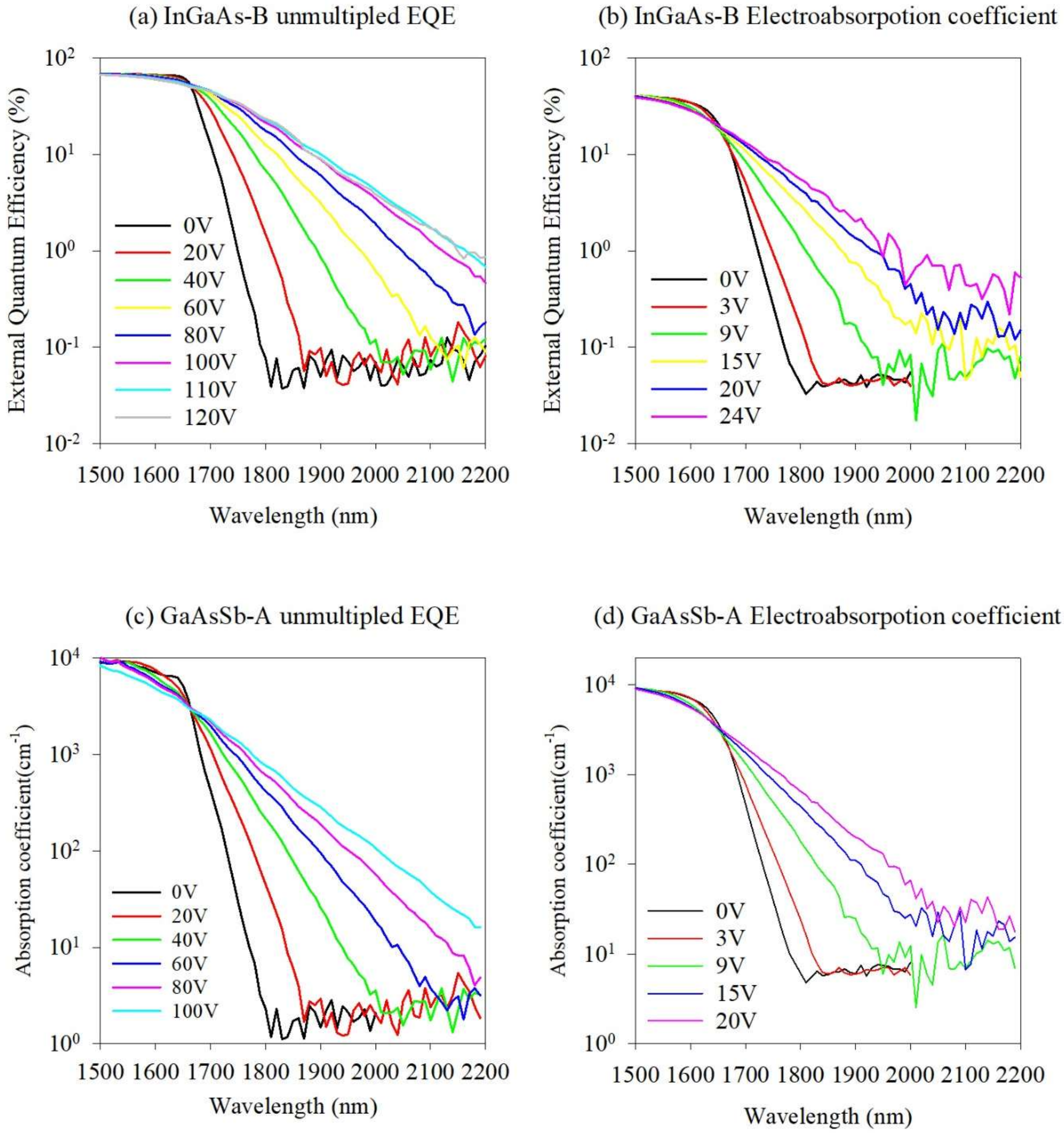

Fig. 6.3 The unmultiplied external quantum efficiency for the (a) 4.8um InGaAs and (b) 1um GaAsSb at various reverse bias. The extracted and calculated absorption coefficients under various reverse bias for (c)InGaAs and (d)GaAsSb photodiodes.

6.3.2 Error Analysis of the $\boldsymbol{M_{mix}}$ Approximation

In this section, we examine the accuracy of the approximation used for the multiplication correction factor M_{mix} and its potential sources of error. The approximation assumes that multiplication is relatively uniform across all wavelengths, significantly simplifying the correction process in the external quantum efficiency (EQE) measurements. This assumption holds well at longer wavelengths, where the absorption coefficient is small, resulting in minimal multiplication effects. However, at shorter wavelengths, the absorption coefficient increases, leading to a corresponding rise in M_{mix}, which is not accounted for in the constant correction method. This introduces slight inaccuracies, particularly at shorter wavelengths where the absorption coefficient, and thus the multiplication factor, varies more significantly.

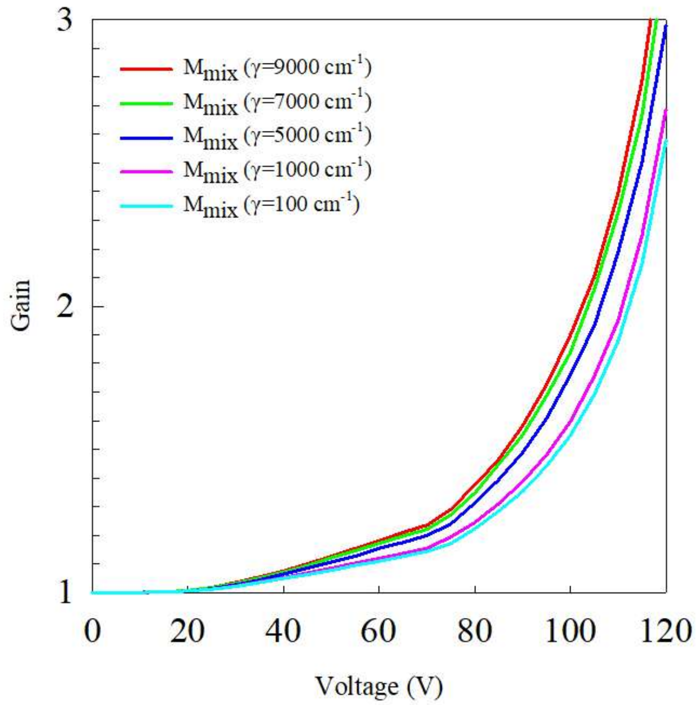

Fig. 6.4 Voltage-dependent gain curves for different absorption coefficients (γ). The multiplication decreases as γ lowers from 9000 cm^{-1} to 100 cm^{-1}, resulting in slower gain increases at lower γ values.

Fig. 6.4 illustrates the relationship between multiplication and applied voltage for different values of the absorption coefficient γ. As γ decreases from 9000 cm^{-1} to 100 cm^{-1}, the multiplication curves shift downward, showing that the gain increases more slowly at lower γ. For smaller γ values, the multiplication efficiency decreases, meaning the device gain becomes more dependent on the mixed multiplication processes, especially at higher voltages. This behaviour demonstrates that lower absorption coefficients lead to closer alignment with the true uniformly generated M_{mix}.

To more accurately reflect the wavelength-dependent nature of the absorption, a wavelength-dependent multiplication factor was generated for the range of 1500 nm to 2200 nm. This was done through an iterative fitting process. First, the absorption coefficient for a specific wavelength was fed into the RPL (Random Path Length) gain calculation model, producing a gain value. Then, another gain was calculated by dividing the unmultiplied EQE (derived from the input absorption coefficient) by the measured multiplied EQE. The input absorption coefficient was adjusted iteratively until the two gain values closely matched. This method allowed us to account for the actual variations in absorption and multiplication across the wavelength range, rather than assuming a constant factor.

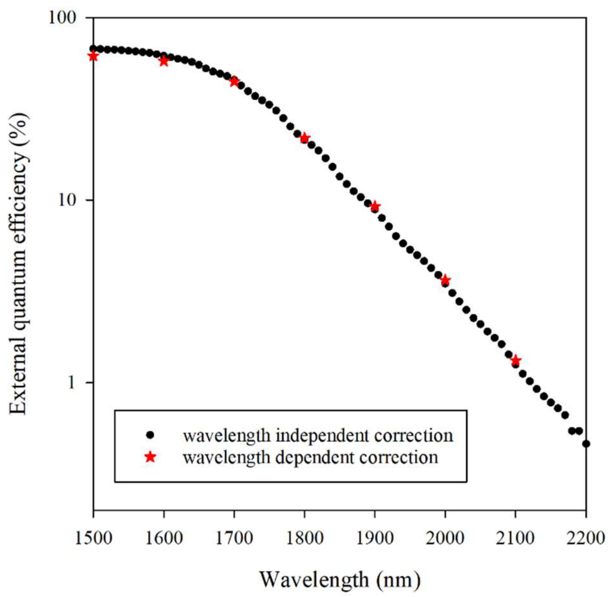

Fig.6.5 The unmultiplied external quantum efficiencies for the 4.8um InGaAs at 205 kV/cm, comparison between the wavelength independent correction and wavelength dependent correction.

Fig. 6.5 compares the unmultiplied EQE using both constant correction (black curve) and wavelength-dependent correction (red stars). Beyond 1650 nm, the difference between the two methods is negligible, as the absorption coefficient remains low and M_{mix} does not vary much. The case shown in Fig. 6.5 represents the thickest InGaAs structure under the highest field conditions, where the variation in gain versus absorption is the largest. Therefore, at lower voltages and for the 1 μm GaAsSb structure, the error is even smaller. The error introduced by assuming a constant M_{mix} remains below 10%, making its impact on the unmultiplied EQE minimal in the wavelength range of interest.

Although the wavelength-dependent correction offers a more accurate reflection of the multiplication factor at shorter wavelengths, where the absorption coefficient is larger, the constant correction provides reliable results under high-field conditions and longer wavelengths, where electroabsorption is most significant. Therefore, while a wavelength-dependent M_{mix} is more precise, the constant correction used in this study is a valid and practical approximation, ensuring that the measured changes in EQE accurately reflect variations in the electroabsorption coefficient rather than overestimations from avalanche multiplication.

6.4.1 The theoretical calculation for electroabsorption effect

To understand the effect of the electric-field on the absorption coefficients, we have attempted to model the electroabsorption due to the Franz-Keldysh effect. The Franz-Keldysh effect, first described by Franz [50] and Keldysh [51] in the late 1950s, involves the tilting of the conduction and valence bands due to an electric field, leading to quantum mechanical tunnelling of electrons from the valence band to the conduction band. Tharmalingam [52] and Callaway [53] introduced an effective mass approximation and used an Airy function for the numerical calculation of the oscillations and decay with photon energy of the electroabsorption coefficient.

The equations to determine the electroabsorption coefficients as given by Tharmalingam [52] and Callaway [53] are:

$$\gamma(\hbar\omega, F) = A \times F^{\frac{1}{3}} \left[\left| \frac{d\,Ai(\beta)}{d\,\beta} \right|^2 - \beta |Ai(\beta)|^2 \right] \tag{6.1}$$

where

$$\beta = B \times (E_g - \hbar\omega) F^{-2/3} \tag{6.2}$$

$Ai(\beta)$ is the Airy function, F is the electric field, $\hbar\omega$ is the energy of the photons, and E_g is the bandgap energy. A is given by Alping [54] as:

$$A = \frac{C}{n\hbar\omega} \left(\frac{2\mu}{m_0}\right)^{4/3} \tag{6.3}$$

while B is given by both Stillman [55] and Alping [54] as:

$$B = 1.1 \times 10^5 \left(\frac{2\mu}{m_0}\right)^{1/3} \tag{6.4}$$

where m_0 is the free electron mass, μ is the reduced mass defined by $\mu = \frac{{m_e}^* {m_h}^*}{{m_e}^* + {m_h}^*}$, where ${m_e}^*$ and ${m_h}^*$ are the relative electron and hole masses, and n is the refractive index. The pre-factor C in Eqn. (4.13), which is associated with the inter-band matrix elements, is a tuneable parameter to be aligned with the empirical zero field absorption coefficient data [118], [123].

The Airy function $Ai(\beta)$, central to the equation, is the mathematical solution to the Schrödinger equation under a linear potential, representing the electric field's perturbation of the crystal's electronic states. The use of the Airy function indicates a one-dimensional treatment of the effect, simplifying the complex three-dimensional reality of the crystal lattice. The airy function is defined by[124]:

$$Ai(\beta) = \frac{1}{\sqrt{\pi}} \int_0^\infty \cos\left(\frac{1}{3}u^3 + \mu\beta\right) du \tag{6.5}$$

The calculation result is shown in Fig.6.6.

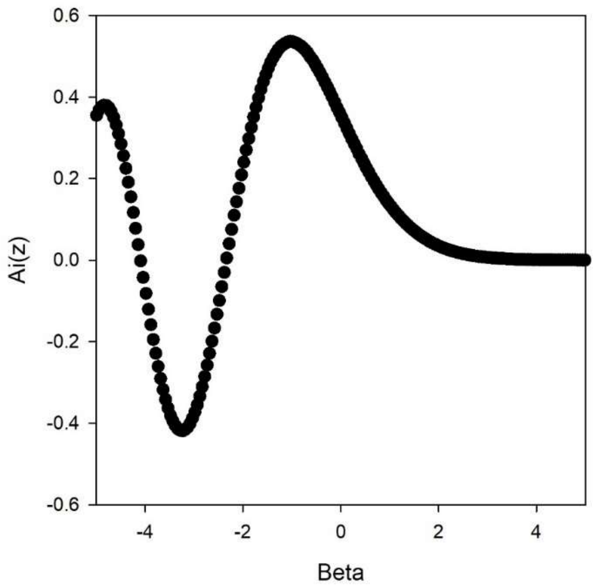

Fig. 6.6 The calculated curve of the Airy function.

Inherent in this model is the presumption of a parabolic band structure near the band edge, a simplification that facilitates the mathematical treatment of the absorption modification. This approach, while streamlining the theoretical description, does not detract from the equation's efficacy in capturing the essence of the electroabsorption effect: the shift and broadening of the optical absorption edge that is experimentally observable and technologically exploitable in devices where electric field control of optical properties is paramount.

However, there are limitations to the model due to these assumptions. The weak field approximation does not hold in cases of very strong electric fields, where non-perturbative effects such as Zener tunnelling become significant[125]. Furthermore, many semiconductors exhibit non-parabolic bands, especially at energies far from the band edge, affecting the accuracy of the electroabsorption effect predictions[126]. Electron-electron and electron-phonon interactions, which can lead to phenomena such as bandgap renormalization and excitonic effects, are not captured by the simple electroabsorption effect equation. Additionally, temperature effects that cause bandgap narrowing at high temperatures are typically not considered[96]. Finally, impact ionization, a non-linear effect more pronounced at higher electric fields, is not accounted for in the electroabsorption model.

6.4.2 Comparison between calculated and measured electroabsorption coefficients

The comparison between calculated and measured electroabsorption coefficients has long been a challenge, with several studies reporting poor agreement between these values. A significant issue is the uncertainty surrounding the bandgap values used in these models. For example, Leeson et al.[123] found that using the conventionally accepted bandgap of 1.42 eV for GaAs did not yield satisfactory fits to the experimental data of Wight et al.[122]. This inconsistency suggests that models relying solely on the conventional bandgap may not accurately represent the electroabsorption behaviour of certain materials.

One key factor contributing to this mismatch is the use of an effective bandgap (E_{ge}), which is smaller than the traditionally accepted value. Recent work by Bhowmick et al.[127] demonstrated that fitting a material's absorption coefficient requires the use of an effective E_{ge} value, typically 12–17 meV smaller than the conventionally accepted bandgap. This finding has significant implications for electroabsorption modelling, as it suggests that E_{ge} should be adopted consistently in such calculations to improve agreement with experimental results. For example, the effective bandgap of InGaAs was found to be 0.733 eV (1690 nm), smaller than its neutral point of 0.747 eV (1660 nm), as shown in Table 6.1. This reduction in E_g has been crucial for obtaining accurate fits to experimental data across various materials.

Table 6.1 The parameters for the calculated absorption coefficient of InGaAs and GaAsSb. Also included is the neutral point for the electroabsorption coefficients.

	InGaAs	GaAsSb
Refractive index, n	3.56	3.65
C	7.2×10^4	6.5×10^4
Effective reduced mass, μ	0.0278	0.0330
Effective Bandgap, E_{ge}	0.733eV (1690nm)	0.738eV (1680nm)
Neutral point, E_g	0.747eV (1660nm)	0.751eV (1650nm)

In addition to the effective bandgap (E_{ge}), the calculation of electroabsorption coefficients also depends on the reduced effective mass (μ), which plays a critical role in the accuracy of these models. As seen in equations (6.1) to (6.4), the reduced mass not only influences the overall magnitude of the electroabsorption coefficients but also determines how these coefficients change with increasing electric field. Kingston[117] suggested that semiconductors with similar values of μ exhibit comparable rates of change in electroabsorption behaviour. By using published values for the electron, light-hole, and heavy-hole masses in InGaAs[90] and GaAsSb[91], we calculated the reduced masses (μ_{lh} and μ_{hh}) for both materials, as shown in Table 6.2. Several studies[122], [123], [128] have used a single effective reduced mass in their calculations, and our findings indicate that using an average value (0.0278 for InGaAs and 0.0330 for GaAsSb, as given in Table 4.1) provides the best fit to our experimental data. Leeson and Payne[123] calculated the electroabsorption coefficient of InGaAs using a larger value of μ=0.038. While using this value of μ with the equations presented in this work gives similar electroabsorption coefficients to Leeson and Payne[123], the absolute values do not agree with the experimental results shown in Fig. 6.7 or the calculations with μ = 0.0278. Furthermore, a comparison of the electroabsorption between InGaAs and GaAsSb shows that InGaAs experiences a slightly larger change with electric field due to its smaller reduced mass, reinforcing the importance of μ in accurately modelling electroabsorption coefficients.

Table 6.2 Summary of mass parameters used for InGaAs and GaAsSb

	InGaAs	GaAsSb
Electron mass, m_e	0.041	0.0447
Light hole mass, m_{lh}	0.052	0.066
Heavy hole mass, m_{hh}	0.363	0.455
Light-hole electron reduced mass, μ_{lh}	0.0227	0.0267
Heavy-hole electron reduced mass, μ_{hh}	0.0368	0.0407

Other adjustable parameters, such as the constant C and the refractive index (n), also play significant roles in obtaining accurate fits. These parameters, alongside the effective bandgap, are integral to calculating the electroabsorption coefficients, which in turn are plotted as a function of wavelength. The calculated values show excellent agreement with experimental data, particularly at higher electric fields, underscoring the validity of this modelling approach.

To further validate the model, we replicated the electroabsorption coefficients calculated by other researchers, such as Seraphin [11] for GaAs using a reduced mass (μ) of 0.065 and Leeson [9, 22], who employed the model of Rees [12]. While Leeson applied this model to both GaAs and InGaAs, using μ values of 0.065 and 0.038 respectively, it is noteworthy that some discrepancies between theory and experiment persist in other works. For instance, Stillman [19] and Wight [23] reported poor agreement between their experimental and theoretical results for GaAs, suggesting that these results should be approached cautiously when interpreting electroabsorption behaviour in similar materials.

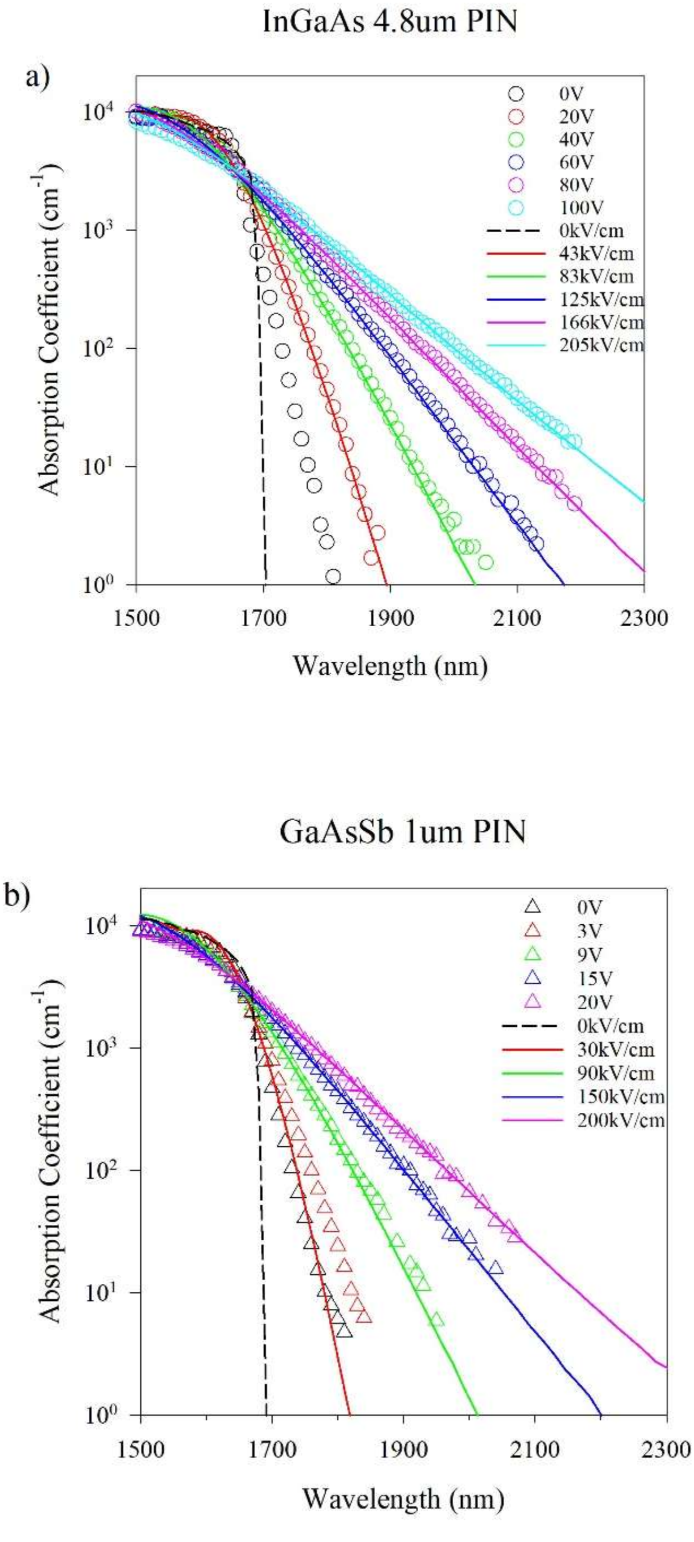

Fig. 6.7 The extracted and calculated absorption coefficients under various reverse bias for (a)InGaAs and (b)GaAsSb photodiodes.

The results of our study show that the electroabsorption coefficients calculated using the effective bandgap and the parameters in Table 6.1 align closely with experimental data at higher electric fields. Similar levels of agreement were found for both InGaAs-A and GaAsSb-B, suggesting that this modelling framework can be reliably extended to other devices with InGaAs or GaAsSb absorption regions. However, at lower electric fields, we observed a slight discrepancy between the calculated and measured values due to Urbach broadening, which limits the accuracy of the model in this regime. Despite this limitation, the overall agreement between the model and the data supports the conclusion that using the effective bandgap (E_{ge}) and the appropriate reduced mass (μ) improves the accuracy of electroabsorption coefficient calculations. Moreover, this physics-based model, with a few adjustable parameters, allows for empirical fits to experimental data, making it a valuable tool for device design and optimization in semiconductor technologies.

6.5 Discussion and conclusion

This work shows that, incorporating InGaAs and GaAsSb in a SACM structure introduces a new performance constraint due to the variations of absorption coefficients, noticeable even when these materials are subjected to a relatively low electric field of 150kV/cm—a level at which many InGaAs SACMs operate at[129], [130]. This work also shows that measuring the photocurrent spectra of a SACM APD structure will give accurate information on the electric field within the absorber region and can be used to optimise the device design.

Fig. 6.8(a) shows how the absorption coefficients decrease with increasing electric field at wavelengths of 1550 nm and 1600 nm. At 1600nm the absorption coefficients decrease from 7113 cm^{-1} to 5225 cm^{-1} in InGaAs and from 7101 cm^{-1} to 5710 cm^{-1} in GaAsSb as the electric field increases from zero to 150 kV/cm. For a 1μm thick absorber region, this change at 1600nm will lead to a notable decline in the internal quantum efficiency (IQE), dropping from 50.8% to 40.7% for InGaAs, and from 50.8% to 43.45% for GaAsSb. This decrease is less pronounced at 1550 nm. In reality, both the electroabsorption reduction and avalanche multiplication may be happening simultaneously to the photons absorbed in the absorber region at high electric fields, making the overall effect less obvious (especially in InGaAs).

Fig. 6.8 (b) also shows that wavelengths beyond the optical bandgap can be detected with increasing efficiency as the electric field increases. These properties could be exploited in waveguide devices to extend the wavelength of conventional short wavelength infrared detectors and APDs albeit at the expense of higher dark currents due to tunnelling.

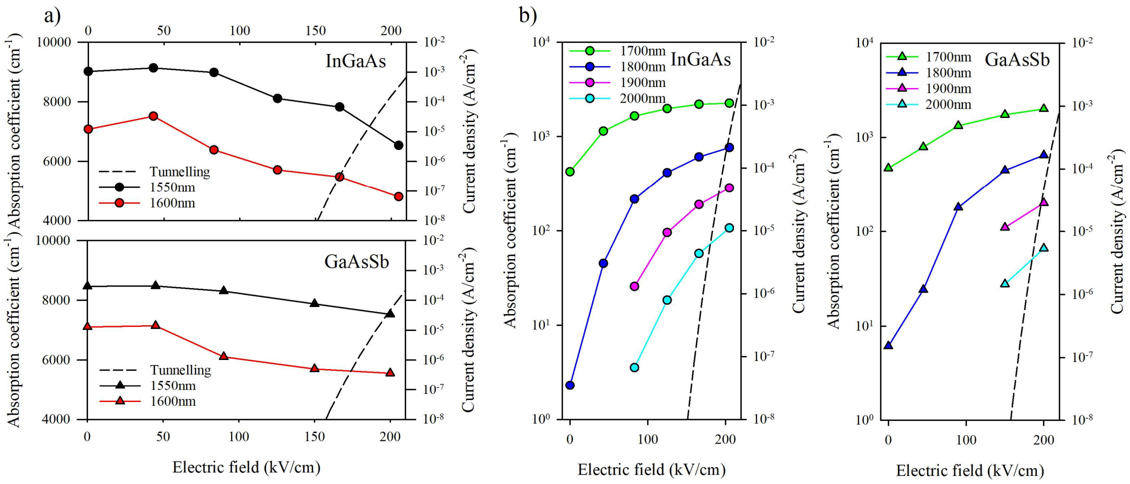

Figure 6.8 The electroabsorption coefficients as a function of electric field for InGaAs(circles) and GaAsSb(triangles) at a) 1550nm(black), 1600nm(red), also shown is the tunnelling dark current density for these two materials as a function of the electric field. b) increasing absorption coefficient with electric field at 1700nm(green), 1800nm(blue), 1900nm(purple) and 2000nm(cyan).

In this chapter, we have conducted experimental measurements and theoretical modelling of the electroabsorption coefficients in bulk InGaAs and GaAsSb under electric fields up to approximately 200 kV/cm. The measurements reveal substantial changes in the absorption properties both above and below the bandgap energies of these materials. The theoretical modelling of the electroabsorption effect aligns closely with the experimental results, confirming the model's accuracy. These findings enhance our understanding of how electric fields impact the absorption characteristics of InGaAs and GaAsSb, which is crucial for the development of high-performance photodetectors, modulators, and other optoelectronic devices. By optimizing these materials for use in optical communication systems, this research provides significant contributions to the field of optoelectronics.

Chapter 7 Characteristics of GaAsSb/AlGaAsSb SACM APD

7.1 Introduction

In the pursuit of high-performance Avalanche Photodiodes (APDs) for telecommunication and sensing applications, a key challenge arises from the trade-off between achieving high sensitivity and maintaining low excess noise. Materials such as 85% AlGaAsSb[108] and InP[131] exhibit excellent characteristics in terms of avalanche multiplication factor and excess noise. However, their detection wavelength range is limited by their relatively large bandgap (1.5 eV, equivalent to 830 nm), which is not ideal for typical telecommunication wavelengths ranging from 1300 to 1650 nm.

To overcome this limitation while maintaining low excess noise, the Separate Absorption, Charge, and Multiplication (SACM) architecture in Avalanche Photodiodes (APDs) has proven effective. SACM APDs are designed to optimize performance in high-speed and high-sensitivity applications by dividing the device into three specialized regions: the absorption region, the charge region, and the multiplication region. In the absorption region, incoming photons generate electron-hole pairs. The charge region, either undoped or lightly doped, extends the electric field uniformly and controls the injection of carriers into the multiplication region. Here, the photocurrent is dramatically amplified through impact ionization.

The separation of the absorption and multiplication zones allows each to be optimized for its specific function, leading to significantly improved device performance. SACM APDs excel in applications requiring high bandwidth and low-noise operation, such as optical communication systems, LiDAR, and high-speed photometry, where they outperform conventional APD designs with lower noise, higher gain, and faster response times.

McIntyre’s local field theory defines the excess noise factor (F) using the equation[27]:

$$F(M) = kM + (1-k)(2-\frac{1}{M}) \quad (7.1)$$

Here, 'k' represents the ratio of ionization coefficients for holes (β) and electrons (α), expressed as $k = \frac{\beta}{\alpha}$ when the multiplication is initiated by electrons. The excess noise factor sets a limit on the maximum useful multiplication achievable for a given device. Therefore, high-sensitivity APDs that require a large signal-to-noise ratio (SNR) must use avalanche materials with a low 'k' value. Materials with significantly different ionization coefficients between electrons and holes not only reduce noise but also enhance bandwidth by minimizing the number of transits through the multiplication region[132].

Silicon avalanche photodiodes (APDs), widely used for visible to near-infrared wavelengths up to 950 nm, are known for their performance, sensitivity, reliability, and cost-effectiveness. However, the 1550 nm wavelength has gained prominence for extended-distance applications due to reduced solar background radiation and scattering, as well as the ability to use higher laser powers while maintaining eye safety[133]. Traditional APD designs for 1550 nm operation typically employ a narrow bandgap material, such as InGaAs, for the absorption region and a wide bandgap material, like InP[35] or InAlAs[134], for the multiplication region, integrated on an InP substrate within a Separate Absorption, Charge, and Multiplication (SACM) configuration. In these designs, the electric field in the absorber is kept low to minimize tunnelling current and impact ionization, while a high electric field in the multiplication region ensures sufficient energy for impact ionization.

Despite their widespread use, commercially available linear mode APDs operating at 1550 nm often face performance limitations due to high excess noise ($F > 10$ at $M = 25$)[18] arising from similar ionization coefficients for electrons (α) and holes (β) at high electric fields[131]. Additionally, undesirable low-field ionization in the InGaAs absorption region negatively affects the gain-bandwidth product[130] and contributes to excess noise[135]. This limitation restricts the maximum useful multiplication and overall device performance.

Alternative materials, such as HgCdTe and InAs, have demonstrated very low excess noise at 1550 nm but require cooling to reduce dark current due to their small bandgap[136], [137]. AlInAsSb, lattice-matched to GaSb, exhibits low excess noise at room temperature beyond 1500 nm but demands complex digital alloy growth techniques[138]. Yi et al.[101] demonstrated exceptionally low excess noise with a k value of 0.005 in a 1550 nm AlAsSb p-i-n structure, though the high aluminum content in this alloy leads to oxidation.

$Al_{0.85}Ga_{0.15}AsSb$ (AlGaAsSb) has emerged as a promising alternative, showing reduced surface dark currents and very low excess noise characteristics[108]. The choice of absorber material plays a crucial role in the performance of SACM structures. As mentioned in previous chapter, using GaAsSb as the absorber material with an $Al_{0.85}Ga_{0.15}AsSb$ multiplication region offers several advantages. The smooth transition between the conduction and valence bands in GaAsSb and $Al_{0.85}Ga_{0.15}AsSb$ avoids abrupt bandgap discontinuities, facilitating easier carrier movement, reducing the likelihood of carrier entrapment, and increasing device speed. Additionally, the transition from GaAsSb to $Al_{0.85}Ga_{0.15}AsSb$ primarily requires adjustments in the group III elements, simplifying the process of achieving lattice-matched growth. In contrast, InGaAs, with its type II band alignment, presents a significant challenge due to the large conduction band offset (~1 eV) between the last grading layer and the $Al_{0.85}Ga_{0.15}AsSb$ multiplier, complicating the grading process and potentially affecting device efficiency and speed.

The excess noise and multiplication characteristics of $Al_{0.85}Ga_{0.15}AsSb$ *p-i-n* diodes with different avalanche region thicknesses have been extensively studied recently[139]. It was concluded that a 1 µm *p-i-n* structure exhibits low excess noise and is suitable for LiDAR applications due to its ability to operate at high multiplication values. Building on these insights, this work presents an SACM architecture using a novel $GaAs_{0.5}Sb_{0.5}$/ $Al_{0.85}Ga_{0.15}AsSb$ (GaAsSb/AlGaAsSb) structure, which offers significant improvements in multiplication and excess noise for operation at 1550 nm.

In this chapter, a SACM structure based on a GaAsSb absorber and an 85% AlGaAsSb multiplier is fabricated and thoroughly characterized in terms of its electrical and optical performance. The GaAsSb/AlGaAsSb structure was chosen for its ability to deliver high gain with low excess noise, crucial for applications in the 1550 nm wavelength range. The characterization focuses on the capacitance-voltage (C-V), current-voltage (I-V), quantum efficiency (QE), and multiplication characteristics. Through these measurements, the advantages of using a GaAsSb absorber in combination with an AlGaAsSb multiplication region are demonstrated, showing that this structure is capable of significantly improved performance for telecommunication and sensing applications, particularly in high-sensitivity, low-noise scenarios.

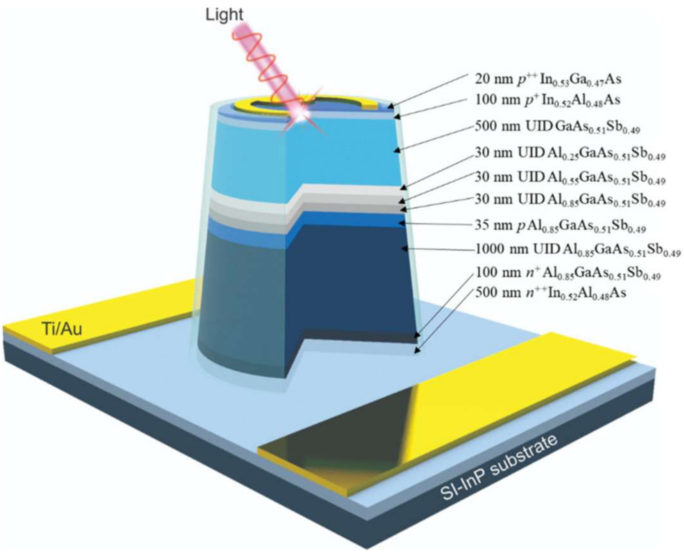

Fig. 7.1 the schematics of GaAsSb/AlGaAsSb SACM APDs.

7.2 Device structure

The GaAsSb/AlGaAsSb SACM APDs were grown via molecular beam epitaxy on a semi-insulating InP substrate using random alloy (RA) growth technique. For the group V cells, RIBER VAC 500 and Veeco Mark V valved crackers were employed for As and Sb, respectively. As summarized in Table 7.1, this structure included a nominal 500 nm GaAsSb absorber and 1000 nm AlGaAsSb, incorporating a 35 nm charge sheet layer with p-type doping of 6×10^{17} cm^{-3}. This doping ensures a low electric field in the absorber, preventing tunnelling, while maintaining a high electric field in the multiplication region to facilitate avalanche multiplication. The energy bands are graded using various compositions of AlGaAsSb to enable smooth carrier migration from the absorber to the multiplication region. Device fabrication involved standard photolithography and wet etching in a solution composed of 40 ml citric acid:10ml phosphoric acid:10ml H_2O_2:240 ml deionized water. This process etches the devices into a clear mesa shape with diameters ranging from 60 µm to 500 µm, and the surface was passivated using SU-8. Ti/Au was deposited on the top and bottom contact layers for ohmic contact.

Table 7.1 The layer details of the SACM APDs

Layer	Material	Doping density/cm^{-3}	Thickness/nm
Top contact	InGaAs	1×10^{19} p^{++}	20
Cladding	InAlAs	5×10^{18} p^{+}	100
Absorber	$GaAs_{0.5}Sb_{0.5}$	UID	500
Grading	$Al_{0.25}Ga_{0.15}AsSb$	UID	30
Grading	$Al_{0.55}Ga_{0.15}AsSb$	UID	30
Grading	$Al_{0.85}Ga_{0.15}AsSb$	UID	30
Charge sheet	$Al_{0.85}Ga_{0.15}AsSb$	6×10^{17} p	35
Multiplier	$Al_{0.85}Ga_{0.15}AsSb$	UID	1000
Contact	$Al_{0.85}Ga_{0.15}AsSb$	5×10^{18} n^{+}	100
Buffer	InAlAs	1×10^{19} n^{++}	500
Substrate	InP	Semi-insulating	N/A

7.3 IV and CV characteristics

The capacitance-voltage (C-V) measurements and doping profile analysis of the GaAsSb/AlGaAsSb SACM APD, as illustrated in Figure 7.2, provide crucial insights into the device structure and electrical characteristics. Fig. 7.2(a) illustrates the capacitance per unit area for different sized devices (D500, D350, D200, and D150). The overlapping curves demonstrate excellent consistency in the capacitance per unit area across various device dimensions, this scaling behaviour validates the accuracy of the mesa etching process and the uniformity of the epitaxial layers.

All devices show a similar trend in capacitance reduction as the reverse bias voltage increases. The capacitance per unit area gradually decreases from about 7 nF/cm² at zero bias to approximately 4.5 nF/cm² at 30 V. A sharp drop in capacitance is observed around 40 V for all device sizes, indicating the punch-through voltage where the depletion region extends into the absorption layer.

Fig. 7.2(b) shows the C-V fitting for the D200 device. The close agreement between the measured data (black dots) and the simulated fit (red line) validates the accuracy of the Poisson-based electric field simulation. This simulation is based on the device structure detailed in Table. 7.2, which outlines the material composition, permittivity, doping density, and thickness of each layer in the SACM APD. The absorber and multiplication regions have thicknesses of 450 nm and 1050 nm, respectively, with corresponding doping levels of 4.5×10^{15} cm^{-3} and 4×10^{15} cm^{-3}. The charge sheet, a critical component in SACM APDs for field control, was found to be 59 nm thick with a p-type doping concentration of 6×10^{17} cm^{-3}. This results in a total charge within the charge sheet of approximately 3.54×10^{12} cm^{-2}.

Table 7.2 The simulated structure for Poisson CV calculation

Material	Permittivity	Doping density/cm^{-3}	Thickness/nm
InGaAs (Top contact)	14	1×10^{19} p^{++}	20
$GaAs_{0.5}Sb_{0.5}$ (Absorber)	14	4.5×10^{15} p	450
$Al_{0.25}Ga_{0.15}AsSb$ (Grading)	13	2×10^{16} p	30
$Al_{0.55}Ga_{0.15}AsSb$ (Grading)	12	4×10^{16} p	30
$Al_{0.85}Ga_{0.15}AsSb$ (Grading)	11.4	5×10^{16} p	30
$Al_{0.85}Ga_{0.15}AsSb$ (Charge sheet)	11.4	6×10^{17} p	59
$Al_{0.85}Ga_{0.15}AsSb$ (Multiplier)	11.4	4×10^{15} p	1050
$Al_{0.85}Ga_{0.15}AsSb$ (Bottom Contact)	11.4	5×10^{18} n^{++}	100

Figure 7.2(c) showed the doping profile as a function of depletion width for different device sizes extracted directly from the C-V measurements. The charge sheet is clearly visible as a peak in the doping profile, centred around 1.1 μm depletion width. The peak doping density in the charge sheet is approximately 3-4 × 10^{17} cm^{-3}, aligning closely with the designed value. By integrating the area under this peak, we can estimate the total charge in the charge sheet region as 2.7 × 10^{12} cm^{-2}.

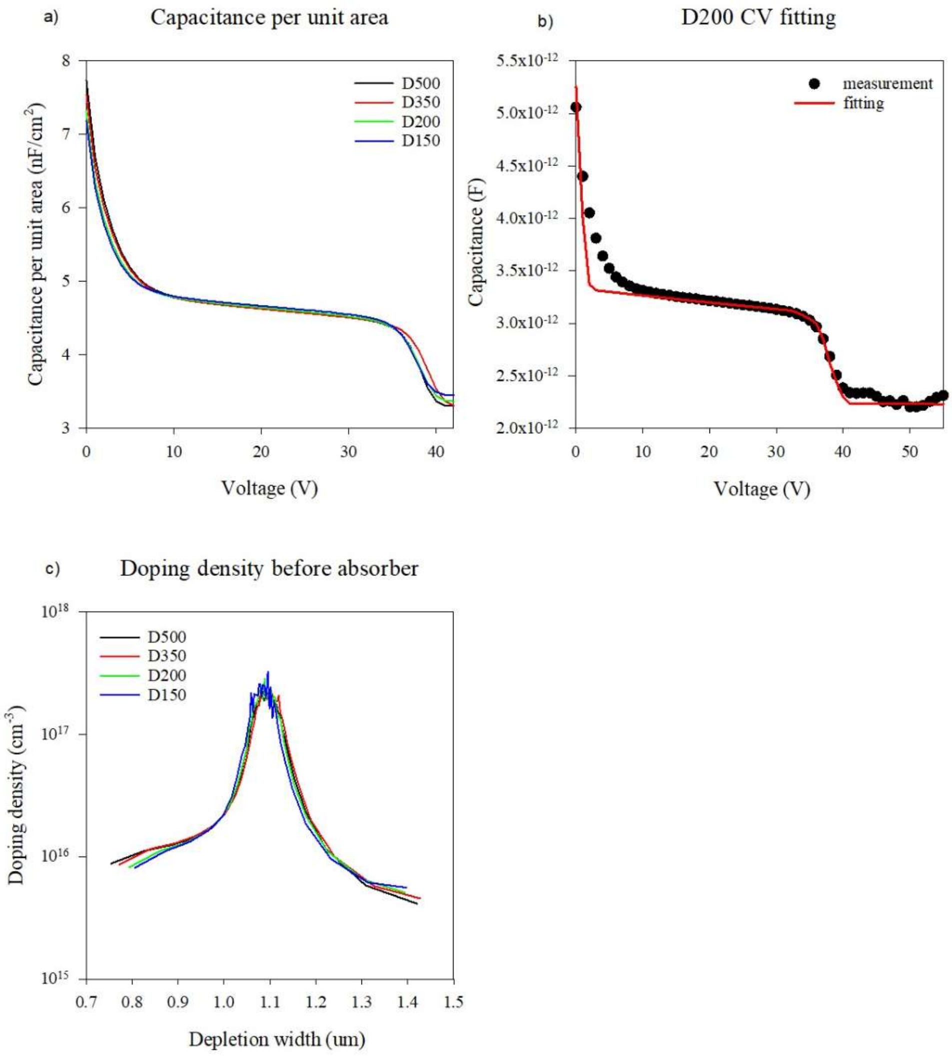

Fig. 7.2 The capacitance-voltage measured of the SACM APDs with different size.

The electric field distribution in this SACM APD structure is shown in Fig. 7.3, where the AlGaAsSb multiplication region supports an electric field of over 600 kV/cm at breakdown voltage, allowing for strong avalanche multiplication. Meanwhile, the GaAsSb absorber operates in a low-field region (<180 kV/cm) to minimize tunnelling currents, maintaining low dark current while allowing efficient carrier multiplication.

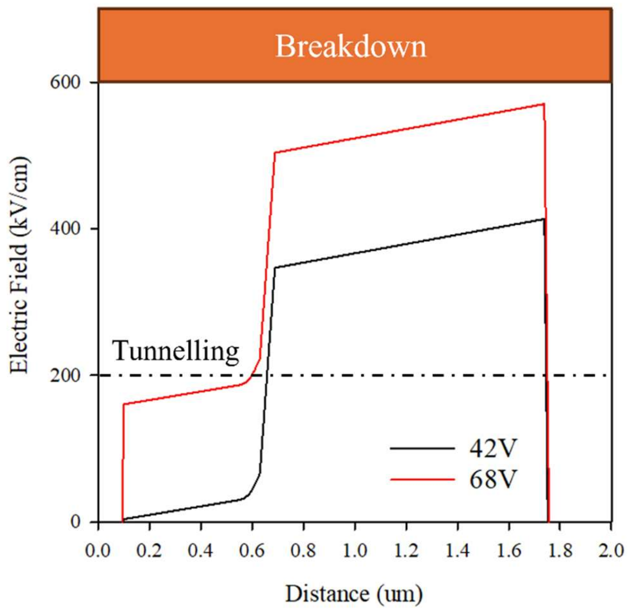

Fig.7.3 The electric field profile of the SACM APDs at punch through voltage and breakdown voltage.

The forward and reverse current-voltage (I-V) characteristics of GaAsSb/AlGaAsSb SACM APD devices with varying diameters are shown in Figure 7.4. The forward current (Figures 7.4(a) and 7.4(b)) scales with area for bias below 1 V, but bends over as the forward bias approaches 1.5 V.

Figures 7.4(c) and 7.4(d) depict the reverse dark current and its density, respectively. Before punch-through, the dark current scales with the device perimeter, suggesting that surface leakage mechanisms, such as generation and recombination at defects or perimeter states, dominate. After punch-through, the dark current scales better with the area of the devices, as shown in Figure 7.4(d), indicating that generation and recombination processes in the bulk GaAsSb absorption layer dominate the current. The punch-through voltage (V_{pt}) is around 42 V, while the avalanche breakdown voltage (V_{bd}) occurs at approximately 68 V. Slight variations in these voltages across devices can be attributed to edge effects and non-uniformities in doping and layer thickness.

The reverse dark current density remains relatively low up to 40 V, ranging from 10^{-6} A/cm² to 10^{-5} A/cm². Beyond punch-through, the current density increases as the electric field penetrates the absorber. At 54 V (just after punch-through), the reverse dark current density is 0.1 mA/cm^{-2}.

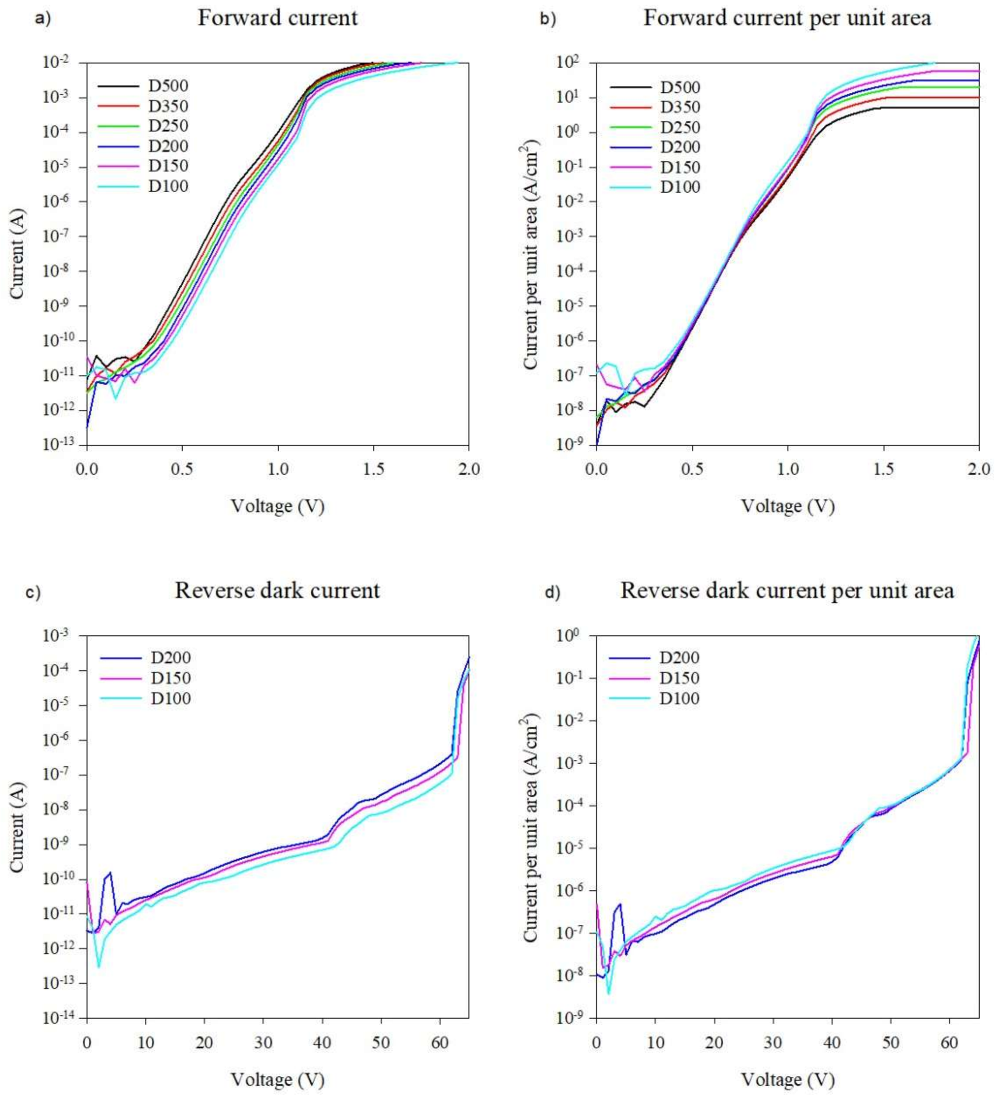

Fig.7.4 The IV characteristics of the SACM APDs.

7.4 Experiment results

Fig. 7.5 illustrates the avalanche multiplication characteristics of the SACM APD under different reverse biases at 1450 nm. Fig.7.5(a) shows the measured dark current and total photocurrent for the SACM APD at various illumination power levels from a 940 nm LED. The dark current remains minimal across the voltage sweep until near breakdown voltage, indicating effective suppression of dark current by the device. For the highest optical power, the photocurrent exceeds the dark current by more than three orders of magnitude, indicating a large signal-to-noise ratio. This establishes a clear distinction between dark current and photocurrent, allowing for the reliable calculation of gain by subtracting the dark current from the total measured current.

Figure 7.5(b) shows the gain calculated from the SMU measurements in Figure 7.5(a) alongside the gain measured using a Lock-In Amplifier (LIA). The solid lines represent the gain derived from the SMU sweep by subtracting the dark current from the total current, with the reference gain set at M=3.6 at 54 V. The open symbols represent the gain measured using the LIA technique, using the phase-sensitive detection method described in Chapter 3. The close match between these two methods confirms the reliability of both approaches for measuring gain.

Figure 7.5(c) presents the measured dark current and gain along with the fitted gain from the Random Path Length (RPL) model. The RPL model uses the electric field distribution profile derived from capacitance-voltage (CV) modelling and the impact ionization coefficients of AlGaAsSb, which were published previously[108]. The experimental gain, represented by symbols, shows strong agreement with the modelled gain (red curve) across the voltage range, particularly for voltages exceeding 54 V. The multiplication is determined to be M=3.6 at 54 V, and the predictions agree well with the measured data up to a gain of M=1150.

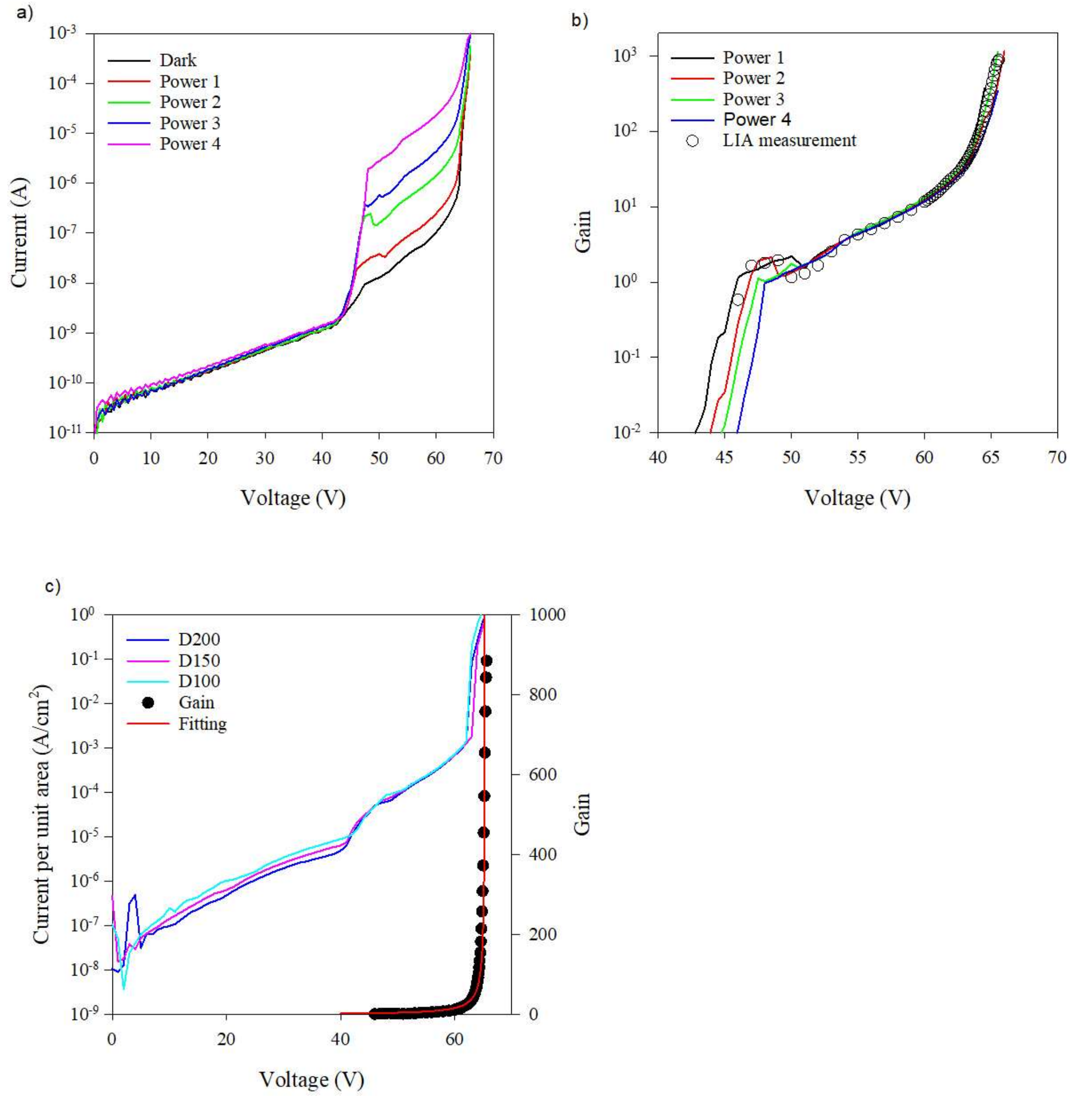

Fig. 7.5 (a) Dark current and photocurrent under different 940 nm illumination powers. (b) Gain calculated from SMU measurements compared with LIA measurements, showing good agreement. (c) Current density and gain for different device sizes, with the RPL model fitting.

Fig. 7.6 presents the measured responsivity and quantum efficiency (QE) spectra of the SACM APD across a range of reverse bias voltages. Figure 7.6(b) illustrates the corresponding quantum efficiency (QE) for the same set of reverse biases. At lower reverse biases (41 V to 46 V), the QE remains relatively low, especially at longer wavelengths, due to limited avalanche multiplication. However, as the reverse bias increases to around 54 V and beyond, the QE rises significantly, reaching over 1000% at higher voltages. At 54 V, the EQE is measured as 77%, with calculations based on a 450 nm thick absorber and an absorption coefficient of 8100 cm^{-1} suggesting an EQE of approximately 21.4% at unity gain. This corresponds to a multiplication gain of around 3.6, aligning well with the multiplication simulation results for 1550 nm. As a results, under maximum multiplication conditions (M = 1150), the device achieved an exceptionally high quantum efficiency of 24610%.

Additionally, as the reverse voltage increases, the cutoff wavelength extends towards 1900 nm due to the electroabsorption effect, which broadens the absorption edge of the material. This shift enhances the APD's ability to detect longer wavelengths, making it suitable for applications involving infrared light detection.

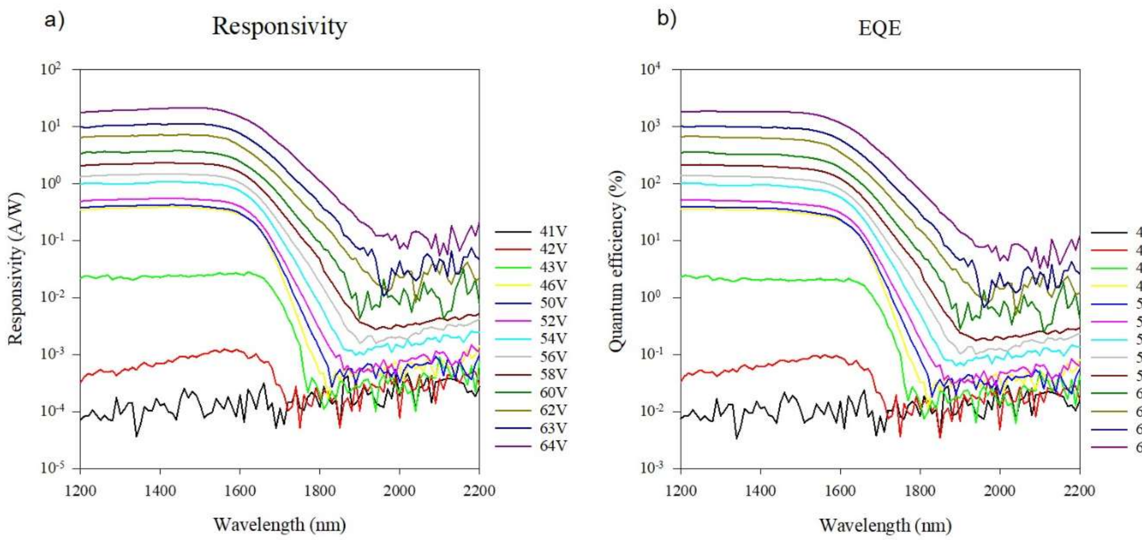

Fig. 7.6 (a) Responsivity and (b) EQE of the SACM APD across different reverse biases.

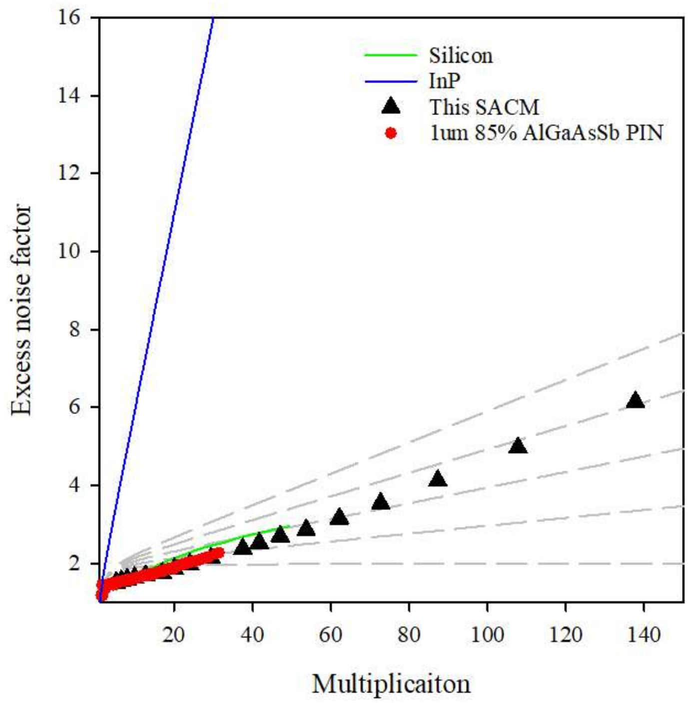

Fig. 7.7 the excess noise measurements of the SACM APDs, in comparison with the 1um 85%AlGaAsSb, Silicon and InP.

Fig. 7.7 illustrates the measured excess noise factor as a function of multiplication for the SACM APD and compares it with a 1 μm thick 85% AlGaAsSb *p-i-n* diode. The excess noise measurements were conducted using a transimpedance amplifier-based circuit, operating at a centre frequency of 10 MHz with a bandwidth of 4.2 MHz. Calibration of shot noise was achieved using a reference silicon photodiode (SFH2701), which lacks multiplication, allowing for accurate determination of the excess noise factor by comparing the measured noise power of the SACM APD with that of the silicon device at a given photocurrent. The details methodology is described in detail in Chapter 3.

The measured excess noise of the SACM structure is presented in Fig. 7.7, showing excellent noise performance across a range of multiplication values. The excess noise remains low up to a multiplication factor of 150, demonstrating a substantial advantage over conventional APDs. Notably, the device does not follow McIntyre’s local theory, where the excess noise factor typically rises more rapidly with increasing multiplication.

The excess noise factor F of the SACM APD is approximately 5 times lower than that of a commercial InP APD. This substantial reduction in noise highlights the superior performance of the AlGaAsSb-based multiplication region. When compared to commercial silicon (Si) APDs, the SACM APD demonstrates similar excess noise characteristics at multiplication values below 25. However, for multiplication values greater than 25, the SACM APD outperforms the Si APD, exhibiting lower excess noise. This is particularly noteworthy, as Si APDs are renowned for their low noise in the visible spectrum, but they typically require much higher operating bias voltages to achieve such low noise factors.

The ability of the SACM APD to maintain lower excess noise at higher multiplication values, combined with its operation at lower bias voltages, makes it highly advantageous. Furthermore, the AlGaAsSb multiplication region provides a significant benefit in terms of extended detection wavelengths, as Si APDs are limited to shorter wavelengths, typically in the visible range. In contrast, the SACM APD operates efficiently in the near-infrared region, making it a more promising solution for applications that require both low-noise performance and sensitivity at extended wavelengths.

7.5 Discussion and Conclusion

In Table 7.3, a comparison is made between the GaAsSb/AlGaAsSb SACM APD developed in this work and other commercially available InGaAs APDs with a 200 μm diameter. The state-of-the-art InGaAs/InP device (G14858-0020AA)[103] is noted for its low dark current and a similar breakdown voltage to the SACM APD. However, this work achieves a significantly higher multiplication factor of 1150, nearly 30 times greater than the InGaAs/InP device, while maintaining an excess noise that is 6.5 times lower at M=25.

The thin 500 nm GaAsSb absorber used in this study yields a quantum efficiency (QE) of 21.4% at unity gain without the use of an anti-reflection (AR) coating. By incorporating a thicker 2 μm GaAsSb absorber with an AR coating in the SACM structure, the QE could be improved to 87% at unity gain, with only a slight increase in dark current and a marginal reduction in speed. Additionally, integrating a thicker InGaAs or GaAsSb absorber in a SACM configuration with this type of multiplication region could result in even better overall performance. The comparison in Table 7.3 highlights key parameters, such as breakdown voltage and excess noise, demonstrating that the SACM APD developed in this study offers superior performance. With a maximum multiplication factor of 1150 and an excess noise factor of around 2 at M=25, the SACM APD shows a considerable improvement in noise and multiplication compared to commercial APDs, which typically exhibit higher excess noise and lower gain.

In conclusion, the GaAsSb/AlGaAsSb SACM APD presented in this chapter, which is lattice-matched to InP, offers high gain and low excess noise, significantly enhancing sensitivity for 1550 nm detection. These characteristics represent a substantial advancement over current commercial APDs, providing a promising solution for applications like lidar systems and other technologies that require high sensitivity and fast response times.

Table 7.3 Comparison of this work with the commercial device.

Parameters	Excelitas (C30662)	Hamamatsu (G8931-20)	Hamamatsu (G14858-0020AA)	SACM (This study)
Device diameter	200 µm	200 µm	200 µm	200 µm
Spectrum range	~1.7µm	~1.7µm	~1.7µm	~1.7µm
Capacitance @Max Depletion	2.5pF	1.5pF	2 pF	2 pF
Breakdown Voltage	50V	55V	65 V	66V
C_{bd}	140mV/K	110 mV/K	100 mV/K	N/A
Bandwidth	0.85GHz	0.9GHz	0.9 GHz	N/A
Max Multiplication	~20	~30	~30	1150
Excess noise @ M = 25	3.4@M=10	~13	~13	~2
Dark current @ M = 25	4.5nA@ M=10	2280nA	20nA	214nA

In summary, this chapter presents the development and characterization of a GaAsSb/AlGaAsSb SACM APD lattice-matched to InP, demonstrating high gain and exceptionally low excess noise. This device achieves significant improvements in sensitivity for 1550 nm detection compared to state-of-the-art commercial APDs, with a much higher multiplication factor and drastically lower excess noise. These advanced characteristics make the GaAsSb/AlGaAsSb SACM APD an ideal candidate for applications requiring high sensitivity and fast response times, such as LiDAR systems, high-speed optical communication, and advanced photodetection technologies.

Chapter 8 Conclusion and future work

8.1 Conclusion

This thesis has demonstrated the significant potential of GaAsSb/AlGaAsSb Separate Absorption Charge and Multiplication (SACM) avalanche photodiodes (APDs) for high-performance optoelectronic applications, particularly in the short-wave infrared (SWIR) spectrum and at the 1550 nm telecom wavelength. GaAsSb demonstrated advantages over InGaAs-based devices in terms of noise reduction, field-dependent absorption, and controlled multiplication.

Accurate absorption measurements showed that GaAsSb and InGaAs have comparable absorption coefficients around 1550 nm, with values of approximately 8400 cm^{-1} and 8100 cm^{-1}, respectively. These results confirm the suitability of both materials for photodetectors operating in the telecom C- and L-bands. Additionally, GaAsSb devices exhibited low dark current, supporting their viability as an alternative to InGaAs.

Electroabsorption studies conducted at 1550 nm and 1600 nm revealed a reduction in absorption coefficients as the electric field increased. For instance, at 1600 nm, the absorption coefficient for InGaAs decreased from 7113 cm^{-1} to 5225 cm^{-1}, and for GaAsSb, it decreased from 7101 cm^{-1} to 5710 cm^{-1} as the electric field rose from 0 to 150 kV/cm. This reduction in absorption impacts the internal quantum efficiency (IQE), with InGaAs showing a drop in IQE from 50.8% to 40.7%, and GaAsSb from 50.8% to 43.45% in 1 μm devices. Although the decrease is less pronounced at 1550 nm, this demonstrates how increasing the electric field in the absorber region influences the overall device performance.

Multiplication measurements indicated that GaAsSb offers lower electron multiplication than InGaAs at electric fields below 210 kV/cm. Specifically, at an electric field of 175 kV/cm, the electron multiplication factor for GaAsSb was measured at 1.038, compared to 1.138 for InGaAs. This behaviour, tied to lower electron ionization coefficient (α) in GaAsSb at this field range, results in significantly lower multiplication but also correlates with reduced noise and limited tunnelling currents. These characteristics make GaAsSb particularly advantageous for applications requiring low noise and high signal clarity at moderate fields, where excessive multiplication can introduce unwanted noise.

GaAsSb/AlGaAsSb SACM APDs demonstrated high multiplication ($M > 1200$) and low excess noise ($F < 7$ at $M = 200$) at room temperature. Compared to commercially available InGaAs/InP devices, these APDs offered a 40-fold improvement in maximum multiplication and a 6.5 times reduction in excess noise at $M = 25$. Additionally, photocurrent spectral measurements enabled accurate optimization of the electric field distribution within the absorber region, which is crucial for minimizing tunnelling currents and maximizing quantum efficiency.

8.2 Future work

This thesis has demonstrated the design and characteristics of GaAsSb/AlGaAsSb Separate Absorption Charge and Multiplication (SACM) APDs for high-performance optoelectronic applications. However, several areas require further exploration to fully optimize device performance and explore new materials and structures. Future research should focus on the following key areas:

1. Impact Ionization Coefficients in *n-i-p* GaAsSb Devices

Developing *n-i-p* GaAsSb devices could enable more accurate determination of impact ionization coefficients, particularly for the hole ionization coefficient (β). Current data on β in GaAsSb remains incomplete. *n-i-p* structures allow for pure hole injection through top illumination, in contrast to *p-i-n* devices with only possible mixed injection and pure electron injection. This would provide more accurate determination of hole-initiated ionization.

1. Temperature Dependence and Varshni Shift in GaAsSb

Future studies should investigate the temperature dependence of GaAsSb, particularly how its bandgap shifts with temperature (Varshni effect), by conducting low-temperature measurements down to 20K and high temperature up to 350K. Such studies will provide valuable insights into the dark current, ionization coefficients, and breakdown voltage (Cbd) under varying temperature conditions.

While low temperatures may improve avalanche gain and reduce noise, the expansion of the bandgap at lower temperatures could shrink the device's detection range, especially in the short-wave infrared (SWIR) spectrum. Careful consideration is needed to balance the advantages of low noise with the potential trade-off of limited detection range.

2. Electroabsorption for Electric Field Determination in SACM Structures

The electroabsorption effect in GaAsSb and InGaAs could be used to accurately measure the electric field distribution within SACM structures, where direct measurements are difficult. By analysing the shift and broadening of the absorption edge, researchers could determine the electric field in both vertical and planar SACM structures in real-time. This would enable the development of more accurate models of field behaviour and allow for the optimization of absorption and multiplication processes.

3. Optimization of Device Speed and Bandwidth

Response speed is critical for the performance of GaAsSb/AlGaAsSb SACM APDs in high-speed communication systems. Future work should focus on measuring the bandwidth of these devices using fast pulsed lasers to avoid the limitations of commercial LEDs. By analysing the cut-off frequency and signal rise time, the high-speed characteristics of these APDs can be better understood and optimized for faster response times.

4. InGaAs/GaAsSb Type-II Superlattices (T2SL) for Wavelength Extension

Future research could explore InGaAs/GaAsSb Type-II Superlattices (T2SL) as potential absorbers to extend the operational wavelength of SACM APDs up to 3 μm. T2SL structures, made by alternating layers of InGaAs and GaAsSb, can be grown on InP substrates using well-established III-V growth techniques. Tailoring the well and barrier thicknesses in these superlattices could allow for longer-wavelength applications, such as gas detection and SWIR sensing.

Investigating the electroabsorption properties of the proposed T2SL structures would provide insights into how the electric field influences absorption in these systems. The potential for quantum confined electroabsorption effect in these superlattices is especially intriguing, as it could enable precise control over light absorption and emission at the quantum level.

5. Photon Counting and High-Sensitivity Applications

A promising area for further exploration is the operation of GaAsSb/AlGaAsSb SACM APDs as Single-Photon Avalanche Diodes (SPADs) in Geiger mode. Given the devices' high gain and low excess noise characteristics, they present strong potential for photon-counting and single-photon detection applications. Future research should focus on measuring photon detection efficiency (PDE) and dark count rate (DCR) to evaluate their performance in photon-counting mode, particularly in the 1550 nm wavelength range.

Operating the devices above breakdown voltage would enable single-photon avalanche events, with both passive and active quenching circuits needed to control and reset the avalanche. Comparative studies with commercially available InGaAs/InP SPADs could quantify improvements in noise performance, gain, and timing jitter. These investigations would pave the way for utilizing GaAsSb-based SPADs in applications like LiDAR, low-light imaging, and quantum cryptography, where single-photon detection is critical.

References

[1] G. Keiser, 'Optical Fiber Communications', in *Wiley Encyclopedia of Telecommunications*, 1st ed., J. G. Proakis, Ed., Wiley, 2003. doi: 10.1002/0471219282.eot158.

[2] K. C. Kao and G. A. Hockham, 'Dielectric-fibre surface waveguides for optical frequencies', *Proc. Inst. Electr. Eng.*, vol. 113, no. 7, pp. 1151–1158, Jul. 1966, doi: 10.1049/piee.1966.0189.

[3] F. P. Kapron, D. B. Keck, and R. D. Maurer, 'RADIATION LOSSES IN GLASS OPTICAL WAVEGUIDES', *Appl. Phys. Lett.*, vol. 17, no. 10, pp. 423–425, Nov. 1970, doi: 10.1063/1.1653255.

[4] R. Ramaswami, K. Sivarajan, and G. Sasaki, *Optical Networks: A Practical Perspective*. in Morgan Kaufmann series in networking. Morgan Kaufmann, 2009. [Online]. Available: https://books.google.co.uk/books?id=WpByp4Ip0z8C

[5] Y. Yamamoto and T. Kimura, 'Coherent optical fiber transmission systems', *IEEE J. Quantum Electron.*, vol. 17, no. 6, pp. 919–935, Jun. 1981, doi: 10.1109/JQE.1981.1071225.

[6] J. A. Buck, *Fundamentals of Optical Fibers*. in Wiley Series in Pure and Applied Optics. Wiley, 2004. [Online]. Available: https://books.google.co.uk/books?id=-QCwrBxRtiwC

[7] T. Miya, Y. Terunuma, T. Hosaka, and T. Miyashita, 'Ultimate low-loss single-mode fibre at 1.55 μm', *Electron. Lett.*, vol. 15, no. 4, p. 106, 1979, doi: 10.1049/el:19790077.

[8] E. Desurvire, *Erbium-doped fiber amplifiers: principles and applications*. in A Wiley-Interscience publication. New York: Wiley, 1994.

[9] J. Shan and C. K. Toth, Eds., *Topographic laser ranging and scanning: principles and processing*, Second edition. Boca Raton: CRC Press, 2023.

[10] G. Vosselman, Ed., *Airborne and terrestrial laser scanning*, Repr. Caithness: Whittles Publ, 2011.

[11] R. Sabatini, M. A. Richardson, A. Gardi, and S. Ramasamy, 'Airborne laser sensors and integrated systems', *Prog. Aerosp. Sci.*, vol. 79, pp. 15–63, Nov. 2015, doi: 10.1016/j.paerosci.2015.07.002.

[12] F. Amzajerdian, M. Vanek, L. Petway, D. Pierrottet, G. Busch, and A. Bulyshev, 'Utilization of 3D imaging flash lidar technology for autonomous safe landing on planetary bodies', presented at the OPTO, M. Razeghi, R. Sudharsanan, and G. J. Brown, Eds., San Francisco, California, Jan. 2010, p. 760828. doi: 10.1117/12.843324.

[13] C. Weitkamp, *Lidar: Range-Resolved Optical Remote Sensing of the Atmosphere*. in Springer Series in Optical Sciences. Springer, 2005. [Online]. Available: https://books.google.co.uk/books?id=8AT2smoj4MkC

[14] B. Schwarz, 'Mapping the world in 3D', *Nat. Photonics*, vol. 4, no. 7, pp. 429–430, Jul. 2010, doi: 10.1038/nphoton.2010.148.

[15] F. Capasso, 'Band-Gap Engineering: From Physics and Materials to New Semiconductor Devices', *Science*, vol. 235, no. 4785, pp. 172–176, Jan. 1987, doi: 10.1126/science.235.4785.172.

[16] G. E. Stillman and C. M. Wolfe, 'Chapter 5 Avalanche Photodiodes', in *Semiconductors and Semimetals*, vol. 12, Elsevier, 1977, pp. 291–393. doi: 10.1016/S0080-8784(08)60150-7.

[17] S. M. Sze and K. K. Ng, *Physics of Semiconductor Devices*, 1st ed. Wiley, 2006. doi: 10.1002/0470068329.

[18] Hamamatsu, 'G1458-0020AA'. Accessed: May 15, 2024. [Online]. Available: https://www.hamamatsu.com/content/dam/hamamatsu-photonics/sites/documents/99_SALES_LIBRARY/ssd/g14858-0020aa_kapd1068e.pdf

[19] 'Thorlab FDO5D specsheet'. [Online]. Available: https://www.thorlabs.com/thorcat/TTN/TTN035395-S01.pdf

[20] D. Z. Ting *et al.*, 'Advances in III-V semiconductor infrared absorbers and detectors', *Infrared Phys. Technol.*, vol. 97, pp. 210–216, Mar. 2019, doi: 10.1016/j.infrared.2018.12.034.

[21] J. C. Campbell, 'Recent Advances in Avalanche Photodiodes', *J Light. Technol*, vol. 34, no. 2, pp. 278–285, Jan. 2016.

[22] F. Capasso, 'Chapter 1 Physics of Avalanche Photodiodes', in *Semiconductors and Semimetals*, vol. 22, Elsevier, 1985, pp. 1–172. doi: 10.1016/S0080-8784(08)62952-X.
[23] J. Mort and D. M. PAI, *Photoconductivity and Related Phenomena*. Elsevier Scientific Publishing Company, 1976. [Online]. Available: https://books.google.co.uk/books?id=Q-KZAAAAIAAJ
[24] HAMAMATSU, *PHOTOMULTIPLIER TUBES Basics and Applications*.
[25] J. Liu, *Photonic Devices*, 1st ed. Cambridge University Press, 2005. doi: 10.1017/CBO9780511614255.
[26] M. A. Itzler, U. Krishnamachari, M. Entwistle, X. Jiang, M. Owens, and K. Slomkowski, 'Dark Count Statistics in Geiger-Mode Avalanche Photodiode Cameras for 3-D Imaging LADAR', *IEEE J Sel Top Quantum Electron*, vol. 20, no. 6, pp. 318–328, Nov. 2014, doi: 10.1109/jstqe.2014.2321525.
[27] R. J. McIntyre, 'Multiplication noise in uniform avalanche diodes', *IEEE Trans. Electron Devices*, vol. ED-13, no. 1, pp. 164–168, Jan. 1966, doi: 10.1109/T-ED.1966.15651.
[28] M. A. Green and M. J. Keevers, 'Optical properties of intrinsic silicon at 300 K', *Prog. Photovolt. Res. Appl.*, vol. 3, no. 3, pp. 189–192, Jan. 1995, doi: 10.1002/pip.4670030303.
[29] H. Ando, H. Kanbe, T. Kimura, T. Yamaoka, and T. Kaneda, 'Characteristics of germanium avalanche photodiodes in the wavelength region of 1-1.6 µm', *IEEE J. Quantum Electron.*, vol. 14, no. 11, pp. 804–809, Nov. 1978, doi: 10.1109/JQE.1978.1069698.
[30] H. Melchior and W. T. Lynch, 'Signal and noise response of high speed germanium avalanche photodiodes', *IEEE Trans. Electron Devices*, vol. ED-13, no. 12, pp. 829–838, Dec. 1966, doi: 10.1109/T-ED.1966.15856.
[31] T. Mikawa, S. Kagawa, T. Kaneda, Y. Toyama, and O. Mikami, 'Crystal orientation dependence of ionization rates in germanium', *Appl. Phys. Lett.*, vol. 37, no. 4, pp. 387–389, Aug. 1980, doi: 10.1063/1.91932.
[32] W. C. Dash and R. Newman, 'Intrinsic Optical Absorption in Single-Crystal Germanium and Silicon at 77°K and 300°K', *Phys. Rev.*, vol. 99, no. 4, pp. 1151–1155, Aug. 1955, doi: 10.1103/PhysRev.99.1151.
[33] Hamamatsu, 'g6854-01_kird1013e.pdf'. Accessed: Aug. 15, 2023. [Online]. Available: https://www.hamamatsu.com/content/dam/hamamatsu-photonics/sites/documents/99_SALES_LIBRARY/ssd/g6854-01_kird1013e.pdf
[34] ThorLabs, 'FGA21-SpecSheet.pdf'. Accessed: Oct. 31, 2022. [Online]. Available: https://www.thorlabs.com/drawings/4b27673743e15fd6-D1DABAAA-F71A-8742-98193F258E6D8C6B/FGA21-SpecSheet.pdf
[35] J. Ma *et al.*, 'Design considerations of high-performance InGaAs/InP single-photon avalanche diodes for quantum key distribution', *Appl. Opt.*, vol. 55, no. 27, p. 7497, Sep. 2016, doi: 10.1364/AO.55.007497.
[36] A. S. Huntington, M. A. Compton, and G. M. Williams, 'Improved breakdown model for estimating dark count rate in avalanche photodiodes with InP and InAlAs multiplication layers', presented at the Defense and Security Symposium, G. W. Kamerman and M. D. Turner, Eds., Orlando (Kissimmee), FL, May 2006, p. 62140R. doi: 10.1117/12.668659.
[37] S. Xie *et al.*, 'InGaAs/AlGaAsSb avalanche photodiode with high gain-bandwidth product', *Opt. Express*, vol. 24, no. 21, p. 24242, Oct. 2016, doi: 10.1364/OE.24.024242.
[38] M. S. Park and J. H. Jang, 'GaAs0.5Sb0.5 lattice matched to InP for 1.55 um photo-detection', *Electron. Lett.*, vol. 44, no. 8, p. 549, 2008, doi: 10.1049/el:20083433.
[39] J. Beck *et al.*, 'The HgCdTe electron avalanche photodiode', p. 8.
[40] X. Sun, J. B. Abshire, J. D. Beck, P. Mitra, K. Reiff, and G. Yang, 'HgCdTe avalanche photodiode detectors for airborne and spaceborne lidar at infrared wavelengths', *Opt. Express*, vol. 25, no. 14, p. 16589, Jul. 2017, doi: 10.1364/OE.25.016589.
[41] Z. Huang *et al.*, '21-GHz-Bandwidth Germanium-on-Silicon Photodiode Using Thin SiGe Buffer Layers', *IEEE J. Sel. Top. Quantum Electron.*, vol. 12, no. 6, pp. 1450–1454, Nov. 2006, doi: 10.1109/JSTQE.2006.884073.

[42] S. R. Forrest, R. F. Leheny, R. E. Nahory, and M. A. Pollack, 'In0.53Ga0.47As photodiodes with dark current limited by generation-recombination and tunneling', *Appl. Phys. Lett.*, vol. 37, no. 3, pp. 322–325, Aug. 1980, doi: 10.1063/1.91922.

[43] G. A. M. Hurkx, D. B. M. Klaassen, and M. P. G. Knuvers, 'A new recombination model for device simulation including tunneling', *IEEE Trans. Electron Devices*, vol. 39, no. 2, pp. 331–338, Feb. 1992, doi: 10.1109/16.121690.

[44] R. J. McIntyre, 'A new look at impact ionization-Part I: A theory of gain, noise, breakdown probability, and frequency response', *IEEE Trans. Electron Devices*, vol. 46, no. 8, pp. 1623–1631, Aug. 1999, doi: 10.1109/16.777150.

[45] E. O. Kane, 'Zener tunneling in semiconductors', *J. Phys. Chem. Solids*, vol. 12, no. 2, pp. 181–188, Jan. 1960, doi: 10.1016/0022-3697(60)90035-4.

[46] P. YU and M. Cardona, *Fundamentals of Semiconductors: Physics and Materials Properties*. in Graduate Texts in Physics. Springer Berlin Heidelberg, 2010. [Online]. Available: https://books.google.co.uk/books?id=4VCxDAEACAAJ

[47] J. I. Pankove, *Optical Processes in Semiconductors*. in Dover books on physics. Prentice-Hall, 1971. [Online]. Available: https://books.google.co.uk/books?id=zK7vAAAAMAAJ

[48] S. Adachi, 'Optical dispersion relations for GaP, GaAs, GaSb, InP, InAs, InSb, Al x Ga1− x As, and In1− x Ga x As y P1− y', *J. Appl. Phys.*, vol. 66, no. 12, pp. 6030–6040, Dec. 1989, doi: 10.1063/1.343580.

[49] F. Urbach, 'The Long-Wavelength Edge of Photographic Sensitivity and of the Electronic Absorption of Solids', *Phys. Rev.*, vol. 92, no. 5, pp. 1324–1324, Dec. 1953, doi: 10.1103/PhysRev.92.1324.

[50] W. Franz, 'Einfluß eines elektrischen Feldes auf eine optische Absorptionskante', *Z. Für Naturforschung A*, vol. 13, no. 6, pp. 484–489, Jun. 1958, doi: 10.1515/zna-1958-0609.

[51] L. V. Keldysh, 'Ionization in the field of a strong electromagnetic wave', *Sov. Phys. JETP*, pp. 56–63, Nov. 2023, doi: 10.1142/9789811279461_0008.

[52] K. Tharmalingam, 'Optical Absorption in the Presence of a Uniform Field', *Phys. Rev.*, vol. 130, no. 6, pp. 2204–2206, Jun. 1963, doi: 10.1103/PhysRev.130.2204.

[53] J. Callaway, 'Optical Absorption in an Electric Field', *Phys. Rev.*, vol. 130, no. 2, pp. 549–553, Apr. 1963, doi: 10.1103/PhysRev.130.549.

[54] A. Alping and L. A. Coldren, 'Electrorefraction in GaAs and InGaAsP and its application to phase modulators', *J. Appl. Phys.*, vol. 61, no. 7, pp. 2430–2433, Apr. 1987, doi: 10.1063/1.337912.

[55] G. E. Stillman, C. M. Wolfe, C. O. Bozler, and J. A. Rossi, 'Electroabsorption in GaAs and its application to waveguide detectors and modulators', *Appl. Phys. Lett.*, vol. 28, no. 9, pp. 544–546, May 1976, doi: 10.1063/1.88816.

[56] J. P. Zheng, L. Shi, F. S. Choa, P. L. Liu, and H. S. Kwok, 'Intensity-dependent photoluminescence spectra of semiconductor-doped glasses', *Appl. Phys. Lett.*, vol. 53, no. 8, pp. 643–645, Aug. 1988, doi: 10.1063/1.100396.

[57] G. Allan, C. Delerue, and M. Lannoo, 'Nature of Luminescent Surface States of Semiconductor Nanocrystallites', *Phys. Rev. Lett.*, vol. 76, no. 16, pp. 2961–2964, Apr. 1996, doi: 10.1103/PhysRevLett.76.2961.

[58] C. H. Henry and D. V. Lang, 'Nonradiative capture and recombination by multiphonon emission in GaAs and GaP', *Phys. Rev. B*, vol. 15, no. 2, pp. 989–1016, Jan. 1977, doi: 10.1103/PhysRevB.15.989.

[59] D. E. Aspnes, 'Recombination at semiconductor surfaces and interfaces', *Surf. Sci.*, vol. 132, no. 1–3, pp. 406–421, Sep. 1983, doi: 10.1016/0039-6028(83)90550-2.

[60] R. J. Nelson and R. G. Sobers, 'Interfacial recombination velocity in GaAlAs/GaAs heterostructures', *Appl. Phys. Lett.*, vol. 32, no. 11, pp. 761–763, Jun. 1978, doi: 10.1063/1.89921.

[61] J. S. Rimmer *et al.*, 'Minority-carrier confinement by doping barriers', *Mater. Sci. Eng. B*, vol. 9, no. 1–3, pp. 375–378, Jul. 1991, doi: 10.1016/0921-5107(91)90205-A.

[62] D. K. Schroder, 'Carrier lifetimes in silicon', *IEEE Trans. Electron Devices*, vol. 44, no. 1, pp. 160–170, Jan. 1997, doi: 10.1109/16.554806.
[63] S. S. Li and W. R. Thurber, 'The dopant density and temperature dependence of electron mobility and resistivity in n-type silicon', *Solid-State Electron.*, vol. 20, no. 7, pp. 609–616, Jul. 1977, doi: 10.1016/0038-1101(77)90100-9.
[64] M. I. Yernaux, C. Battochio, P. Verlinden, and F. Van De Wiele, 'A one-dimensional model for the quantum efficiency of front-surface-field solar cells', *Sol. Cells*, vol. 13, no. 1, pp. 83–97, Nov. 1984, doi: 10.1016/0379-6787(84)90095-4.
[65] G. G. Macfarlane and V. Roberts, 'Infrared Absorption of Germanium near the Lattice Edge', *Phys. Rev.*, vol. 97, no. 6, pp. 1714–1716, Mar. 1955, doi: 10.1103/PhysRev.97.1714.2.
[66] G. G. Macfarlane and V. Roberts, 'Infrared Absorption of Silicon Near the Lattice Edge', *Phys. Rev.*, vol. 98, no. 6, pp. 1865–1866, Jun. 1955, doi: 10.1103/PhysRev.98.1865.
[67] O. S. Heavens, *Optical Properties of Thin Solid Films*. in Dover Books on Physics Series. Dover Publications, 1991. [Online]. Available: https://books.google.co.uk/books?id=yfJjiZBAc-AC
[68] P. Drude, C. R. Mann, and R. A. Millikan, *The Theory of Optics*. Longmans, Green, and Company, 1901. [Online]. Available: https://books.google.co.uk/books?id=PLVCAAAAIAAJ
[69] L. R. Ingersoll and J. T. Littleton, 'A New Method of Determining the Optical Constants of Metals, and the Optical Constants of Silicon', *Phys. Rev. Ser. I*, vol. 31, no. 5, pp. 489–499, Nov. 1910, doi: 10.1103/PhysRevSeriesI.31.489.
[70] D. Weaire, 'Optical properties of solids — new developments', *Opt. Laser Technol.*, vol. 8, no. 3, p. 141, Jun. 1976, doi: 10.1016/0030-3992(76)90029-3.
[71] R. Swanepoel, 'Determination of the thickness and optical constants of amorphous silicon', *J. Phys. [E]*, vol. 16, no. 12, pp. 1214–1222, Dec. 1983, doi: 10.1088/0022-3735/16/12/023.
[72] G. Rey *et al.*, 'Absorption Coefficient of a Semiconductor Thin Film from Photoluminescence', *Phys. Rev. Appl.*, vol. 9, no. 6, p. 064008, Jun. 2018, doi: 10.1103/PhysRevApplied.9.064008.
[73] G. P. Donati, R. Kaspi, and K. J. Malloy, 'Interpolating semiconductor alloy parameters: Application to quaternary III–V band gaps', *J. Appl. Phys.*, vol. 94, no. 9, pp. 5814–5819, Nov. 2003, doi: 10.1063/1.1613371.
[74] R. J. McIntyre, 'Multiplication noise in uniform avalanche diodes', *IEEE Trans. Electron Devices*, vol. ED-13, no. 1, pp. 164–168, Jan. 1966, doi: 10.1109/T-ED.1966.15651.
[75] F. Capasso, 'Chapter 1 Physics of Avalanche Photodiodes', in *Semiconductors and Semimetals*, vol. 22, Elsevier, 1985, pp. 1–172. doi: 10.1016/S0080-8784(08)62952-X.
[76] J. C. Campbell, 'Recent Advances in Telecommunications Avalanche Photodiodes', *J. Light. Technol.*, vol. 25, no. 1, pp. 109–121, Jan. 2007, doi: 10.1109/JLT.2006.888481.
[77] A. R. J. Marshall, J. P. R. David, and C. H. Tan, 'Impact Ionization in InAs Electron Avalanche Photodiodes', *IEEE Trans. Electron Devices*, vol. 57, no. 10, pp. 2631–2638, Oct. 2010, doi: 10.1109/TED.2010.2058330.
[78] C. L. Anderson and C. R. Crowell, 'Threshold Energies for Electron-Hole Pair Production by Impact Ionization in Semiconductors', *Phys. Rev. B*, vol. 5, no. 6, pp. 2267–2272, Mar. 1972, doi: 10.1103/PhysRevB.5.2267.
[79] M. M. Hayat, B. E. A. Saleh, and M. C. Teich, 'Effect of dead space on gain and noise of double-carrier-multiplication avalanche photodiodes', *IEEE Trans. Electron Devices*, vol. 39, no. 3, pp. 546–552, Mar. 1992, doi: 10.1109/16.123476.
[80] P. Yuan *et al.*, 'A new look at impact ionization-Part II: Gain and noise in short avalanche photodiodes', *IEEE Trans. Electron Devices*, vol. 46, no. 8, pp. 1632–1639, Aug. 1999, doi: 10.1109/16.777151.
[81] D. S. G. Ong, Jo Shien Ng, M. M. Hayat, Peng Sun, and J. David, 'Optimization of InP APDs for High-Speed Lightwave Systems', *J. Light. Technol.*, vol. 27, no. 15, pp. 3294–3302, Aug. 2009, doi: 10.1109/JLT.2009.2020303.
[82] K. S. Lau *et al.*, 'Excess noise measurement in avalanche photodiodes using a transimpedance amplifier front-end', *Meas. Sci. Technol.*, vol. 17, no. 7, pp. 1941–1946, Jul. 2006, doi: 10.1088/0957-0233/17/7/036.

[83] F. R. Bacher, J. S. Blakemore, J. T. Ebner, and J. R. Arthur, ‘Optical-absorption coefficient of In1−xGaxAs/InP’, *Phys. Rev. B*, vol. 37, no. 5, pp. 2551–2557, Feb. 1988, doi: 10.1103/PhysRevB.37.2551.
[84] D. A. Humphreys, R. J. King, D. Jenkins, and A. J. Moseley, ‘Measurement of absorption coefficients of Ga0.47In0.53As over the wavelength range 1.0–1.7 μm’, *Electron. Lett.*, vol. 21, no. 25–26, p. 1187, 1985, doi: 10.1049/el:19850839.
[85] E. Zielinski, H. Schweizer, K. Streubel, H. Eisele, and G. Weimann, ‘Excitonic transitions and exciton damping processes in InGaAs/InP’, *J. Appl. Phys.*, vol. 59, no. 6, pp. 2196–2204, Mar. 1986, doi: 10.1063/1.336358.
[86] D. Hahn, O. Jaschinski, H.-H. Wehmann, A. Schlachetzki, and M. Von Ortenberg, ‘Electron-concentration dependence of absorption and refraction in n-In0.53Ga0.47As near the band-edge’, *J. Electron. Mater.*, vol. 24, no. 10, pp. 1357–1361, Oct. 1995, doi: 10.1007/BF02655448.
[87] L. Rapp and M. Eiselt, ‘Optical Amplifiers for Multi–Band Optical Transmission Systems’, *J. Light. Technol.*, vol. 40, no. 6, pp. 1579–1589, Mar. 2022, doi: 10.1109/JLT.2021.3120944.
[88] I. Vurgaftman, J. R. Meyer, and L. R. Ram-Mohan, ‘Band parameters for III–V compound semiconductors and their alloys’, *J. Appl. Phys.*, vol. 89, no. 11, pp. 5815–5875, Jun. 2001, doi: 10.1063/1.1368156.
[89] S. R. Forrest, R. F. Leheny, R. E. Nahory, and M. A. Pollack, ‘In0.53Ga0.47As photodiodes with dark current limited by generation-recombination and tunneling’, *Appl. Phys. Lett.*, vol. 37, no. 3, pp. 322–325, 1980, doi: 10.1063/1.91922.
[90] T. P. Pearsall, *GaInAsP alloy semiconductors*. Chichester [West Sussex]: Wiley, 1982.
[91] M. Levinshtein, S. L. Rumyantsev, M. Shur, and W. Scientific, *Handbook Series on Semiconductor Parameters: Ternary and quaternary III-V compounds*. in EBL-Schweitzer. World Scientific Publishing Company, 1999. [Online]. Available: https://books.google.co.uk/books?id=zLvACwAAQBAJ
[92] ThorLabs, ‘FD05D-SpecSheet.pdf’. Accessed: Oct. 31, 2022. [Online]. Available: https://www.thorlabs.com/drawings/4b27673743e15fd6-D1DABAAA-F71A-8742-98193F258E6D8C6B/FD05D-SpecSheet.pdf
[93] O. Blum *et al.*, ‘Highly reflective, long wavelength AlAsSb/GaAsSb distributed Bragg reflector grown by molecular beam epitaxy on InP substrates’, *Appl. Phys. Lett.*, vol. 66, no. 3, pp. 329–331, Jan. 1995, doi: 10.1063/1.114202.
[94] S. Nojima and H. Asahi, ‘Refractive index of InGaAs/InAlAs multiquantum-well layers grown by molecular-beam epitaxy’, *J. Appl. Phys.*, vol. 63, no. 2, pp. 479–483, Jan. 1988, doi: 10.1063/1.340267.
[95] M. V. Kurik, ‘Urbach rule’, *Phys. Status Solidi A*, vol. 8, no. 1, pp. 9–45, Nov. 1971, doi: 10.1002/pssa.2210080102.
[96] Y. P. Varshni, ‘Temperature dependence of the energy gap in semiconductors’, *Physica*, vol. 34, no. 1, pp. 149–154, Jan. 1967, doi: 10.1016/0031-8914(67)90062-6.
[97] S. R. Johnson and T. Tiedje, ‘Temperature dependence of the Urbach edge in GaAs’, *J. Appl. Phys.*, vol. 78, no. 9, pp. 5609–5613, Nov. 1995, doi: 10.1063/1.359683.
[98] M. V. Kurik, ‘Urbach rule’, *Phys. Status Solidi A*, vol. 8, no. 1, pp. 9–45, Nov. 1971, doi: 10.1002/pssa.2210080102.
[99] C. H. Grein and S. John, ‘Temperature dependence of the Urbach optical absorption edge: A theory of multiple phonon absorption and emission sidebands’, *Phys. Rev. B*, vol. 39, no. 2, pp. 1140–1151, Jan. 1989, doi: 10.1103/PhysRevB.39.1140.
[100] B. Bansal, V. K. Dixit, V. Venkataraman, and H. L. Bhat, ‘Alloying induced degradation of the absorption edge of InAsxSb1−x’, *Appl. Phys. Lett.*, vol. 90, no. 10, p. 101905, Mar. 2007, doi: 10.1063/1.2711388.
[101] X. Yi *et al.*, ‘Extremely low excess noise and high sensitivity AlAs0.56Sb0.44 avalanche photodiodes’, *Nat. Photonics*, vol. 13, no. 10, pp. 683–686, Oct. 2019, doi: 10.1038/s41566-019-0477-4.

[102] J. C. Campbell, 'Recent advances in avalanche photodiodes: Ultraviolet to infrared', in *IEEE Photonic Society 24th Annual Meeting*, Arlington, VA, USA: IEEE, Oct. 2011, pp. 202–203. doi: 10.1109/PHO.2011.6110496.
[103] 'Hamamatsu InGaAs APD G14858-0020AA'.
[104] L. W. Cook, G. E. Bulman, and G. E. Stillman, 'Electron and hole impact ionization coefficients in InP determined by photomultiplication measurements', *Appl. Phys. Lett.*, vol. 40, no. 7, pp. 589–591, Apr. 1982, doi: 10.1063/1.93190.
[105] J. Xie, S. Xie, R. C. Tozer, and C. H. Tan, 'Excess Noise Characteristics of Thin AlAsSb APDs', *IEEE Trans. Electron Devices*, vol. 59, no. 5, pp. 1475–1479, May 2012, doi: 10.1109/TED.2012.2187211.
[106] S. Xie *et al.*, 'InGaAs/AlGaAsSb avalanche photodiode with high gain-bandwidth product', *Opt. Express*, vol. 24, no. 21, p. 24242, Oct. 2016, doi: 10.1364/OE.24.024242.
[107] M. Ren, S. J. Maddox, M. E. Woodson, Y. Chen, S. R. Bank, and J. C. Campbell, 'AlInAsSb separate absorption, charge, and multiplication avalanche photodiodes', *Appl. Phys. Lett.*, vol. 108, no. 19, p. 191108, May 2016, doi: 10.1063/1.4949335.
[108] S. Lee *et al.*, 'Random alloy thick AlGaAsSb avalanche photodiodes on InP substrates', *Appl. Phys. Lett.*, vol. 120, no. 7, p. 071101, Feb. 2022, doi: 10.1063/5.0067408.
[109] D. S. G. Ong, Jo Shien Ng, M. M. Hayat, Peng Sun, and J. David, 'Optimization of InP APDs for High-Speed Lightwave Systems', *J. Light. Technol.*, vol. 27, no. 15, pp. 3294–3302, Aug. 2009, doi: 10.1109/JLT.2009.2020303.
[110] M. H. Woods, W. C. Johnson, and M. A. Lampert, 'Use of a Schottky barrier to measure impact ionization coefficients in semiconductors', *Solid-State Electron.*, vol. 16, no. 3, pp. 381–394, Mar. 1973, doi: 10.1016/0038-1101(73)90013-0.
[111] D. S. Ong, K. F. Li, G. J. Rees, J. P. R. David, and P. N. Robson, 'A simple model to determine multiplication and noise in avalanche photodiodes', *J. Appl. Phys.*, vol. 83, no. 6, pp. 3426–3428, 1998, doi: 10.1063/1.367111.
[112] S. A. Plimmer, J. P. R. David, and D. S. Ong, 'The merits and limitations of local impact ionization theory [APDs]', *IEEE Trans. Electron Devices*, vol. 47, no. 5, pp. 1080–1088, May 2000, doi: 10.1109/16.841244.
[113] X. Jin *et al.*, 'Excess noise measurements in Al0.85Ga0.15As0.56Sb0.44 avalanche photodiodes', in *Optical Sensing and Detection VII*, F. Berghmans and I. Zergioti, Eds., Strasbourg, France: SPIE, May 2022, p. 7. doi: 10.1117/12.2624285.
[114] J. S. Ng, C. H. Tan, J. P. R. David, G. Hill, and G. J. Rees, 'Field dependence of impact ionization coefficients in In0.53Ga0.47As', *IEEE Trans. Electron Devices*, vol. 50, no. 4, pp. 901–905, Apr. 2003, doi: 10.1109/TED.2003.812492.
[115] C. Canali *et al.*, 'Measurement of the electron ionization coefficient at low electric fields in InGaAs-based heterojunction bipolar transistors', *Appl. Phys. Lett.*, vol. 66, no. 9, pp. 1095–1097, Feb. 1995, doi: 10.1063/1.113583.
[116] E. Tea and F. Aniel, 'Minority electron mobilities in GaAs, In0.53Ga0.47As, and GaAs0.50Sb0.50 calculated within an ensemble Monte Carlo model', *J. Appl. Phys.*, vol. 109, no. 3, p. 033716, Feb. 2011, doi: 10.1063/1.3533963.
[117] R. H. Kingston, 'Electroabsorption in GaInAsP', *Appl. Phys. Lett.*, vol. 34, no. 11, pp. 744–746, Jun. 1979, doi: 10.1063/1.90657.
[118] B. R. Bennett and R. A. Soref, 'Analysis of Franz-Keldysh Electro-Optic Modulation in InP, GaAs, GaSb, InAs, And InSb', presented at the O-E/Fibers '87, T. E. Batchman, R. F. Carson, R. L. Galawa, and H. J. Wojtunik, Eds., San Diego, CA, Jan. 1987, p. 158. doi: 10.1117/12.967524.
[119] Y.-D. Hsieh, J.-H. Lin, R. Soref, G. Sun, H.-H. Cheng, and G.-E. Chang, 'Electro-absorption modulation in GeSn alloys for wide-spectrum mid-infrared applications', *Commun. Mater.*, vol. 2, no. 1, p. 40, Apr. 2021, doi: 10.1038/s43246-021-00144-z.
[120] M. Schmid *et al.*, 'Franz–Keldysh effect of germanium-on-silicon p–i–n diodes within a wide temperature range', *Thin Solid Films*, vol. 525, pp. 110–114, Dec. 2012, doi: 10.1016/j.tsf.2012.10.087.

[121] T. Maeda *et al.*, 'Measurement of avalanche multiplication utilizing Franz-Keldysh effect in GaN p-n junction diodes with double-side-depleted shallow bevel termination', *Appl. Phys. Lett.*, vol. 115, no. 14, p. 142101, Sep. 2019, doi: 10.1063/1.5114844.

[122] D. R. Wight *et al.*, 'Limits of electro-absorption in high purity GaAs, and the optimisation of waveguide devices', *IEE Proc. J Optoelectron.*, vol. 135, no. 1, p. 39, 1988, doi: 10.1049/ip-j.1988.0010.

[123] M. S. Leeson and F. P. Payne, 'Predicted performance of Franz-Keldysh effect optical reflection modulators and comparisons with similar multiple quantum well-based devices', *IEE Proc. - Optoelectron.*, vol. 141, no. 4, pp. 257–264, Aug. 1994, doi: 10.1049/ip-opt:19941175.

[124] M. Abramowitz and I. A. Stegun, *Handbook of Mathematical Functions: With Formulas, Graphs, and Mathematical Tables*. in Applied mathematics series. Dover Publications, 1965. [Online]. Available: https://books.google.co.uk/books?id=MtU8uP7XMvoC

[125] E. O. Kane, 'Zener tunneling in semiconductors', *J. Phys. Chem. Solids*, vol. 12, no. 2, pp. 181–188, 1959, doi: http://dx.doi.org/10.1016/0022-3697(60)90035-4.

[126] D. F. Blossey, 'Wannier Exciton in an Electric Field. I. Optical Absorption by Bound and Continuum States', *Phys. Rev. B*, vol. 2, no. 10, pp. 3976–3990, Nov. 1970, doi: 10.1103/PhysRevB.2.3976.

[127] M. Bhowmick, H. Xi, and B. Ullrich, 'Optical Bandgap Definition via a Modified Form of Urbach's Rule', *Materials*, vol. 14, no. 7, p. 1639, Mar. 2021, doi: 10.3390/ma14071639.

[128] B. O. Seraphin and N. Bottka, 'Franz-Keldysh Effect of the Refractive Index in Semiconductors', *Phys. Rev.*, vol. 139, no. 2A, pp. A560–A565, Jul. 1965, doi: 10.1103/PhysRev.139.A560.

[129] G. S. Kinsey, J. C. Campbell, and A. G. Dentai, 'Waveguide avalanche photodiode operating at 1.55 μm with a gain-bandwidth product of 320 GHz', *IEEE Photonics Technol. Lett.*, vol. 13, no. 8, pp. 842–844, Aug. 2001, doi: 10.1109/68.935822.

[130] Ning Duan *et al.*, 'Detrimental effect of impact ionization in the absorption region on the frequency response and excess noise performance of InGaAs-InAlAs SACM avalanche photodiodes', *IEEE J. Quantum Electron.*, vol. 41, no. 4, pp. 568–572, Apr. 2005, doi: 10.1109/JQE.2005.843613.

[131] L. J. J. Tan, J. S. Ng, C. H. Tan, and J. P. R. David, 'Avalanche Noise Characteristics in Submicron InP Diodes', *IEEE J. Quantum Electron.*, vol. 44, no. 4, pp. 378–382, Apr. 2008, doi: 10.1109/JQE.2007.914771.

[132] R. B. Emmons, 'Avalanche-Photodiode Frequency Response', *J. Appl. Phys.*, vol. 38, no. 9, pp. 3705–3714, Aug. 1967, doi: 10.1063/1.1710199.

[133] C. A. Gueymard, 'Parameterized transmittance model for direct beam and circumsolar spectral irradiance', *Sol. Energy*, vol. 71, no. 5, pp. 325–346, Nov. 2001, doi: 10.1016/S0038-092X(01)00054-8.

[134] S. Cao *et al.*, 'Theoretical Studies on InGaAs/InAlAs SAGCM Avalanche Photodiodes', *Nanoscale Res. Lett.*, vol. 13, no. 1, p. 158, Dec. 2018, doi: 10.1186/s11671-018-2559-5.

[135] J. S. Ng, C. H. Tan, J. P. R. David, and G. J. Rees, 'Effect of impact ionization in the InGaAs absorber on excess noise of avalanche photodiodes', *IEEE J. Quantum Electron.*, vol. 41, no. 8, pp. 1092–1096, Aug. 2005, doi: 10.1109/JQE.2005.850700.

[136] P. J. Ker, 'Development of high speed low noise InAs electron avalanche photodiodes'.

[137] X. Sun, J. B. Abshire, J. D. Beck, P. Mitra, K. Reiff, and G. Yang, 'HgCdTe avalanche photodiode detectors for airborne and spaceborne lidar at infrared wavelengths', *Opt. Express*, vol. 25, no. 14, p. 16589, Jul. 2017, doi: 10.1364/OE.25.016589.

[138] A. H. Jones, S. D. March, S. R. Bank, and J. C. Campbell, 'Low-noise high-temperature AlInAsSb/GaSb avalanche photodiodes for 2-μm applications', *Nat. Photonics*, vol. 14, no. 9, pp. 559–563, Sep. 2020, doi: 10.1038/s41566-020-0637-6.

[139] S. Lee *et al.*, 'Low noise Al0.85Ga0.15As0.56Sb0.44 avalanche photodiodes on InP substrates', *Appl. Phys. Lett.*, vol. 118, no. 8, p. 081106, Feb. 2021, doi: 10.1063/5.0035571.